Wegener Center for Climate and Global Change
University of Graz

Wegener Center/Uni Graz Technical Report for ESA/ESRIN No. 01/2016

Project: MMValRO-E
ESRIN/Contract No. 4000110769/14/I-AM

Multi-Mission Validation by Satellite Radio Occultation – Extension Project

Final Report

Prepared by:
M. Schwärz, G. Kirchengast, B. Scherllin-Pirscher,
J. Schwarz, F. Ladstädter, and B. Angerer

Doc-ID: WEGC–ESA-MMValRO-E–2016–FR
Issue 1.1
15th December, 2016

Wegener Center for Climate and Global Change
University of Graz

Wegener Center for Climate and Global Change, University of Graz, Brandhofgasse 5, A-8010 Graz, Austria
Wegener Center Web: http://www.wegcenter.at

Document Distribution List

Name	Organization	Email Address	Copies
A. Dehn	ESA/ESRIN	angelika.dehn@esa.int	1
S. Casadio	ESA/ESRIN	stefano.casadio@serco.com	1
G. Kirchengast	WEGC/UniGraz	gottfried.kirchengast@uni-graz.at	1
M. Schwärz	WEGC/UniGraz	marc.schwaerz@uni-graz.at	1

Document Change Record

Issue	Date	Change
1.0	30th November, 2016	Draft final version of the MIPAS Validation Report to ESA.
1.1	15th December, 2016	Consolidated Final Report version to ESA.

Contents

Acronyms and Abbreviations 7

Introduction 14

1 Quality Assessment of the OPSv5.6 RO Data 16
- 1.1 Radio Occultation Data Base at WEGC 16
- 1.2 Validation of Data Quality 17
  - 1.2.1 Bending Angle Quality 18
  - 1.2.2 Validation of Atmospheric Profiles 21
- 1.3 Temporal Evolution of Data Quality 27
- 1.4 Consistency Evaluation 30
  - 1.4.1 Spatial and Temporal Sampling 30
  - 1.4.2 Differences in Dry Temperature Climatologies in July 2008 31
  - 1.4.3 Temporal Evolution of Dry Temperature Consistency 31

2 MIPAS, GOMOS, and RAOB Validation 38
- 2.1 MIPAS Validation 38
  - 2.1.1 MIPAS Collocations 38
  - 2.1.2 MIPAS–RO Temperature Validation 39
  - 2.1.3 MIPAS-RO Altitude Validation 44
- 2.2 GOMOS Validation 57
  - 2.2.1 GOMOS Collocations 57
  - 2.2.2 GOMOS-RO HRTP Validation 58
  - 2.2.3 GOMOS–RO Density Validation 65
- 2.3 RAOB Validation 71
  - 2.3.1 RAOB Collocations 71
  - 2.3.2 RO vs. RAOB Temperature Comparison 72
  - 2.3.3 RO vs. RAOB Humidity Comparison 79
  - 2.3.4 RO vs. GRUAN Comparison 84

3 MMValRO Profiles Processing System 88
- 3.1 PPS Top-view Structure 88
  - 3.1.1 Occultation Processing System 90

3.1.2 Workload Assessment . . . 93
3.1.3 PPS and OPS Automation Issues . . . 98
3.1.4 Key PPS Algorithms . . . 99
3.2 Specification of the PPS Modules . . . 106
3.2.1 pps-exprof-download . . . 106
3.2.2 pps-exprof-2-db . . . 107
3.2.3 roprof-2-db . . . 108
3.2.4 pps-sel-cand . . . 109
3.2.5 pps-collocate . . . 110
3.2.6 pps-collocations-2-db . . . 111
3.2.7 pps-collocate-special-stations . . . 112
3.2.8 pps-validate . . . 113
3.2.9 pps-validate-2-db . . . 114
3.2.10 pps-plot . . . 115
3.2.11 pps-plot-2-db . . . 116
3.2.12 pps-present . . . 117
3.2.13 pps-convert . . . 118
3.2.14 pps-submit-2-nilu . . . 119

4 Summary and Outlook 120

A RO Method and Processing 126
A.1 Measurement Principle . . . 126
A.2 GPS and Excess Phase Delay . . . 128
A.3 Characteristics of Radio Occultation . . . 128
A.4 OPSv5.6 Processing . . . 130
A.4.1 OPSv5.6 Input Data . . . 130
A.4.2 Occultation Geometry . . . 131
A.4.3 Data Preparation . . . 132
A.4.4 Correction of the Earth's Oblateness . . . 132
A.4.5 Bending Angle Retrieval . . . 133
A.4.6 Atmospheric Refractivity . . . 136
A.4.7 Retrieval of Dry Atmospheric Parameters . . . 136
A.4.8 Retrieval of Moist Atmospheric Parameters . . . 141
A.4.9 Quality Control . . . 145
A.4.10 Reference to the Earth's Geoid . . . 146
A.4.11 Summary of OPSv5.6 Retrieval . . . 147
A.5 Beyond OPSv5.6 . . . 147
A.5.1 Rationale for the rOPS . . . 147
A.5.2 rOPS Development Projects . . . 149

List of Figures 151

List of Tables 157

Reference Documents 158

Acronyms and Abbreviations

Symbols

1D-Var 1-Dimensional Variational Data Assimilation. 39, 44, 57, 65, 72, 76, 141, 142

COSMIC-2 Constellation Observing System for Meteorology, Ionosphere, and Climate-2. 8, 149

C/NOFS Communications/Navigation Outage Forecasting System. 15, 18, 29, 31, 32, 38, 57, 130

FORMOSAT-3 Formosa Satellite mission-3. 8

FORMOSAT-7 Formosa Satellite mission-7. 8

FY-3C Feng Yun series-3 satellite C. 149

TerraSAR-X Terra: the Earth; SAR: Synthetic Aperture Radar; X: X-band radar (wavelength). 15, 18, 29–32, 130

A

AIUB Astronomical Institute at the University of Bern. 148

ALR Aeronautics and Space Agency. 149

B

BEAT Basic ENVISAT Atmospheric Toolbox. 106, 107

C

Cal/Val Calibration/Validation. 14, 88, 93, 98, 118, 123

CDAAC COSMIC Data Analysis and Archive Center. 16, 18, 23, 29, 131

CHAMP Challenging Mini-Satellite Payload. 15, 16, 18, 29–32, 38, 41, 57, 62, 67, 71, 76, 79, 121, 134–136, 138, 144

COLLOC Wegener Center database for collocation datasets. 89, 111

COSMIC Constellation Observing System for Meteorology, Ionosphere, and Climate. 7, 8, 38, 39, 57, 71, 72, 76, 79, 121

D

D-PAC German Processing and Archiving Centre. 57

DB Database. 89

DLR Deutsches Zentrum für Luft und Raumfahrt. 148

DWD Deutscher Wetterdienst. 71

E

ECMWF European Centre for Medium-Range Weather Forecasts. 21–23, 27, 32, 38, 39, 41, 42, 44, 57, 65, 71, 72, 76, 90, 98, 99, 106, 120–122, 125, 135, 136, 138–142, 144, 145

ECV Essential Climate Variable. 147–149

EGOPS End-to-End Generic Occultation Performance Simulation and Processing System. 11

ENVISAT ESA's Environmental Satellite. 7, 14, 15, 38, 41, 42, 45, 57, 62, 90, 106, 120, 121, 123, 124

EO Earth Observation. 9

ESA European Space Agency. 14, 38, 57, 88, 89, 93, 106, 107, 120, 123, 125, 149

ESRIN European Space Research Institute. 88, 106, 125, 149

EUMETSAT European Organization for the Exploitation of Meteorological Satellites. 131, 148

EVDC Envisat Validation Data Centre. 14, 99, 118, 119

F

F3C FORMOSAT-3/COSMIC. 15, 16, 18, 29–32, 93, 130, 131, 149

F7C2 FORMOSAT-7/COSMIC-2. 17

FFG Austrian Research Promotion Agency (Österreichische Forschungsförderungsgesellschaft). 149

FIELD Wegener Center Atmospheric Field database. 98, 99

FM FlightModel. 16, 18, 30–32, 131

FR Full Resolution Period of MIPAS (2002 to early 2004). 41, 42, 44, 45, 122

FWHM Full Width at Half Maximum. 103

G

GCOS Global Climate Observing System. 9, 82

GEOMS Generic EO Metadata Standard. 88

GFZ German Research Centre for Geosciences [former GeoForschungsZentrum]. 131

GLO Global. 41, 42, 45, 62, 67

GNOS GNSS radio-occultation sounder. 149

GNSS Global Navigation Satellite System. 9, 14, 124, 126, 128, 147

GO Geometrical Optics. 127, 129–131, 133–135

GOMOS Global Ozone Monitoring by Occultation of Stars. 14, 15, 29, 31, 57, 58, 62, 65, 67, 89, 90, 93, 101, 103, 104, 106, 107, 109, 111, 120–125

GPS Global Positioning System. 9, 82, 124, 126–128, 130, 131, 133, 136, 149

GPS/MET Global Positioning System/Meteorology [experiment]. 126, 147

GRACE Gravity Recovery and Climate Experiment. 15, 18, 29–32, 38, 57, 71

GRAS Global Navigation Satellite Systems Receiver for Atmospheric Sounding. 11, 149

GRUAN GCOS Reference Upper Air Network. 71, 82, 84, 87

H

HDF Hierarchical Data Format. 9

HDF5 Hierarchical Data Format Version 5. 88, 118, 119

HRTP High Resolution Temperature Profile. 57, 62, 101, 103, 121

I

IAP Institute of Atmospheric Physics [Russian Academy of Sciences]. 148

IGG Institute of Geodesy and Geophysics. Chinese Academy of Sciences. 148

J

JPL Jet Propulsion Laboratory. 148

L

L Level. 9, 10

L1 L band signal no. 1 transmitted by GPS satellites (centered at 1.57542 GHz). 131, 133, 134

L1 Level 1 [data product]. 93

L1a Level 1a [data product]. 93

L1b Level 1b [data product]. 89

L2 L band signal no. 2 transmitted by GPS satellites (centered at 1.22760 GHz). 131, 133

L2 Level 2 [data product]. 88–90, 106–108

LEO Low Earth Orbit. 30, 124, 126, 127, 130, 131, 133

M

MetOp Meteorological Operational [satellite series]. 11, 15, 16, 18, 23, 29–32, 131, 149, 151

MIPAS Michelson Interferometer for Passive Atmospheric Sounding. 14, 15, 29, 31, 38, 39, 41, 42, 44, 45, 47, 58, 62, 65, 72, 79, 89, 90, 93, 101, 103–107, 109, 111, 120–125, 151, 152

ML2PPv6.0 ESA ML2PP processor version 6.0. 38

ML2PPv7.03 ESA ML2PP processor version 7.03. 38, 120–122

MMValRO Multi-Mission Validation by Satellite Radio Occultation [project]. 15, 38, 39, 44, 57, 58, 71, 72, 79, 88, 103, 120, 123–125, 149

MMValRO-E Multi-Mission Validation by Satellite Radio Occultation – Extension Project. 14, 88, 89, 120, 125

MSIS Mass Spectrometer and Incoherent Scatter Radar [model of the middle atmosphere]. 18, 29, 134

MSL Mean Sea Level. 136, 138–140, 144, 146

Multi-TASTE Multi-Mission Validation by Sounders, Spectrometers, and Radiometers. 14, 90, 99, 112

N

NHL Northern High Latitudes. 41, 42, 45, 62, 67

NILU Norwegian Institute for Air Research. 14, 88, 93, 98, 99, 118, 119, 123

NLL Northern Low Latitudes. 41, 42, 45, 62, 67

NML Northern Mid Latitudes. 41, 42, 45, 62, 67

O

OL Open Loop. 130, 131

OPS Occultation Processing System. 15, 16, 88, 90, 93, 98, 99, 108, 123, 124, 130, 131, 135, 146, 157

OPSCLIMPROP Occultation Processing System for Cal/Val and Climate: Level 1 Processing with Integrated Uncertainty Propagation. 149

OPSCLIMTRACE Occultation Processing System for Cal/Val and Climate: Algorithm Advancements and SI-traceable Processing. 149

OPSCLIMVALUE Value-added Products and Validation of Occultation Processing System Re-processing Data for Climate Monitoring. 149

OPSGRAS Reference Occultation Processing System for GRAS on MetOp and other Past and Future RO Missions. 149

OPSv5.4 Occultation Processing System Version 5.4 [EGOPS revision number 979]. 39, 65, 130, 131, 155

OPSv5.6 Occultation Processing System version 5.6. 15, 16, 22, 23, 27, 31, 32, 38, 39, 41, 42, 44, 45, 47, 57, 62, 65, 67, 71, 120, 124, 130–135, 142, 146, 151–153, 155, 157

OPSv5.6.2 Occultation Processing System version 5.6.2. 15, 120

OR Optimized Resolution Period of MIPAS (2005 to 2012). 41, 42, 45, 122

P

PLL Phase Locked Loop. 130, 131

POD Precise Orbit Determination. 90

PPS Profiles Processing System. 15, 88, 89, 93, 98, 103, 123, 124

PROF Wegener Center Profile (and Phase-delay) database application. 89, 90, 93, 98, 99, 107, 108, 110, 112

Q

QF Quality Flag. 16, 27, 134, 135, 145

R

RAER Retrieval to A-priori Error Ratio. 23, 27, 29

RAOB Radiosonde Observation. 123

RAOB Radiosonde Observation (Rawinsonde Observation). 14, 15, 29, 31, 38, 71, 72, 75, 76, 79, 82, 90, 93, 99, 101, 102, 106, 107, 109, 111, 120, 121, 124, 125, 154, 155

RMIT Royal Melbourne Institute of Technology. 148

RMS Root Mean Square [error]. 30

RMSE Root-Mean-Square Error. 58, 62

RO Radio Occultation. 10, 11, 14–17, 21–23, 27, 29–32, 38, 39, 41, 42, 44, 45, 47, 57, 58, 62, 65, 67, 71, 72, 75, 76, 79, 82, 84, 87, 88, 90, 93, 98, 99, 103–105, 108, 110–113, 118–130, 133–136, 138–142, 144–149, 151–154

ROM Radio Occultation Meteorology. 148

rOPS Reference Occultation Processing System. 15, 148, 149

S

SAC-C Satélite de Aplicaciones Científicas/Scientific Applications Satellite C. 15, 18, 29–32, 38, 57

SAF Satellite Application Facility. 148

SHL Southern High Latitudes. 41, 42, 45, 62, 67

SI International System of Units. 11, 147, 148

SLL Southern Low Latitudes. 41, 42, 45, 62, 67

SML Southern Mid Latitudes. 41, 42, 45, 62, 67

T

TP Tangent Point. 126

U

UCAR University Corporation for Atmospheric Research. 16, 18, 23, 29, 131, 148

UG University of Graz. 13

UTC Universal Time Coordinated. 104

UTLS Upper Troposphere–Lower Stratosphere [region]. 39, 45, 65, 121, 122, 126, 130

V

VAL Wegener Center database for validation datasets. 89, 114

VALID Satellite Validation with LIDAR Data. 14, 90, 99, 112

W

WEGC Wegener Center for Climate and Global Change [University of Graz]. 16, 120, 124, 125, 130, 135, 148, 149

WO Wave Optics. 127–131, 133, 135

WOCAS Wegener Center Occultation and Climate Analysis System. 88, 123, 125

Z

zRAER50 Impact altitude, where retrieval to apriori error ratio equals 50 %. 27, 29

Introduction

Within the MMValRO-E project, the Wegener Center has developed and provides long-term RO validation data, which will be used in the long-loop monitoring of trends and variability related to both spaceborne instrument and climate system variations. Applications in addition to direct monitoring include long-term validation of atmospheric satellite data products such as from ENVISAT, validation of geophysical retrieval algorithms, bridging between temporally separated space missions, as well as scientific evaluation of atmospheric processes. The project ensures the collection of correlative RO measurements suitable for in-depth examination of tropospheric and stratospheric profiles retrieved from (ESA) satellite atmospheric observations.

This undertaking is highly worthwhile since the unique combination of global coverage, high accuracy, long-term stability, and all weather capability makes the validation with RO measurements preferable to other methods. The currently (2016) available RO receiver constellation provides a combined total of up to about 1500 profiles per day. With the further extension of the GNSS, e.g., by the upcoming Galileo system, this number will further increase.

In the frame of the MMValRO-E project, a long-term database of temperature, humidity, pressure, density, and refractivity, as a function of mean-sea-level altitude, has been established, covering in particular the thermodynamic state of the upper troposphere/lower stratosphere region (about 5 km to 35 km altitude). The correlative RO data provided during the project have been collocated with the comparable ESA mission datasets from the ENVISAT atmospheric instruments MIPAS and GOMOS, as well as with RAOB data from the global net of RAOB stations and with the ground-based validation sites as defined in the Multi-TASTE and VALID projects related to ENVISAT. Correlative data for specific campaigns will also be provided on ESA demand. The correlative data have been provided to a Cal/Val repository of ESA, which is providing the Cal/Val and science community a direct access to these data (Envisat Validation Data Centre, hosted by NILU, Kjeller, Norway).

Furthermore, the Wegener Center has validated the selected ESA satellite data (from MIPAS and GOMOS) as well as the RAOB data against the correlative RO data used as reference, in order to derive estimates of the systematic and random errors and their changes in time. Also specific validation support to ESA algorithm developments and other ad-hoc requests was provided on ESA demand. Support and advice regarding ESA validation strategies, both multi-mission and mission-specific for ESA missions, was provided on demand as well.

The project worked towards reliable long-term provision of the RO validation data, and of the related validation analysis results, including a fresh re-processing of the RO data (OPSv5.6.2 further called OPSv5.6 throughout the report). In particular, RO satellite missions included by the end of the current project are CHAMP, SAC-C, F3C, GRACE, C/NOFS, MetOp-A, and TerraSAR-X (the raw data of the latter two are not yet available at the desired quality, so also the derived products are of lower quality). The collective RO dataset covers the time from January 2002 until July 2016, i.e., covers the full ENVISAT observing period from ENVISAT's launch in March 2002 to its end of mission in April 2012.

In this report we start with a description of the quality of the Wegener Center OPSv5.6 RO data (Chapter 1). We proceed with a description of the results of the MMValRO validation analyses (Chapter 2). The monthly records extend to the end of the ENVISAT period (April 2012), i.e., to the end of the available MIPAS and GOMOS measurements. Also the validation of RAOB measurements was performed over this period plus the recent years until mid-2016. Chapter 3 then describes the MMValRO PPS, the system which now operationally performs the MMValRO tasks. In this part of the report a description of the processing chains of the PPS is given. In addition, a short description of the processing chain of the OPS is included here to show that the enabling of operational processing has required a redesign, including a full automation, of the OPS which was developed in a separate project. Finally, this chapter contains a detailed description of the individual processing modules of the PPS. A summary and outlook (Chapter 4) closes the report in summarizing the project activities and results.

As supplementary information, Appendix A provides a description of the Wegener Center RO processing system OPSv5.6, including also an outlook to the next-generation system rOPS that is currently under development.

1 RO Data from Different Satellites and WEGC Quality Analysis

1.1 Radio Occultation Data Base at WEGC

To derive profiles of bending angle, refractivity, density, pressure, temperature, and specific humidity, the WEGC[1] OPS[2] uses excess phase profiles and orbit information provided by other data centers. Even though the RO[3] technique itself is self-calibrating, different data processing schemes yield differences in atmospheric RO data products, which cannot be neglected [ASW03; Eng06; Ho+12; LLS09; Ste+13]. For that reason WEGC OPSv5.6[4] uses excess phase and orbit information provided by UCAR[5]/CDAAC[6] for all satellites. However, differences in retrieved products can still result from different data versions used at UCAR/CDAAC. The most recent CHAMP[7] data version, e.g., is 2014.0140, the current versions of F3C[8] data are 2014.2860, that of MetOp[9]-A,B is 2016.0120.

Figure 1.1 shows all high quality profiles (bending angle QF = 0 and QF = 2, refractivity, and dry temperature/physical temperature QF = 0) available at WEGC from 2001 to 2012. For detailed info on the quality flags cf. Appendix A. The long-term record of CHAMP data together with that from the other satellites can already be used for climate trend analyses [e.g. Lac+11; Ste+09; Ste+11]. With the launch of F3C and MetOp-A in 2006 the number of available RO data has increased by a factor of ten, which enables RO data to be used not only for global climate studies [Lad+11; SP+12; Ste+09] but also for continental-scale or even regional climate investigations.

However, the F3C satellites have already passed their designated life-time and are degrading: F3C/FM[11]-3 has been out of contact since August 1, 2010 and F3C/FM-4 has not delivered any data since July 2015. Several F3C did not provide data in some time intervals due to different reasons. There was no contact e.g., to F3C/FM-5 and to F3C/FM-6 from September 26, 2010 to November 10, 2010 and from September 9, 2007 to November 13,

---

[1] Wegener Center for Climate and Global Change

[2] Occultation Processing System

[3] Radio Occultation

[4] Occultation Processing System version 5.6

[5] University Corporation for Atmospheric Research

[6] COSMIC Data Analysis and Archive Center

[7] Challenging Mini-Satellite Payload

[8] FORMOSAT-3/COSMIC

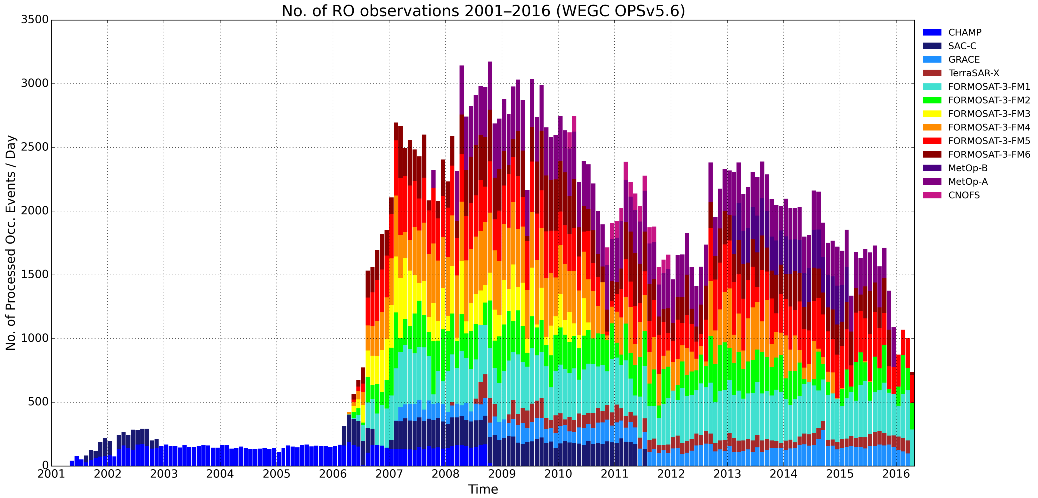

Figure 1.1: Number of high quality measurements derived from different RO satellites on a daily basis from 2001 to 2016. The total number of measurements significantly increased in 2006, when additional measurements performed by the six F3C satellites became available.

2007, respectively. F3C/FM-2 operates with only one solar panel and all F3C spacecraft (FM-1, FM-2, FM-4, FM-5, FM-6) are experiencing some level of battery degradation.

For global climate monitoring and reliable calibration/validation data source for other data, it is of very high importance to assure the continuity of RO measurements with global coverage and coverage of all local times. Therefore there is an urgent need for all twelve F7C2[12] satellites. The launch date for six satellites which will be in low inclination orbits is currently planned for September 2017. For the other six satellites which will be in high inclination orbits to provide coverage also of mid- and high latitudes the funding is still not assigned by the US government.

1.2 Validation of Data Quality of a Selected Set from Each Satellite

The reliability of estimated atmospheric climate trends strongly depends on data quality. Even though the RO technique features high accuracy and high precision it is not possible to completely remove ionospheric effects in the neutral atmospheric retrieval. Since the ionospheric correction in the retrieval process only yields elimination of first order iono-

---

[12] FORMOSAT-7/COSMIC-2

sphere terms, the ionosphere residual is larger during high solar activity than during low solar activity. Danzer, Scherllin-Pirscher, and Foelsche [DSPF13] estimated this error to be approximately 0.4 µrad for solar maximum conditions and 0.05 µrad for solar minimum conditions.

Furthermore, data quality is affected by the receiver quality and by the procedure applied to correct for potential clock errors. The latter is performed differently for the satellites. UCAR/CDAAC, e.g., applies single differencing for CHAMP and F3C data but zero-differencing for GRACE[13]-A and MetOp-A (W. Schreiner, UCAR, pers. comm. October 2009).

1.2.1 Bending Angle Quality

Bending angle quality is validated from bending angle bias and bending angle noise estimated between 65 km and 80 km impact height, cf. Appendix A. The use of simple climatological MSIS[14] bending angles as a reference to estimate these statistics is reasonable since at these high altitudes they generally fit the real situation within 0.5 µrad (the total atmospheric bending angle above 70 km is not higher than about this value). Only high quality profiles are used for bending angle validation. To get a representative ensemble of profiles, data from all satellites are analyzed for three consecutive day, i.e., from July 14, 2008 to July 16, 2008.

Figure 1.2 shows the median of the bending angle bias against the MSIS climatology for the different satellites over the time they were available at the UCAR data archive. In Figure 1.3 the bending angle noise can be seen. The different colors are indicating different latitude bands.

In Figure 1.2 one can see that CHAMP, GRACE, SAC-C[15], MetOp-A, MetOp-B, as well as FM-1 as an example for the F3C satellite series and TerraSAR-X[16] reveal similar bending angle quality. Only C/NOFS[17] data exhibit a little bit degraded bias structure.

Regarding the bending angle noise (cf. Figure 1.3) it can be said that all satellites except C/NOFS and TerraSAR-X show a very consistent evolution of the noise data over time. CHAMP and SAC-C, which were both launched in 2000, and GRACE-A (launch 2002) feature slightly larger bending angle noise than other satellites. In general, it can be seen that the data of both MetOp satellites are superior to all the other satellite data: MetOp-A anb MetOp-B bending angle noise is about a factor of two better than that of F3C (see Figure 1.3).

Figure 1.4 exhibits the difference in bending angle bias between the old UCAR data version (2011.2980) for the MetOp-A satellite and the new one (2016.0120). One clearly

---

[14] Mass Spectrometer and Incoherent Scatter Radar (model)

[15] Satélite de Aplicaciones Científicas/Scientific Applications Satellite C

[16] Terra Synthetic Aperture Radar

[17] Communications/Navigation Outage Forecasting System

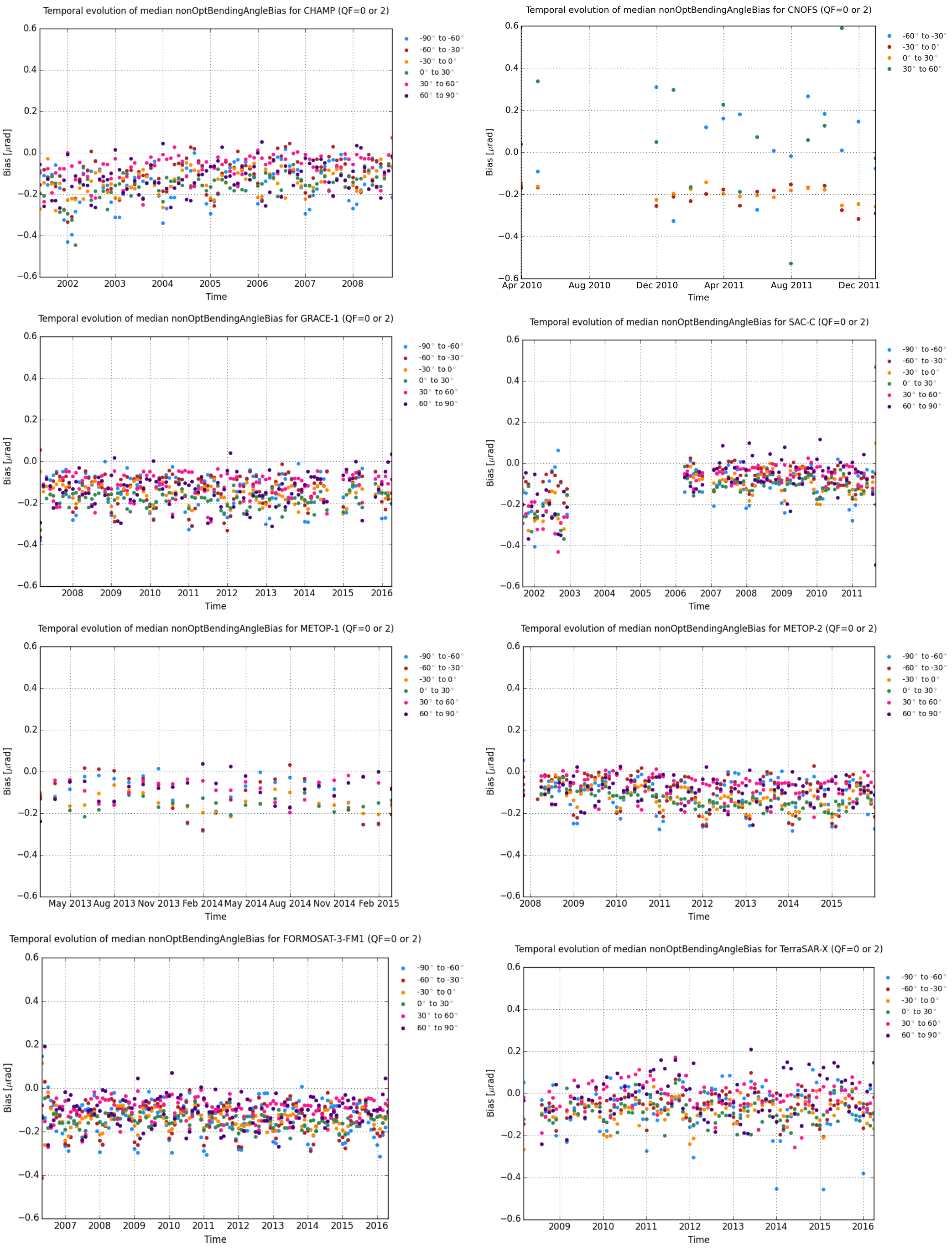

Figure 1.2: Bending angle bias as a function of geographic latitude

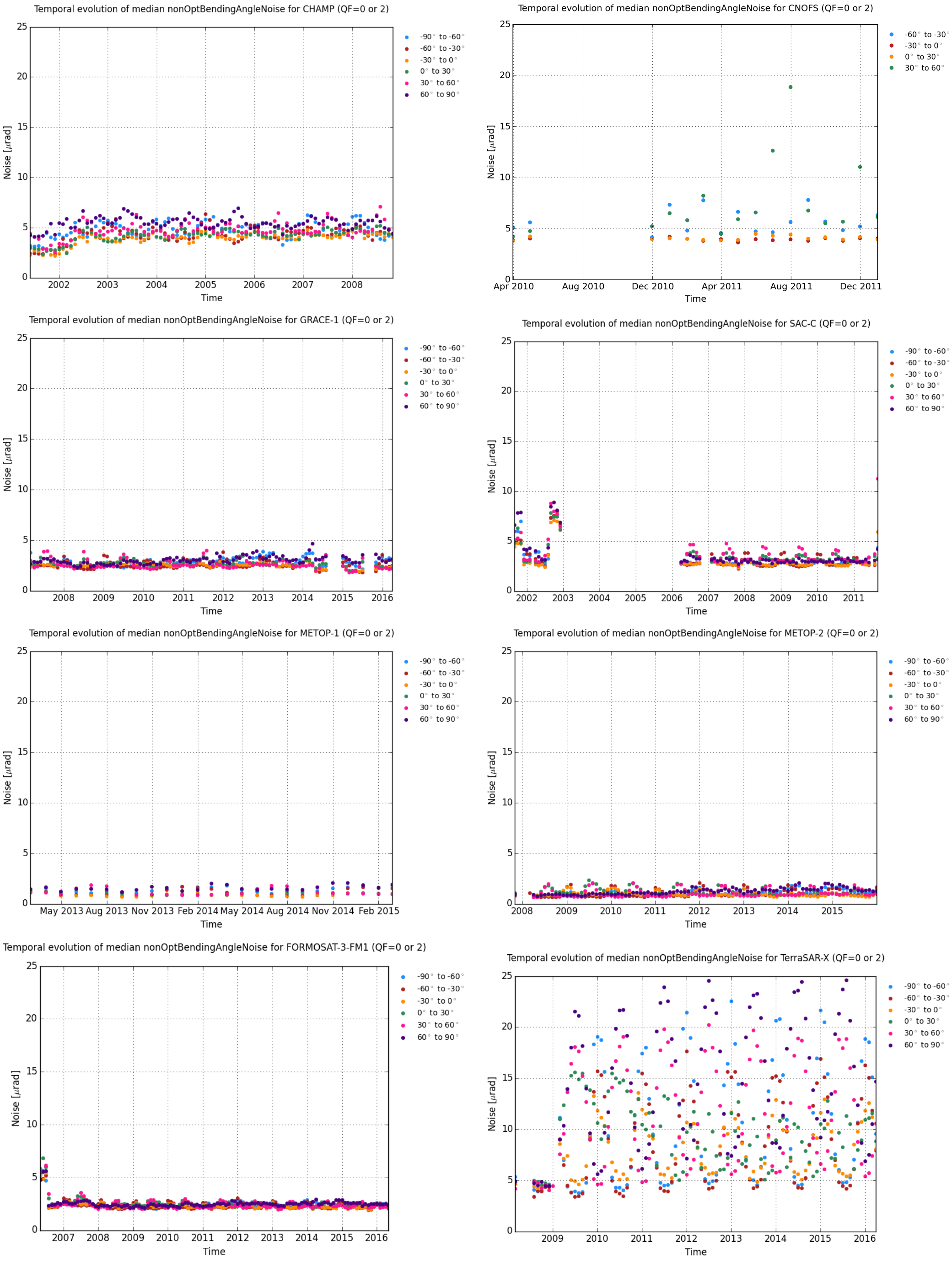

Figure 1.3: Bending angle noise as a function of geographic latitude

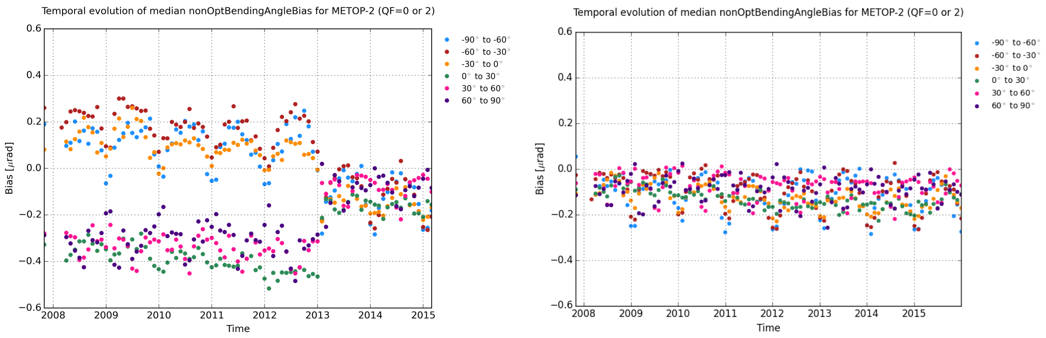

Figure 1.4: Bending angle bias as a function of geographic latitude for MetOp-A data version 2011.2980 (left) and 2016.0120 (right).

can see that the new version removed the hemisphere dependent bias structures which were mentioned in the previous report (cf. Schwärz et al. [Sch+13]).

1.2.2 Validation of Atmospheric Profiles

Retrieved atmospheric profiles are routinely validated against co-located profiles provided by ECMWF[18]. For each RO profile, a co-located reference profile is extracted from an ECMWF analysis field. ECMWF fields are used at a reduced spatial resolution of T42, which corresponds to approximately 300 km. This horizontal resolution is selected to roughly match the natural horizontal resolution of RO profiles, which is approximately 300 km as well.

Co-located reference profiles are extracted at times and locations of RO events. In a first step the ECMWF time layer nearest to the time of the RO event is allocated (temporal difference always smaller than 3 hours). The four ECMWF time layers do not represent an optimal sampling of all harmonics of the diurnal cycle. However, four time layers are sufficient to sample the diurnal cycle up to the second harmonics (the semidiurnal variations). In a second step the ECMWF field is spatially interpolated to the geographic event location, where the co-located profile is extracted. The used interpolation method depends on the particular parameter:

temperature, dry temperature: horizontal: 4-point polynomial (cubic) interpolation adapted by M. E. Gorbunov and A. K. Steiner (for a detailed description cf. [Lac10]); vertical: natural cubic spline interpolation.

refractivity, pressure, dry pressure: horizontal: 4-point polynomial (cubic) interpolation adapted by M. E. Gorbunov and A. K. Steiner (for a detailed description cf. [Lac10]);

---

[18] European Centre for Medium-Range Weather Forecasts

vertical: natural cubic spline interpolation; note: the interpolation is performed on the natural logarithm of the values of the particular parameters;

specific humidity: horizontal: linear interpolation; vertical: linear interpolation;

density: the density values are calculated out of the interpolated values of interpolated input parameters;

dry density: the dry density values are retrieved from the interpolated refractivity values under the assumption of the hydrostatic equilibrium.

The validation methodology is based on error characteristics of dry pressure, dry temperature, physical temperature, and specific humidity. We follow the approach of Steiner and Kirchengast [SK05] and Steiner, Löscher, and Kirchengast [SLK06], and Scherllin-Pirscher et al. [SP+11a]. The difference profile is calculated for each corresponding pair of profiles:

$$\Delta x(z_j) = x_{\mathrm{RO}}(z_j) - x_{\mathrm{coloc}}(z_j), \tag{1.1}$$

where $\Delta x(z_j)$ denotes the difference of the retrieved profile x_{RO} and the co-located (ECMWF) profile x_{coloc} at altitude level z_j, without attempting to match their different vertical resolutions (since the difference is reasonably small so that the intercomparison results do not change appreciably by aiming to match resolutions). The mean systematic difference $\overline{\Delta x(z_j)}$ is calculated by

$$\overline{\Delta x(z_j)} = \frac{1}{N(z_j)} \sum_{i=1}^{N(z_j)} \Delta x_i(z_j), \tag{1.2}$$

with $N(z_j)$ being the number of profiles at altitude level z_j. The number of available samples decreases with decreasing altitude because increasing humidity leads to atmospheric multipath and signal degradation.

The determination of the standard deviation of the difference profiles $\sigma(z_j)$ is based on

$$\sigma(z_j) = \sqrt{\frac{1}{N(z_j)-1} \sum_{i=1}^{N(z_j)} \left(\Delta x_i(z_j) - \overline{\Delta x(z_j)}\right)^2}. \tag{1.3}$$

Monthly data from all satellites stem from July 2008. The statistics is calculated for different latitude regions: low (30°S to 30°N), middle (30°S/N to 60°S/N), and high (60°S/N to 90°S/N) latitudes. In addition, the Global (90°S to 90°N), the Northern Hemisphere (NH, from 0° to 90°N), and the Southern Hemisphere (SH, from 0° to 90°S) regions are analyzed.

Validation of Dry Pressure Profiles

Due to the roughly exponential decrease of dry pressure with height, statistical differences between RO and ECMWF are shown in terms of relative quantities, which are derived by dividing the absolute difference profiles by the mean of all ECMWF reference profiles.

Figure 1.5 depicts the dry pressure validation results from 4 km to 35 km. Different satellites are displayed in different colors, the bias is shown in solid lines, standard deviations in dashed lines. Systematic differences of all satellite data relative to ECMWF analyses show a very smooth behavior and are very close to each other. Simple exception are MetOp-A data, which feature a negative bias (compared to the other satellites) in the northern hemisphere and a positive bias in the southern hemisphere. This hemispheric characteristics results from the bug in the UCAR/CDAAC excess phase and orbit processing, which also caused the hemispherically different bending angle bias (cf. Subsection 1.2.1).

The bias of the remaining satellites is negative up to approximately 30 km and positive above. However, it remains within ±0.5 % in the entire altitude range. The standard deviation is constant (0.3 %) from approximately 5 km up to approximately 17 km, above it increases to about 1 % (global mean) at 35 km.

Validation of Dry Temperature Profiles

Dry temperature validation results are shown in Figure 1.6. As already found for dry pressure, the bias of MetOp-A dry temperature features a hemispherically dependent characteristics. Compared to the other satellite data, MetOp-A dry temperature is lower in the northern hemisphere and higher in the southern hemisphere. The difference between MetOp-A and the other satellites increases with height and reaches more than 2 K at 35 km.

The bias of the remaining RO satellite data relative to ECMWF analyses is very close to zero up to 25 km. Above 25 km, the bias is positive, reaching approximately 1 K at 35 km. Within the upper troposphere, the standard deviation is very small (<1 K) up to approximately 20 km. Above it increases and at an altitude of 35 km it is larger than 2 K.

Validation of Tropospheric Temperature Profiles

Tropospheric temperature is in very good agreement for all satellites, even MetOp-A shows the same characteristics relative to ECMWF as the other satellites (see Figure 1.7). The bias of tropospheric temperature is very close to zero (<0.5 K) in the entire troposphere, the standard deviation rarely exceeds 1 K.

The reason for this very small bias and the small standard deviation is the considerable amount of background information (ECMWF short-term forecasts) used in the retrieval of physical temperature (see Appendix A). The RAER[19] profile of physical temperature (not

---

[19] Retrieval to A-priori Error Ratio

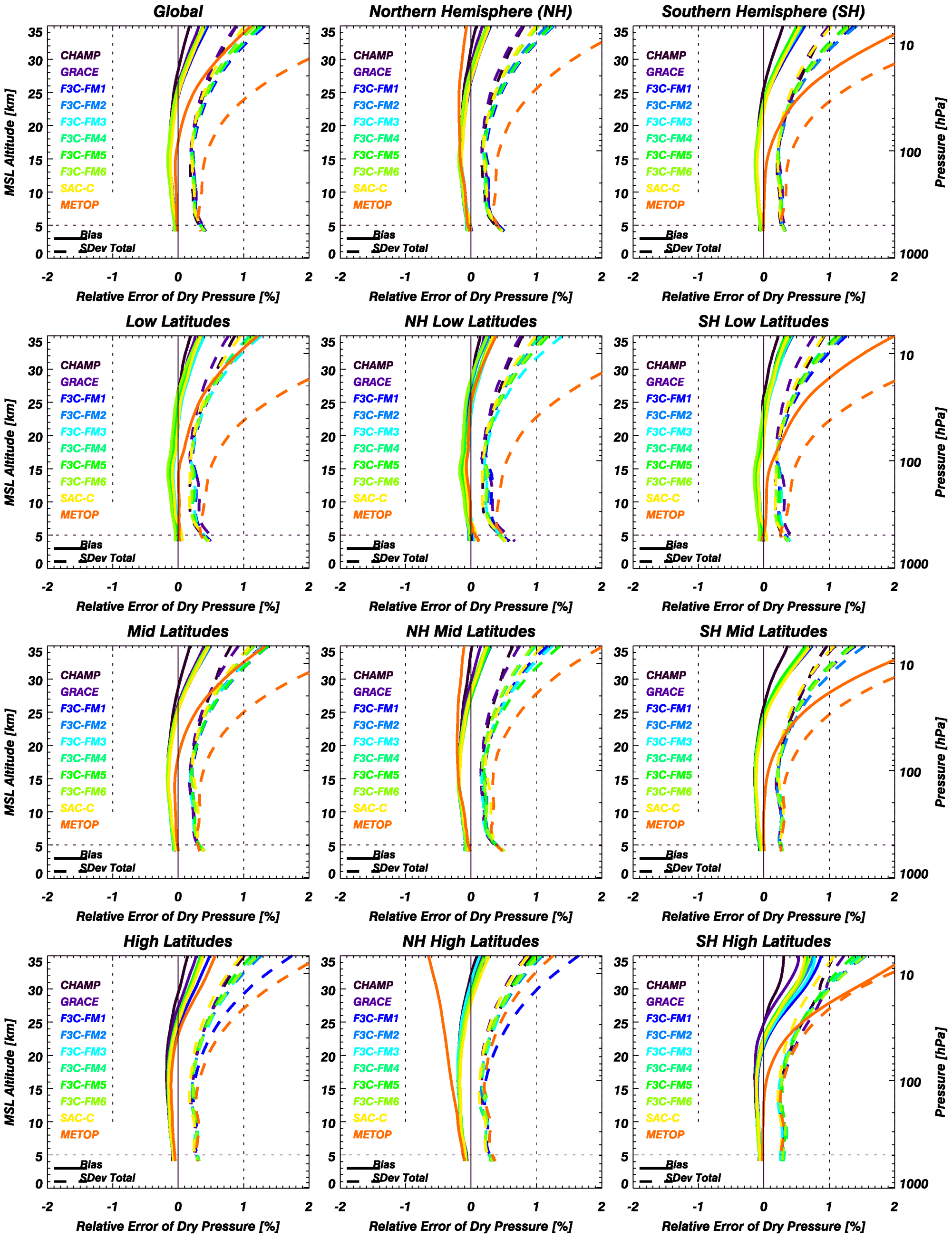

Figure 1.5: Dry pressure validation results using the standard OPSv5.6 processing of all satellite data available in July 2008. Solid lines denote RO minus ECMWF systematic differences, dashed lines show standard deviations.

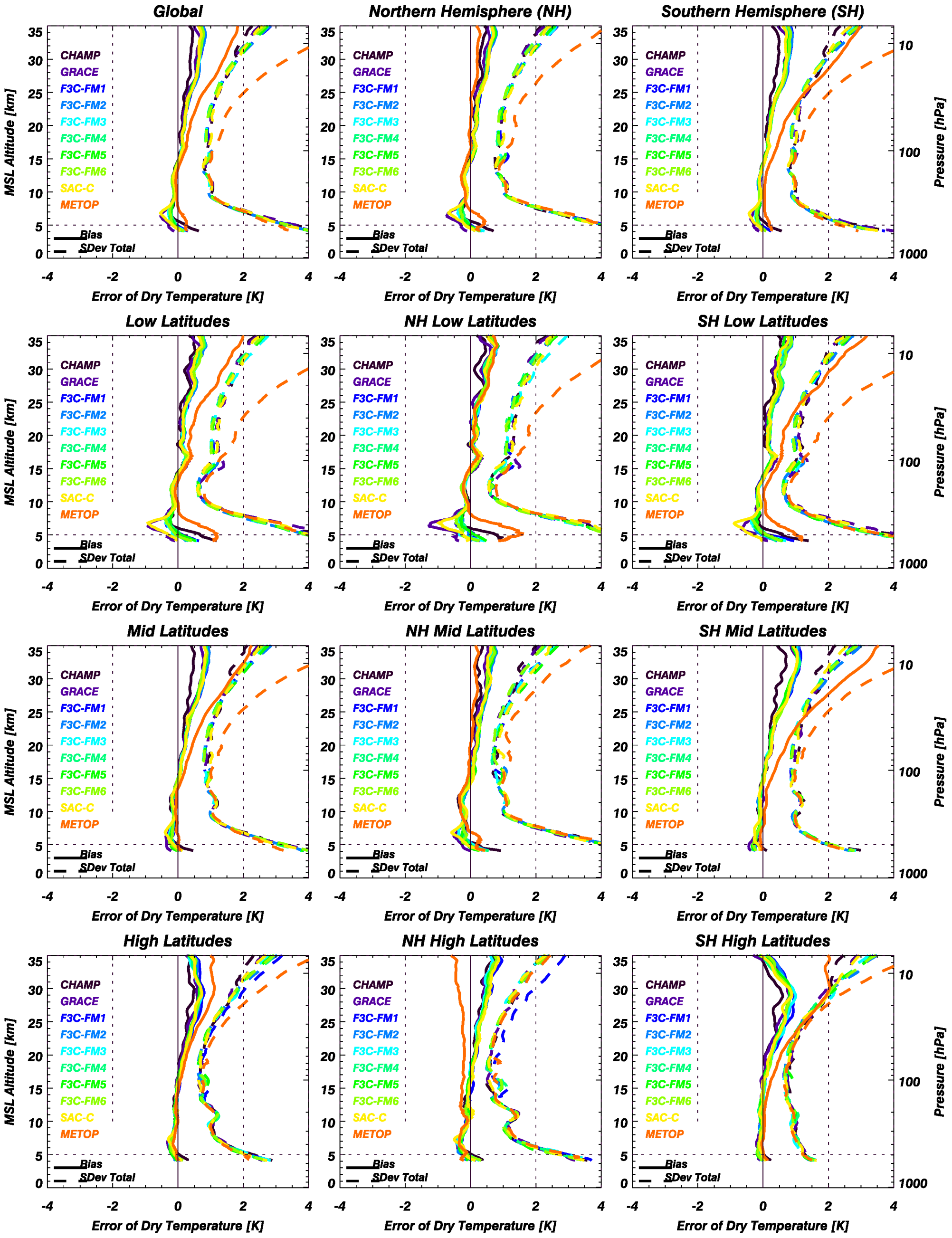

Figure 1.6: Dry temperature validation results using the standard OPSv5.6 processing of all satellite data available in July 2008. Solid lines denote RO minus ECMWF systematic differences, dashed lines show standard deviations.

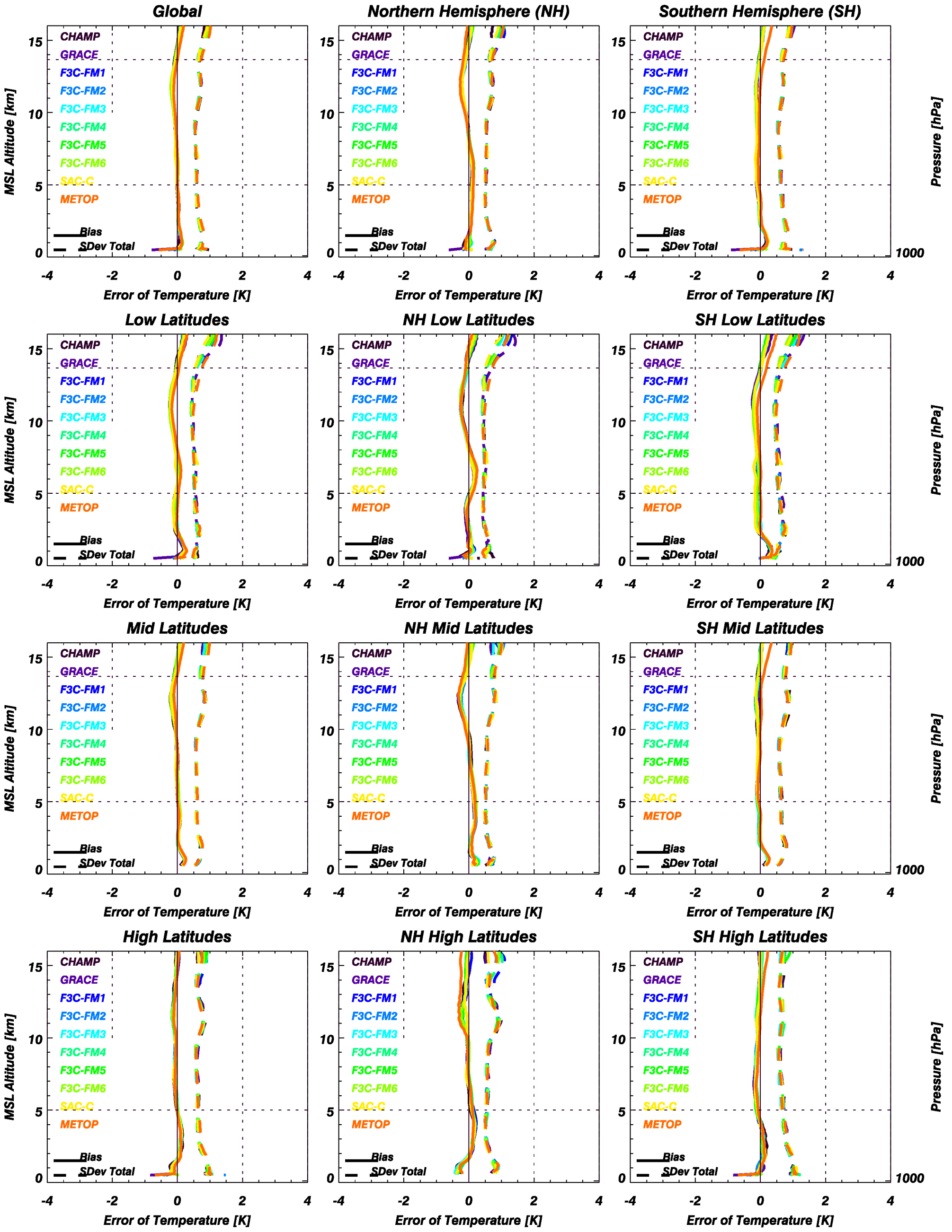

Figure 1.7: Physical temperature validation results using the standard OPSv5.6 processing of all satellite data available in July 2008. Solid lines denote RO minus ECMWF systematic differences, dashed lines show standard deviations.

separately shown), which is given in percent, gives the retrieval to a priori error ratio calculated in the optimal estimation and indicates where background information dominates observed information or vice versa. Below 16 km (the moist-air retrieval is performed only below 16 km), the RAER profile for temperature retrieval increases with decreasing altitude. Below approximately 12 km, the monthly mean 10°-zonal mean temperature RAER is larger than 50 % (i.e., background information about as influential in the retrieval as observation information), below 10 km it is larger than 70 % (background information starting to dominate the retrieval), and below 6 km at high latitudes and below 10 km at low latitudes the temperature RAER is even larger than 80 % (M. Gorfer, pers. comm., August 2013). These values indicate that background information dominates observed information below about 10 km (RAER $>$ 70 %) and RO tropospheric temperature profiles are therefore not independent from ECMWF a priori information.

Validation of Tropospheric Specific Humidity Profiles

Specific humidity is obtained together with physical temperature (see Appendix A) and validation results are shown in Figure 1.8. Systematic differences between RO and ECMWF tropospheric specific humidity show more variability than tropospheric temperature, standard deviation is larger as well. This results from a stronger weighting of RO information in the retrieval of humidity than in the retrieval of physical temperature. Monthly mean 10°-zonal mean specific humidity RAER indicates that RO observed information begins dominating background information (RAER $<$ 70 %) below about 9 km at low latitudes and below about 4 km at high latitudes in the summer hemisphere (M. Gorfer, pers. comm., August 2013).

Systematic differences between RO and ECMWF specific humidity are similar for all satellites and amount approximately to within ±10 %. The systematic difference is negative below about 3 km to 5 km, positive from 3 km/5 km to 10 km, and very close to zero (<5 %) above. The standard deviation is largest within about 6 km to 12 km, where it can be larger than 40 %.

This quality of RO-derived tropospheric humidity data is reasonably good overall, in particular the biases smaller than 10 % indicate the value of the data.

1.3 Temporal Evolution of Data Quality

Section 1.2 showed some remarkable features of data quality of selected data sets provided by each satellite. However, since it is possible that some of these features do not systematically occur in all data sets, the temporal evolution of the whole RO record available since 2001 is analyzed.

The temporal evolution of bending angle quality is investigated from the median of the bending angle bias, the median of the bending angle noise (statistics is performed on a daily

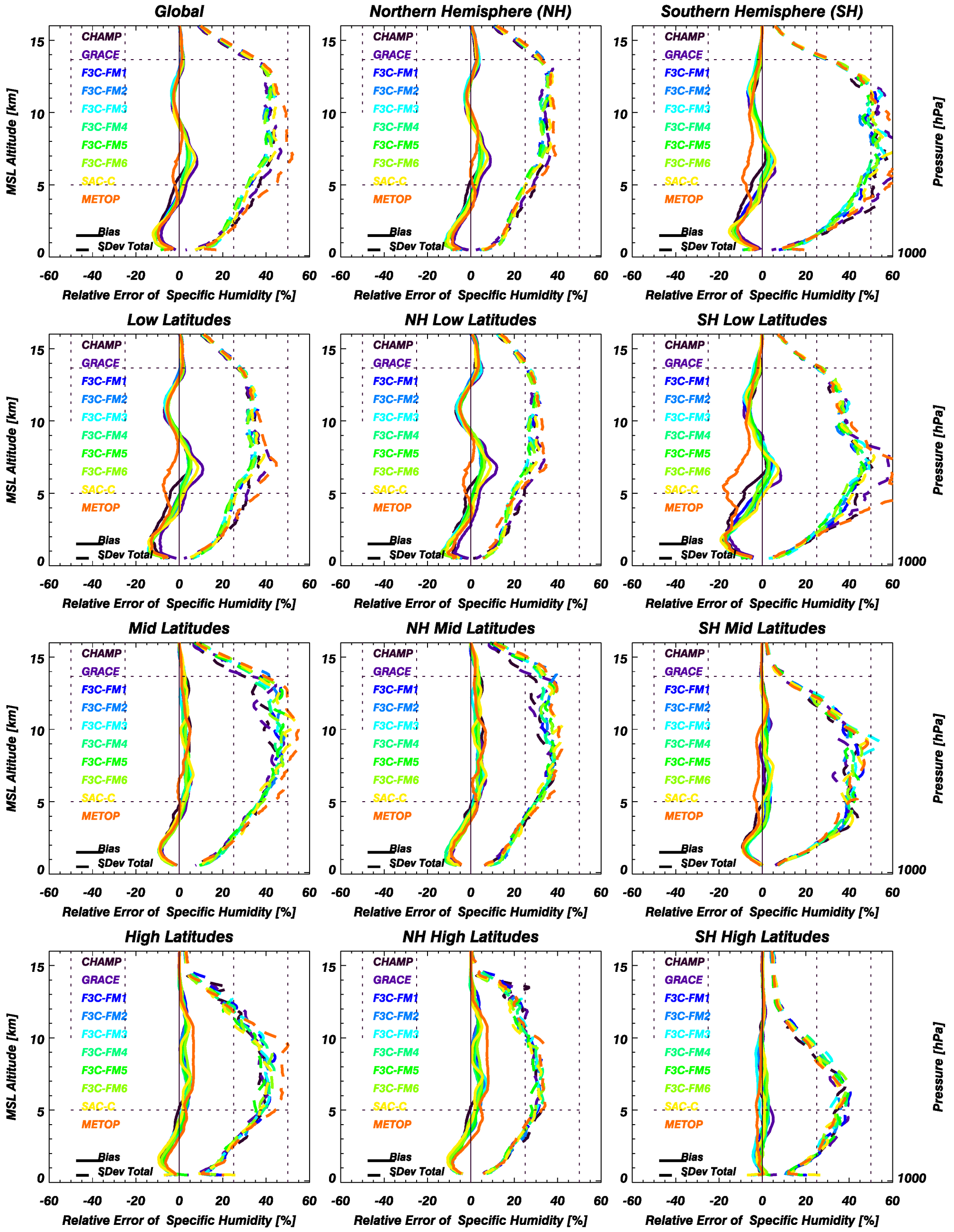

Figure 1.8: Specific humidity validation results using the standard OPSv5.6 processing of all satellite data available in July 2008. Solid lines denote RO minus ECMWF systematic differences, dashed lines show standard deviations.

basis) and the daily mean of zRAER50[20] values. Only high quality profiles, i.e., bending angle QF = 0 and QF = 2, refractivity, and dry temperature/physical temperature QF = 0 entered into the statistics.

The top panel of Figure 1.9 shows the temporal evolution of bending angle bias relative to MSIS. Temporal mean values are shown on the left hand side of the panel. The bending angle bias is slightly negative for all satellites. The temporal mean value is largest for C/NOFS (−0.20 µrad) and smallest for TerraSAR-X (−0.05 µrad). Data from TerraSAR-X also show the largest temporal variability.

To better understand the nature of different RO records, the middle panel of Figure 1.9 shows the temporal evolution of bending angle noise. Smallest bending angle noise (1.04 µrad in temporal mean) is found for MetOp-A, largest noise (8.0 µrad in temporal mean) is found for TerraSAR-X. The reason for this very larger TerraSAR-X noise is still unknown at the current stage but indicates serious problems with either the instrument, the satellite software, or excess phase and orbit processing. Given this limited quality of the current TerraSAR-X data, we will therefore not use these data for the MIPAS[21], GOMOS[22], and RAOB[23] validation.

CHAMP noise is smallest at the beginning of the observation period. After an update of the software onboard CHAMP in March 2002 (J. Wickert, GFZ, pers. comm. November 2009) the bending angle noise increased from approximately 4 µrad to 5 µrad, afterward it remained comparatively constant with time. Different data noise of SAC-C in 2001/2002 and after 2006 might result from different UCAR/CDAAC excess phase and orbit information processing versions (2005.3090 in 2001/2002 and 2010.2640 from 2006 onwards). From 2006 onwards, F3C, GRACE-A, and SAC-C bending angle noise is similar. It amounts to 2.32 µrad for F3C and 2.66 µrad for GRACE-A, for SAC-C it is slightly larger. C/NOFS bending angle noise is again larger than SAC-C noise and reaches almost CHAMP level (4 µrad in temporal mean).

Bending angle data quality at high altitudes (between 50 km and 80 km impact height) determines the degree of background information at lower altitudes (e.g., at 30 km). Better data quality is reflected in higher transition heights, where background information equals observation information; we take here the zRAER50 values as indicator of these transition heights (more precisely, RAER values near 70% may mark this transition but zRAER50 equally well illustrates the relative performance of the different satellites).

The temporal evolution of daily mean zRAER50 values is shown in the bottom panel of Figure 1.9. Nearly all CHAMP profiles are observation dominated below about 41.2 km, TerraSAR-X profiles are observation dominated below about 38.3 km. zRAER50 values then increase when evaluating C/NOFS (42.8 km), SAC-C (44.7 km), GRACE-A (45.6 km),

---

[20] Impact altitude, where retrieval to apriori error ratio equals 50 %

[21] Michelson Interferometer for Passive Atmospheric Sounding

[22] Global Ozone Monitoring by Occultation of Stars

[23] Radiosonde Observation (Rawinsonde Observation)

F3C (47.4 km), MetOp-A (56 km), and MetOp-B (54.3 km) data, respectively.

1.4 Study of the Consistency of Climatologies for Understanding RO Errors

The understanding of differences of RO data derived from different satellites is crucial when utilizing the RO record for climate studies. Previous studies investigated the consistency of sets of co-located single RO profiles. Hajj et al. [Haj+04] compared co-located occultations observed by CHAMP and SAC-C. After removal of expected atmospheric variability they found that single profiles agree to within 0.5 K between 5 km and 20 km altitude. Schreiner et al. [Sch+07] compared co-located F3C profiles and found that the refractivity RMS[24] difference between 10 km and 20 km is less than 0.2 %.

Foelsche et al. [Foe+09a] and Foelsche et al. [Foe+09b] analyzed systematic differences between seasonal mean 10°-zonal mean climatologies from CHAMP and F3C. They found that after subtraction of the estimated respective sampling errors, climatologies from different F3C satellites agree to within 0.1 K almost everywhere between 8 km and 35 km altitude. Differences between F3C and CHAMP climatologies rarely exceed 0.2 K provided that data from the same processing center are used.

In the following the approach of Foelsche et al. [Foe+09a] and Foelsche et al. [Foe+09b] is applied to investigate systematic differences of dry temperature climatologies between CHAMP, SAC-C, GRACE-A, F3C, and MetOp-A. We again analyze on July 2008 data as a representative example.

1.4.1 Spatial and Temporal Sampling

The satellite orbit altitude and inclination determine the geographic locations of RO events. While the orbit altitude determines the distance from the mean tangent point location to the LEO[25] satellite, the orbit inclination determines the geographical coverage of RO measurements. Only near-polar orbiting satellites have the potential to perform RO measurements at high latitudes.

The geographic distribution (i.e., latitudinal and longitudinal event statistics) of high quality RO measurements performed in July 2008 is shown in Figure 1.10. Comparison of CHAMP, SAC-C, GRACE-A, F3C and MetOp-A allows to investigate the impact of different orbit characteristics on the latitudinal distribution of RO events. CHAMP and GRACE-A fly in orbits with very high inclination (87.2° and 89.0°, respectively), the sun-synchronous satellites SAC-C and MetOp-A have orbit inclinations of 98.2° and 98.7°, respectively, and the F3C satellites are in orbits with only 72° inclination. The smaller

---

[24] Root Mean Square

[25] Low Earth Orbit

inclination of F3C limits the number of RO events beyond about 55° latitude. While the number of F3C measurements continuously decreases beyond this latitude, it remains stable up to 80° latitude for CHAMP and GRACE-A. The meridional event distribution (right panel) of all RO measurements is rather uniform.

1.4.2 Differences in Dry Temperature Climatologies in July 2008

Monthly mean 10°-zonal mean climatologies of different satellites are calculated according to Pirscher [Pir10]. Differences of these climatologies from July 2008 are investigated relative to the satellite mean climatology.

Figure 1.11 shows latitude-height zonal bands of dry temperature differences of CHAMP, GRACE-A, SAC-C, F3C, and MetOp-A relative to the satellite mean of all satellites except the data from both MetOp satellites (multi-satellite mean). The data from the MetOp satellites is excluded from the climatology dataset and also from the validation dataset due to one remaining issue which will be mentioned below.

Comparison with estimated sampling errors (not shown) reveals that disparities are primarily caused by differences in sampling times and locations of RO events. This means that the differences are dominated by the sampling errors of each climatology [see, e.g., Foe+11]. The quantitative estimation of the sampling error allows to subtract it from a climatology. Systematic differences between data derived from different satellites are calculated from sampling error subtracted single satellites climatologies, which are compared to the sampling error subtracted satellite mean climatology.

Figure 1.12 shows dry temperature deviations of all sampling error subtracted climatologies relative to the satellite mean (without data from both MetOp satellites). Since data from MetOp-A is not included in the satellite mean climatology it exhibits a completely different structure compared to those from the other satellites. For all other satellites it can be seen that almost everywhere the differences between the satellite mean climatology and the single satellite climatologies are smaller than ±0.25 K. Inspecting Figure 1.12 in more detail we can see that CHAMP and GRACE temperatures are slightly cooler than other satellite temperatures – more pronounced in the champ data. On the other hand SAC-C data is warmer over the northern polar region.

In global mean, the differences remain within 0.1 K, however, at tropical latitudes they even remain within 0.05 K.

1.4.3 Temporal Evolution of Dry Temperature Consistency

The top, middle, and the bottom panels of Figure 1.13 show monthly mean dry temperature records relative to the monthly multi-satellite mean [see also Foe+11].

The largest single-satellite difference relative to the multi-satellite mean is found for MetOp-A ($\Delta T = -0.41\,\mathrm{K}$) followed by MetOp-B ($\Delta T = -0.24\,\mathrm{K}$). Due to this strong difference between the MetOp satellites and all other satellites we decided to still exclude the MetOp satellites from our climatology and validation dataset (for the MIPAS, GOMOS, and RAOB validation). This feature can currently not be explained and is under strong investigation since due to the increasing data loss of the F3C we strongly need the data from the MetOp satellite.

Apart from the MetOp satellites the largest single-satellite difference relative to the multi-satellite mean is found for C/NOFS ($\Delta T = -0.27\,\mathrm{K}$), which is a satellite in low inclination and samples tropical atmospheric conditions only.

Focusing on low latitudes, where the sampling error is distinctively smaller compared to high latitudes, yields largest differences again for MetOp-A ($\Delta T = -0.49\,\mathrm{K}$ – larger than in the global dataset) followed by MetOp-B ($\Delta T = -0.10\,\mathrm{K}$).

Excluding MetOp-A and TerraSAR-X from the statistics yields best agreement between the satellites. C/NOFS, CHAMP, and GRACE-A ($\Delta T = -0.07\,\mathrm{K}$, $\Delta T = -0.03\,\mathrm{K}$, and $\Delta T = -0.02\,\mathrm{K}$, respectively) are somewhat cooler than the other satellites, SAC-C ($\Delta T = 0.03\,\mathrm{K}$) somewhat warmer. The F3C satellite data agree to within $\pm 0.01\,\mathrm{K}$.

The somewhat colder CHAMP, C/NOFS, and GRACE-A data can be explained by the effect of background information at high altitudes: The OPSv5.6 retrieval uses background information provided by ECMWF short-term forecasts. Studies evaluating the quality of ECMWF data [e.g., BKF07; Foe+08; Gob+05] showed that ECMWF temperatures are somewhat cooler than RO temperatures at high altitudes (approximately 1 K at an altitude of 35 km). RO profiles with lower background/observation transition heights are more strongly affected by this bias than profiles with higher transition heights.

Remaining peaks shown in the bottom panel of Section 1.3 are attributable to insufficient sampling by some satellites. The CHAMP climatology for July 2006, e.g., only contains data from July 1, 2006. The climatologies from F3C/FM-3 for March 2008 are calculated from data from March 1 to March 7, 2008 only and the climatologies from F3C/FM-3 and SAC-C for February 2009 both primarily contain data from the first half of the month. Finally, the SAC-C climatology for August 2011 is calculated from data from August 2 and August 3, 2011 only. These example months point at the importance to check data availability, to provide sampling error estimates for climatologies, and to check data quality.

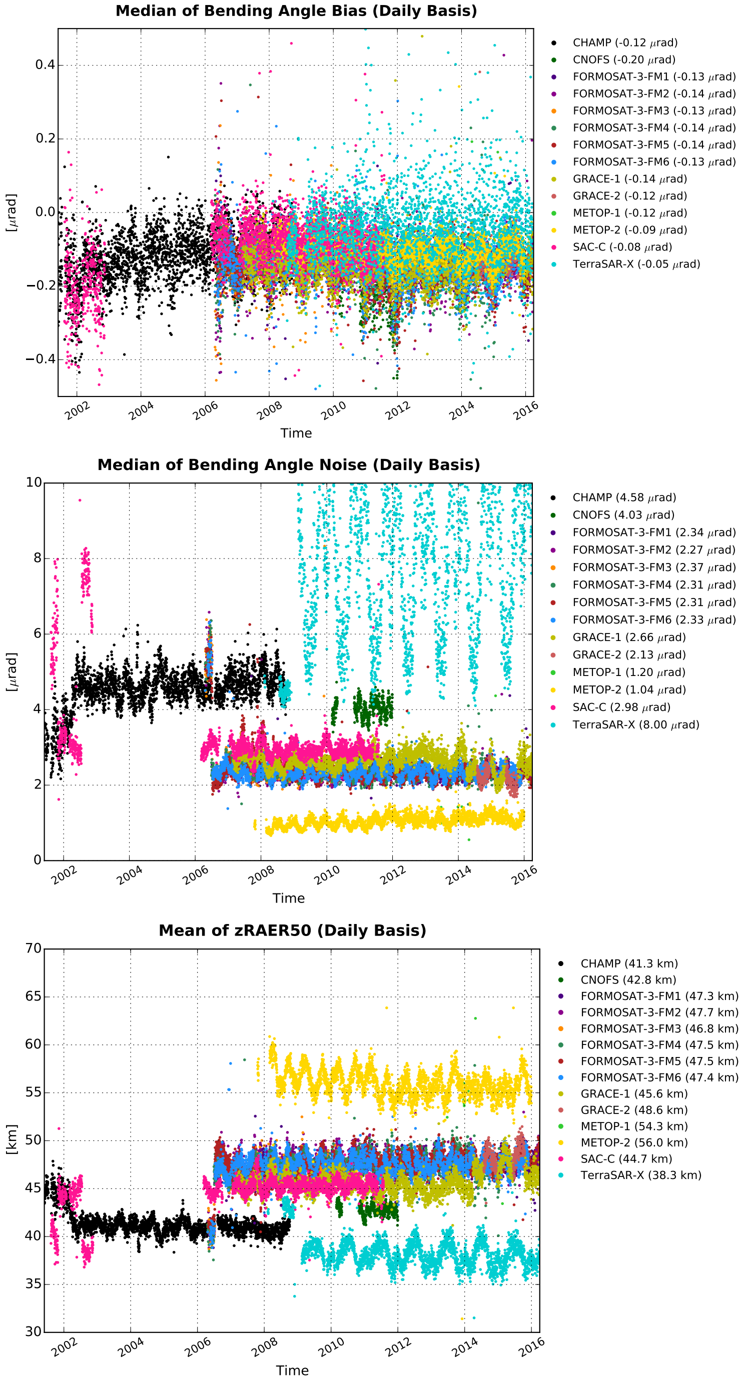

Figure 1.9: Time series of the daily median bending angle bias (top), daily median bending angle noise (standard deviation) (middle), and daily mean zRAER50 values (bottom) of different satellite data from 2001 to 2016.

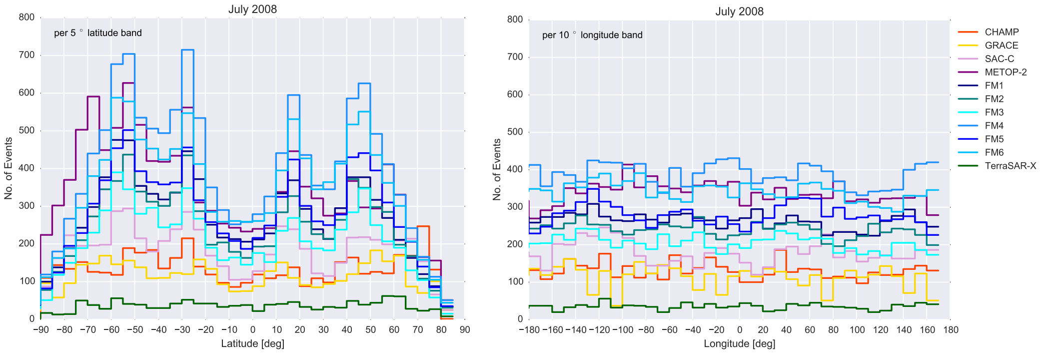

Figure 1.10: Event statistics as a function of latitude (number of RO events per 5° latitude band, left) and longitude (number of RO events per 10° longitude sector, right) in July 2008 for CHAMP, SAC-C, TerraSAR-X, GRACE-A, FM-1, FM-2, FM-3, FM-4, FM-5, FM-6, and MetOp-A, respectively.

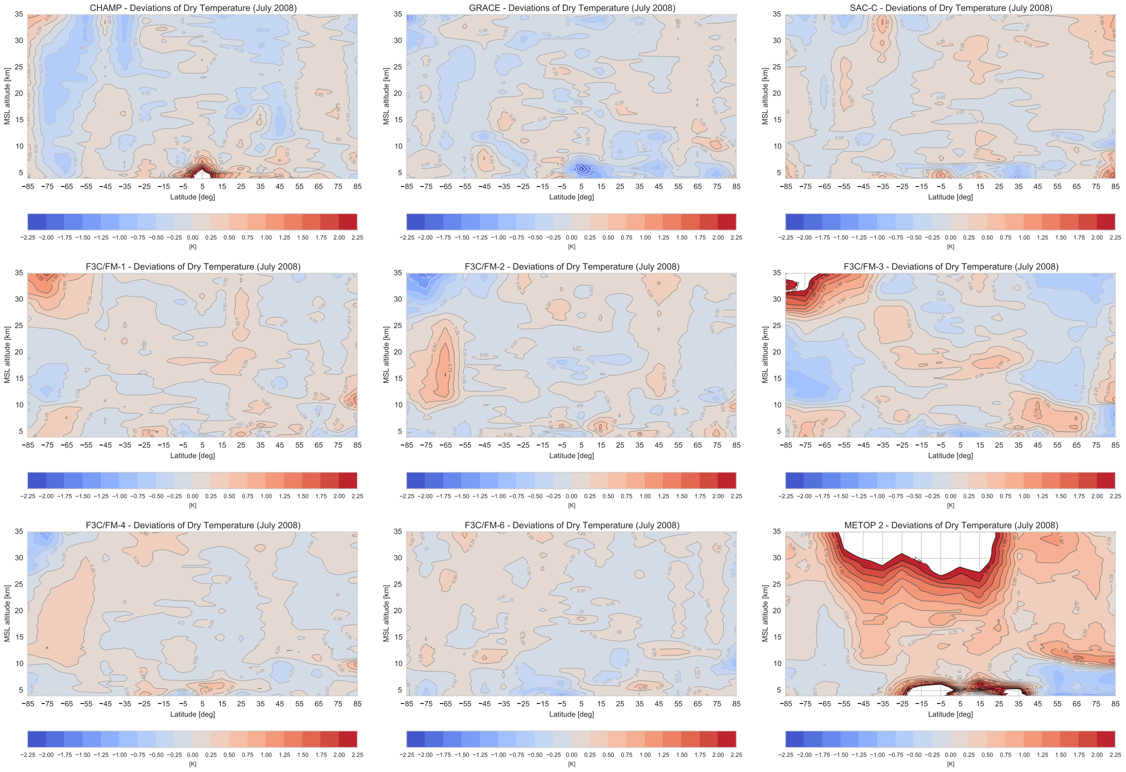

Figure 1.11: Differences between dry temperature single-satellite climatologies relative to the multi-satellite mean climatology in July 2008. Results are shown for CHAMP, GRACE-A, SAC-C, FM-1, FM-2, FM-3, FM-4, FM-6, and MetOp-A, respectively.

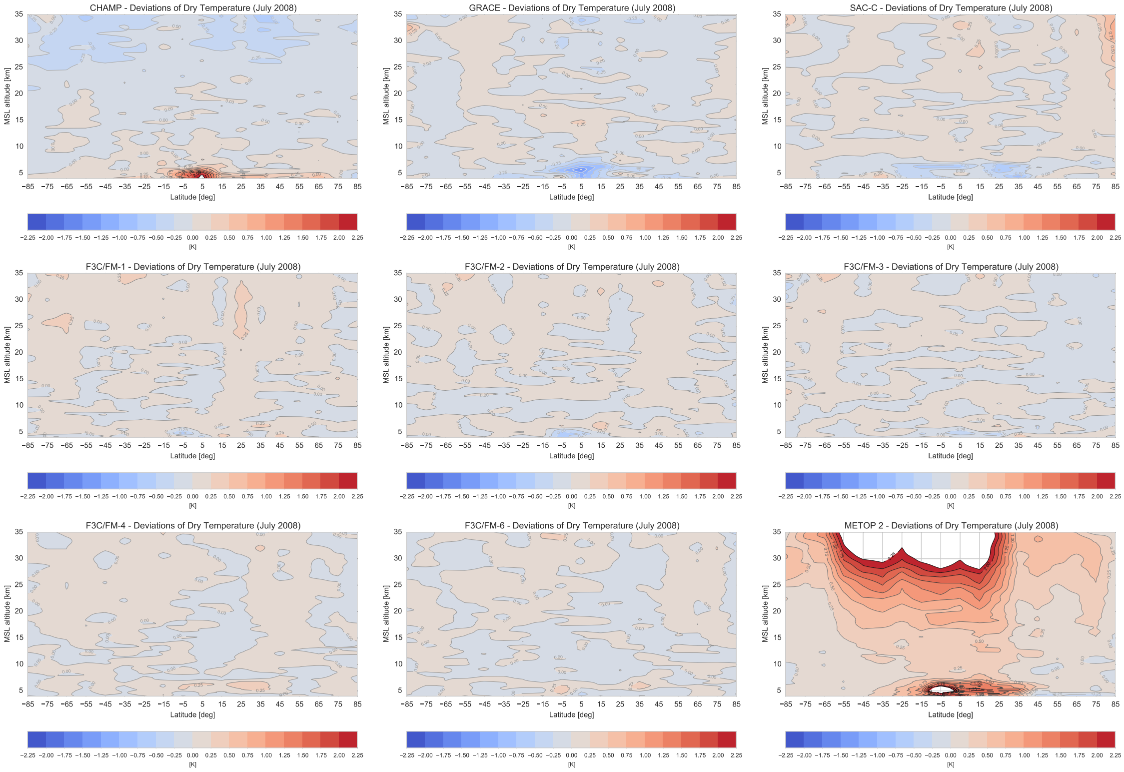

Figure 1.12: Sampling error corrected differences between dry temperature single-satellite climatologies relative to the multi-satellite mean climatology in July 2008. Results are shown for CHAMP, GRACE-A, SAC-C, FM-1, FM-2, FM-3, FM-4, FM-6, and MetOp-A, respectively.

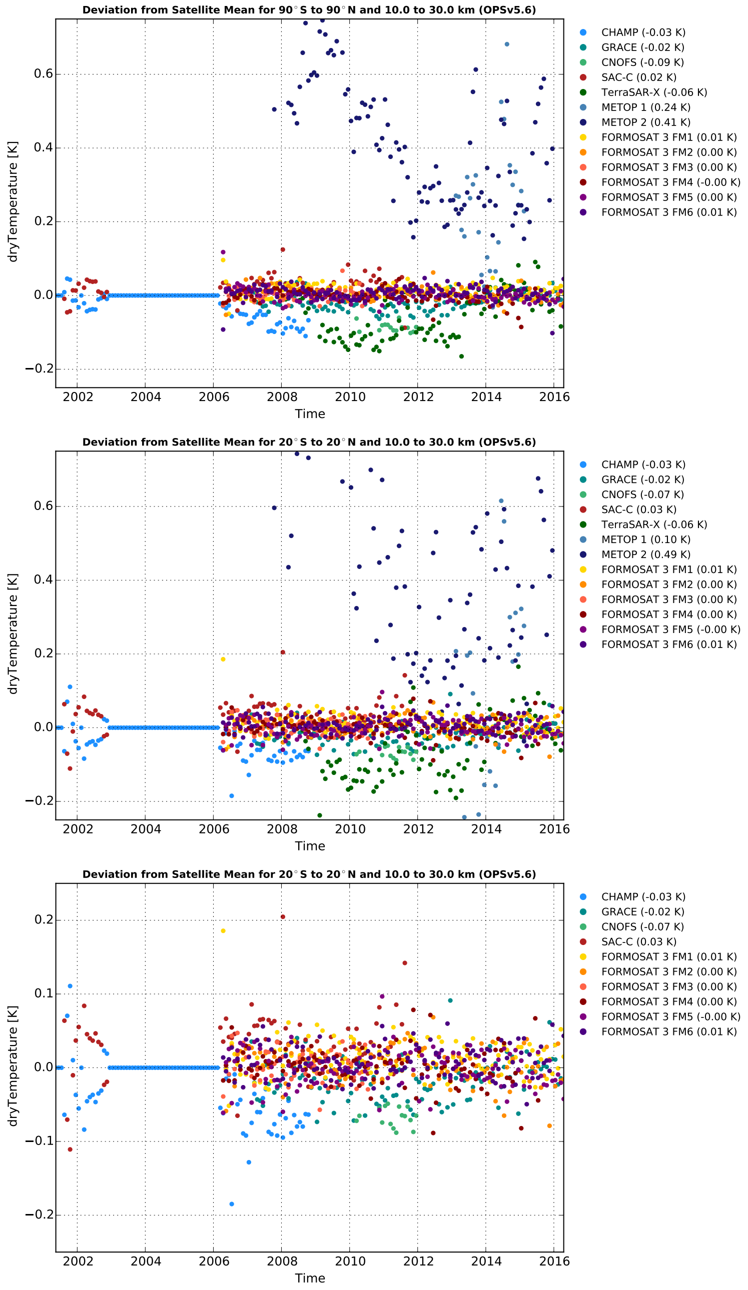

Figure 1.13: Temporal evolution of temperature records of different satellites relative to the multi-satellite mean from 2001 to 2016. Results from OPSv5.6 processing are shown for CHAMP, SAC-C, GRACE-A, all F3C satellites, C/NOFS, MetOp-A, MetOp-B , and TerraSAR-X, respectively. The top panel shows global mean differences (90°S to 90°N, 10 km to 30 km). The middle and bottom panels show differences at low latitudes (20°S to 20°N) with and without MetOp satellites and TerraSAR-X data included.

2 MIPAS, GOMOS, and RAOB Validation Results

2.1 MIPAS Validation by RO for the Period 2002 to 2012

2.1.1 Input Data Flows and MIPAS-RO Collocations 2002 to 2012

The candidate data input flow consisted of the MIPAS ML2PPv6.0[1] and the MIPAS ML2PPv7.03[2] processor data 2002 to 2012 (the fully reprocessed dataset including the "full resolution" and the "optimized resolution" mission phases; amongst other changes the MIPAS ML2PPv7.03 dataset contains ECMWF corrected altitudes). The reference input data flow of OPSv5.6 (2002 to 2012 and beyond) was obtained from the satellites CHAMP, COSMIC[3] (major fraction), C/NOFS, SAC-C, and GRACE. 300 km/3 h space-time distance (cf. [Sof+08]) was used as collocation criterion. MIPAS temperature and pressure were validated against RO for the collocated ensemble of profiles, on a global scale (and for various large-scale zonal bands). The profiles were interpolated to an equidistant log-pressure grid with 350 levels between 1000 hPa to 5 hPa (for details cf.Subsection 3.1.4). A vertical smoothing was performed on both measurements as explained in Subsection 3.1.4 using an effective resolution of 3 km.

Figure 2.1 shows, for monthly data over the time period studied, the number of profiles from the candidate (MIPAS) and reference (RO) data sources, together with the number of collocated profiles (L.H.S. ordinate) found in each month. In addition, Figure 2.2 shows representative collocation distributions for July 2003 and July 2008 on global geographic maps. The color bar indicates the space-time distance between the validated and the reference profile. The time distance is converted to a spatial distance by applying a conversion factor of 100 km per hour, reflecting a typical stratospheric wind speed. A more detailed view on such collocation distributions for the whole ENVISAT[4] period can be found on the Wegener Center's MMValRO[5] validation website `http://validate.globclim.org`.

The MIPAS ML2PPv7.03 and ML2PPv6.0 data stream, retrieved from ESA[6]'s processing

---

[1] ESA ML2PP processor version 6.0

[2] ESA ML2PP processor version 7.03

[3] Constellation Observing System for Meteorology, Ionosphere, and Climate

[4] Environmental Satellite

[5] Multi-Mission Validation by Satellite Radio Occultation

[6] European Space Agency

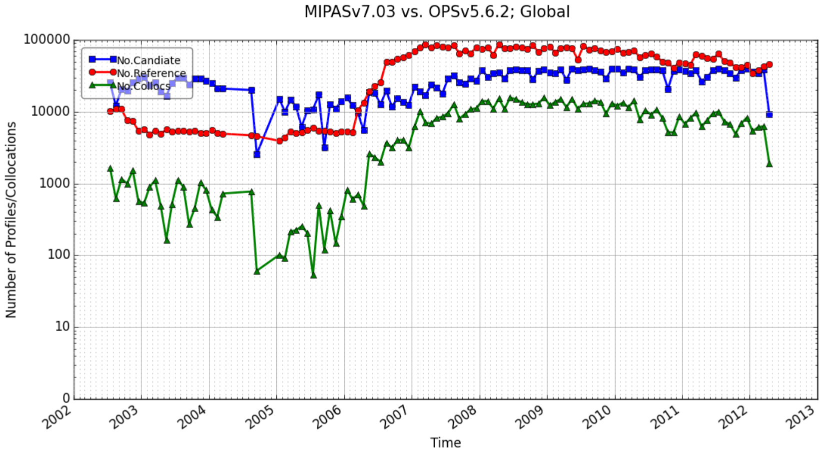

Figure 2.1: Overview on the number of events of MIPAS and RO data, as well as on the collocated profiles from 2002 to 2012.

centers, features typically about 20 000 to 40 000 profiles per month from July 2002 until April 2012 (cf. Table 3.1), except in the gap between the full resolution period and the optimized resolution period in 2004 (this data should not be used). The RO data stream is small, below 5000 profiles per months, before the “COSMIC data era” starts as of mid 2006, from which on 40 000 to 70 000 RO profiles are available per month (cf. Table 3.4).

Reflecting these input data streams, the number of collocated profiles is small up to June 2006, generally about 1000 collocations per month and high from August 2006 onward with about 10 000 collocations per month. The collocations are more or less equally distributed over the globe and evidently more sparse before the “COSMIC data era” (cf. Figure 2.2).

2.1.2 MIPAS Temperature Validation by RO

Figure 2.3 and Figure 2.4 show the overall results for the validation of the physical temperature of MIPAS. It has to be noted here once more that below 16 km the RO physical temperature is correlated with the ECMWF short term forecast field because of the 1D-Var[7] approach.

Detailed results for different altitude layers (from 500 hPa to 200 hPa – 4.9 km to 11.4 km – to 20 hPa to 10 hPa – 27 km to 32 km – layers) and individual months can be viewed via the Wegener Center’s MMValRO validation website `http://validate.globclim.org`; the reader may directly use this online information resource in parallel to reading this chapter.

Figure 2.4, bottom panel, contains the estimated 90 % RO uncertainty estimates as de-

---

[7] 1-Dimensional Variational Data Assimilation

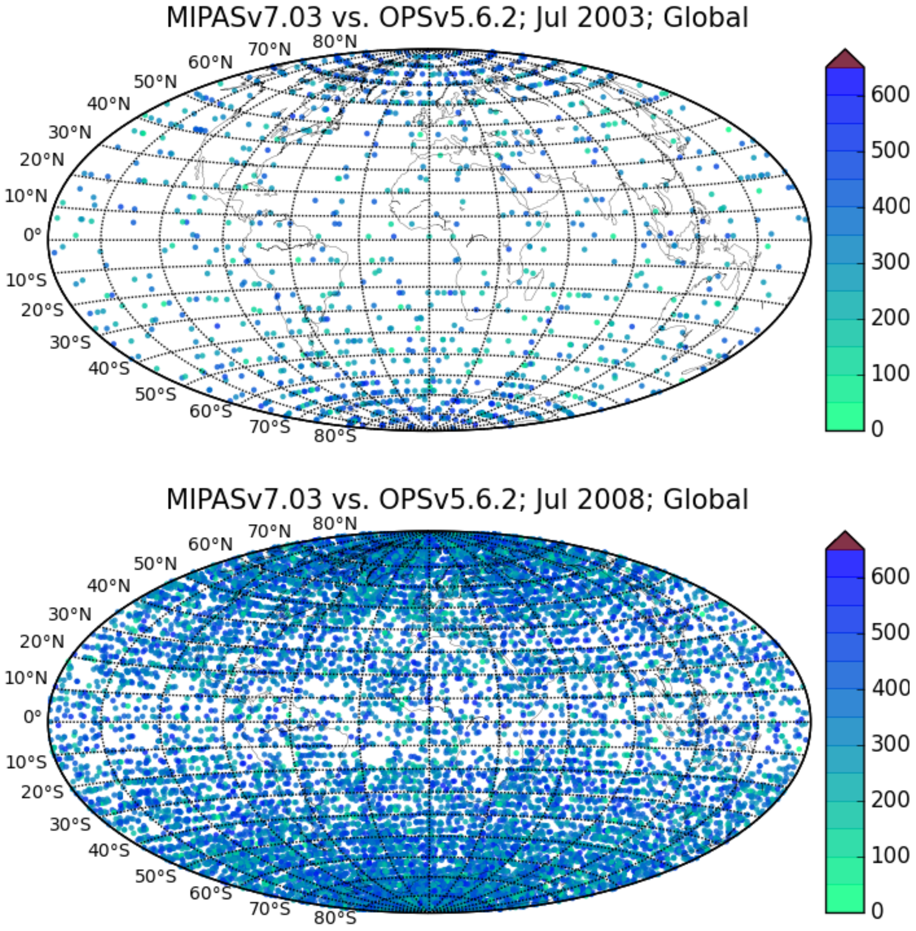

Figure 2.2: Collocation distribution for MIPAS, months July 2003 and 2008.

scribed in RO literature [SP+11a; SP+11b] as dark gray error bars. As a reference information on RO it is relevant to know, as available from RO literature [SP+11a; SP+11b], that the OPSv5.4[8] monthly-mean RO temperature data have a systematic error of <0.3 K within 8 km and 25 km, increasing to <0.8 K up to 35 km and down to 5 km, respectively. The OPSv5.6 has similar error characteristics in the UTLS[9], as comparison against OPSv5.4 shows, so the same error estimates apply and were built into the visualized 90 % RO uncertainty ranges. Also RO data are long-term stable, i.e., based on literature information ([SP+11b; Ste+13], and references therein) their systematic temperature error over 2002 to 2012 is expected to change by <0.3 K per decade over this ten year period. The validation can be interpreted with this error information on RO in mind that is for convenience also visualized in form of the dark-grey uncertainty ranges.

Generally speaking, the systematic difference between MIPASv7.03 and RO is within ±1.5 K at all heights and throughout the full ENVISAT period, which confirms all MIPAS data are overall in the right ballpark, there is no illegitimate, i.e., non-physical outliers in terms of monthly-evolving MIPAS climatology.

The results show three different regimes: On the one hand a difference between the full resolution period and the optimized resolution period of MIPAS can be seen (bias blow 15 km; smaller standard deviation in 2005 compared to 2003). On the other hand the global validation altitude slice (cf.Figure 2.3) shows a transition to another regime (change in the bias structure of about ±0.5 K at an altitude of about 16 km) in 2006. Globally once also finds a change from a more positive to a more negative bias structure between 16 km to 30 km. Trying to resolve this feature for latitudes (cf.`http://validate.globclim.org`) it turns out that the time series is sparse for the diverse latitude bands. One can see these changes partially but the continuous change cannot be displayed. A CHAMP-only validation analysis has shown the same changes. Hence, this jump in the structure of the systematic difference does not result from the change in the RO record which changes from a single-satellite (CHAMP only) to a multi-satellite one but has to be a matter of other reasons, e.g. that the ECMWF has two big changes in 2006 – on the one hand the model resolution was increased from T511L60 to T799L91 (from 60 to 91 vertical levels) in February 2006 and on the other hand the variational bias correction of the nadir sounder data was introduced in September 2006 (together with several further model system changes).

A comparison between the old MIPASv6.0 validation dataset and the new MIPASv7.03 full dataset shows that they are generally in a good agreement. Table 2.1 shows the mean temperature bias and standard deviation (in Kelvin) of MIPASv6.0 versus OPSv5.6 (top rows) and of MIPASv7.03 versus OPSv5.6 (bottom rows) for different regions (GLO[10] (90°S

---

[8] Occultation Processing System version 5.4

[9] Upper Troposphere–Lower Stratosphere

[10] Global

to 90°N), NHL[11] (60°N to 90°N), NML[12] (30°N to 60°N), NLL[13] (0° to 30°N), SLL[14] (0° to 30°S), SML[15] (30°S to 60°S), SHL[16] (60°S to 90°S)) for the the full ENVISAT period. The top two parts of Table 2.1 show MIPASv7.03 separated into FR[17] and OR[18], the bottom two parts show MIPASv6.0 separated into FR and OR.

For OR MIPASv6.0 and MIPASv7.03 are rather similar and exhibit no significant difference both for the global statistics as well as for the results separated into latitude bands. For FR this is different. On a quick view it seems that MIPASv6.0 performs better compared to MIPASv7.03 since the biases are smaller. But on a closer look the opposite is true. The reason for that is that when looking at the whole MIPASv7.03 (combined FR and OR) dataset it far more consistent in itself. Within the MIPASv6.0 dataset there is a jump between FR and OR of about ∼0.5 K which is not the case for the MIPASv7.03 dataset (cf. Figure 2.4). This better consistency allows a better and more smoothly usage of the MIPASv7.03 dataset in climate applications.

From 15 km to 25 km over the lower stratosphere the temperature quality of MIPAS can be considered very good, they generally agree with RO within ∼0.5 K (more precisely from 17 km, but this is only visible in height resolved plots, see examples further below and see the validation results at `http://validate.globclim.org`).

When resolving the altitude-time plots with latitude (cf.`http://validate.globclim.org`) an interesting feature arises between about 16 km to 30 km (parts of the used RO temperature data which are independent from the ECMWF fields): For the low latitudes a more positive bias occurs whereas for the mid- and high latitudes the systematic difference of MIPAS against RO is more negative.

Also from 25 km to 35 km the agreement is good and generally within 1 K. Overall above ∼15 km (more precisely ∼17 km) there is only a slight tendency of a cold bias of MIPAS relative to RO (from perhaps <0.3 K to ∼0.5 K from 17 K to 35 K), but as this is generally within the margin of the RO uncertainties no more detailed attribution shall be undertaken here.

As of Sep.2006 below ∼15 km (more precisely ∼17 km) into the upper troposphere the MIPAS temperature quality systematically degrades, with cold biases of mostly ∼1 K already above 10 km, and cold biases reaching up to about 5 K below 10 km.

In order to enable a more detailed look at the behavior of individual months beyond inspecting the altitude layers over time, the separate plots as a function of altitude that

---

[11] Northern High Latitudes
[12] Northern Mid Latitudes
[13] Northern Low Latitudes
[14] Southern Low Latitudes
[15] Southern Mid Latitudes
[16] Southern High Latitudes
[17] Full Resolution Period
[18] Optimized Resolution Period

Table 2.1: Temperature bias and standard deviation (in Kelvin) of MIPASv7.03 versus OPSv5.6 (top rows) and of MIPASv6.0 versus OPSv5.6 (bottom rows) for different regions and separated into FR and OR period. Statistics is calculated from January 2005 to December 2009.

v7.03/FR	20–200 hPa	10–20 hPa	20–50 hPa	50–100 hPa	100–200 hPa	200–500 hPa
GLO	−0.47/1.82	0.29/1.94	−0.14/1.88	−0.33/2.12	−0.68/2.02	−0.61/1.47
NHL	−0.59/1.58	0.30/1.93	−0.10/1.83	−0.44/1.80	−0.82/1.64	−0.75/1.14
NML	−0.51/1.53	0.08/1.78	−0.24/1.36	−0.47/1.83	−0.63/1.72	−0.64/0.90
NLL	−0.02/0.88	0.29/1.24	−0.11/0.72	0.24/1.12	−0.16/1.36	−0.42/1.15
SLL	0.20/1.03	0.35/1.25	0.06/0.78	0.35/1.27	0.19/1.45	−0.02/1.00
SML	−0.74/2.09	0.06/1.90	−0.33/1.93	−0.64/2.39	−0.92/2.29	−0.49/1.09
SHL	−0.61/2.03	0.39/1.92	−0.20/2.09	−0.50/2.38	−0.93/2.30	−0.90/1.74
v7.03/OR	20–200 hPa	10–20 hPa	20–50 hPa	50–100 hPa	100–200 hPa	200–500 hPa
GLO	−0.42/1.34	−0.40/1.85	−0.49/1.51	−0.17/1.52	−0.60/1.61	−0.95/1.31
NHL	−0.49/1.22	−0.43/1.80	−0.61/1.48	−0.33/1.36	−0.58/1.37	−1.03/1.38
NML	−0.53/1.27	−0.54/1.78	−0.60/1.27	−0.26/1.38	−0.71/1.54	−1.01/1.29
NLL	−0.12/0.84	−0.16/1.44	−0.12/0.82	0.30/0.89	−0.43/1.38	−0.67/0.66
SLL	−0.09/1.01	−0.28/1.43	−0.11/0.86	0.27/1.07	−0.36/1.53	−0.65/0.44
SML	−0.50/1.55	−0.50/1.92	−0.60/1.53	−0.21/1.67	−0.70/1.84	−0.92/1.13
SHL	−0.50/1.38	−0.42/1.82	−0.61/1.71	−0.38/1.66	−0.62/1.57	−0.98/1.44
v6.0/FR	20–200 hPa	10–20 hPa	20–50 hPa	50–100 hPa	100–200 hPa	200–500 hPa
GLO	−0.01/1.76	0.59/1.79	0.35/1.66	0.15/1.93	−0.21/2.08	−0.22/1.38
NHL	0.06/1.66	0.65/1.79	0.55/1.67	0.22/1.74	−0.17/1.84	−0.03/1.16
NML	−0.10/1.58	0.39/1.64	0.20/1.24	−0.02/1.67	−0.23/1.93	−0.01/1.21
NLL	0.10/0.90	0.57/1.16	0.23/0.70	0.51/1.04	−0.17/1.45	−0.71/1.69
SLL	0.24/1.10	0.56/1.19	0.31/0.74	0.55/1.23	0.04/1.64	−0.60/1.43
SML	−0.38/2.21	0.34/1.73	0.08/1.73	−0.24/2.25	−0.60/2.61	−0.33/1.41
SHL	−0.04/1.86	0.69/1.81	0.31/1.86	0.07/2.14	−0.22/2.20	−0.46/1.37
v6.0/OR	20–200 hPa	10–20 hPa	20–50 hPa	50–100 hPa	100–200 hPa	200–500 hPa
GLO	−0.47/1.29	−0.40/1.84	−0.54/1.45	−0.24/1.45	−0.65/1.56	−1.21/1.27
NHL	−0.54/1.17	−0.45/1.79	−0.62/1.46	−0.41/1.31	−0.63/1.31	−1.26/1.34
NML	−0.58/1.22	−0.56/1.77	−0.61/1.22	−0.37/1.31	−0.75/1.49	−1.35/1.28
NLL	−0.24/0.88	−0.12/1.41	−0.19/0.82	0.27/0.87	−0.65/1.45	−0.89/0.71
SLL	−0.16/1.03	−0.16/1.42	−0.21/0.85	0.22/1.02	−0.46/1.62	−0.73/0.54
SML	−0.53/1.52	−0.52/1.91	−0.61/1.47	−0.31/1.64	−0.70/1.81	−1.15/1.14
SHL	−0.56/1.29	−0.45/1.82	−0.72/1.62	−0.45/1.55	−0.69/1.48	−1.35/1.35

are available per month are useful. They show the candidate (MIPAS) validation in an altitude-resolved manner. As examples Figure 2.5 and Figure 2.6 show this detailed look for a month of the FR period (December 2003; Figure 2.5) and a month for the OR period (February 2008; Figure 2.6). The top panel of both figures shows a detailed statistical analysis of the MIPASv7.03 dataset and the bottom panel the comparison between the validation results of MIPASv7.03 and MIPASv6.0 where both datasets are compared using the same reference profiles. On the webpage `http://validate.globclim.org` detailed statistical analysis plots for the whole ENVISAT period are available.

Inspecting Figure 2.5 and Figure 2.6 clearly explains closer the nature of deviations and this type of figures is evidently a good means to more closely explore the elementary (monthly) climatological time periods that have spotted special interest.

2.1.3 MIPAS Altitude Validation by RO

Figure 2.7 and Figure 2.8 show the overall results for MIPAS altitude validation. It has to be noted here once more that below 16 km the RO physical pressure is correlated with the ECMWF short term forecast field because of the 1D-Var approach.

As for temperature discussed in the previous subsection, detailed results for different pressure layers(from 500 hPa to 200 hPa – 4.9 km to 11.4 km – to 20 hPa to 10 hPa – 27 km to 32 km – layers) and individual months can be viewed via the Wegener Center's MMValRO validation website `http://validate.globclim.org`; the reader may directly use this online information resource in parallel to reading this report.

Although RO data are long-term stable, i.e., based on literature information ([SP+11b; Ste+13], and references therein) the systematic pressure error over 2002 to 2012 is expected to change only within <0.2 % per decade over this period. The validation can be interpreted with this error information on RO in mind. The OPSv5.4 as well as the OPSv5.6 monthly-mean RO pressure data have a systematic error of <0.3 % within 5 km to 25 km, increasing <0.7 % up to 35 km. This pressure error maps to a corresponding altitude error when changing the vertical coordinate from altitude to pressure. As a rule of thumb, every 70 m of altitude mis-location leads to 1 % pressure bias, that is, as an example, 5 % pressure bias corresponds to an altitude mis-location of about 300 m to 400 m.

Figure 2.8 shows a detailed statistical analysis of the MIPASv7.03 dataset and the bottom panel the comparison between the validation results of MIPASv7.03 and MIPASv6.0 where both datasets are compared using the same reference profiles.

In the full resolution period MIPAS altitude bias against RO is larger than in the optimized resolution period and has maxima of more than 200 m. In the optimized resolution period the altitude bias against RO is about 50 m at all pressures which confirms all MIPAS data of the optimized resolution period are quite good, there is no illegitimate, i.e., truly non-physical outlier in terms of monthly MIPAS climatologies except probably January 2010. This month will be addressed later.

Comparing the new with the old validation dataset (cf. bottom panel of Figure 2.8) the improvements obtained with the MIPASv7.03 dataset can clearly be seen. The usage of the ECMWF-corrected altitudes in the mipas dataset has removed the strong seasonal dependency of the results as well as the somehow erratic behavior in the FR period.

It is visible in the results (see at `http://validate.globclim.org` for details) that in any given month the relative pressure bias is essentially the same at all UTLS altitudes. This points to the interpretation that this relative pressure bias mainly reflects an altitude allocation bias.

Table 2.2 shows the mean altitude bias and standard deviation (in percent) of MIPASv6.0 versus OPSv5.6 (top rows) and of MIPASv7.03 versus OPSv5.6 (bottom rows) for different regions (GLO (90°S to 90°N), NHL (60°N to 90°N), NML (30°N to 60°N), NLL (0° to 30°N), SLL (0° to 30°S), SML (30°S to 60°S), SHL (60°S to 90°S)) for the the full ENVISAT period. The top two parts of Table 2.1 show MIPASv7.03 separated into FR and OR, the bottom two parts show MIPASv6.0 separated into FR and OR. As mentioned above We can clearly see that there is a strong improvement that has been obtained in the MIPASv7.03 dataset. In the FR period the global bias is reduced by about 300 m through all heights except for the lowest one (200 hPa to 500 hPa) and in the OR period the strong seasonal dependency of the results is removed as mentioned above.

Figure 2.9 and Figure 2.10 show vertically resolved monthly validation results for December 2003 (as an example for the FR period) and February 2008 (as an example for the OR period). Inspecting the top panel of Figure 2.10 in detail one can see that the mean exhibits a more erratic structure below about 150 hPa. Comparing then the two different datasets in the bottom panel of Figure 2.10 one can see that the mean of MIPASv7.03 follows the median of version MIPASv6.0 in this height region. A possible reason for that could be that some features which were present in most of MIPASv6.0 datasets could be removed from most of the MIPASv7.03 datasets but is still present in some measurements.

Comparing Figure 2.10 and Figure 2.9 one can see also from this point of view that within the OR period the height alignment works better than in the FR period.

It can be seen very well from Figure 2.9 bottom panel with February 2008 as an example month for the OR period how good the improvement of the MIPASv7.03 data is: Almost the whole bias has vanished compared to the MIPASv6.0 data. An interesting feature to mention is that the shape of the mean has shifted but has not really changed. In contrast to that in the median some special features have vanished or could have been reduced (e.g. that the small increase between 60 hPa to 70 hPa or the increase starting at about 180 hPa).

As for temperature, the same type of plots is available for all months at the website `http://validate.globclim.org`. Inspecting plots like Figure 2.10 and Figure 2.9 clearly explains closer the nature of deviations and this type of figures is evidently a good means to more closely explore in a dedicated analysis the elementary climatological time periods (here individual months) that have spotted special interest.

As mentioned above, we finally look at January 2010 (cf. Figure 2.11) since it had a

Table 2.2: Altitude bias and standard deviation (in Meter) of MIPASv7.03 versus OPSv5.6 (top rows) and of MIPASv6.0 versus OPSv5.6 (bottom rows) for different regions and separated into FR and OR period. Statistics is calculated for the whole envisat period.

v7.03/FR	20–200 hPa	10–20 hPa	20–50 hPa	50–100 hPa	100–200 hPa	200–500 hPa
GLO	62/264	58/313	59/297	62/284	82/287	159/189
NHL	159/121	131/161	129/137	138/122	179/125	184/100
NML	135/126	96/151	99/135	117/128	157/138	149/90
NLL	107/165	102/194	105/190	154/202	117/182	126/105
SLL	101/189	107/218	106/211	149/224	97/220	101/114
SML	157/158	118/198	121/178	141/163	177/164	153/105
SHL	162/141	160/203	152/177	165/154	187/142	184/110

v7.03/OR	20–200 hPa	10–20 hPa	20–50 hPa	50–100 hPa	100–200 hPa	200–500 hPa
GLO	39/73	35/120	33.67/98	36/82	49/91	117/56
NHL	44/73	49/120	47.31/98	41/81	49/84	133/58
NML	39/75	25/104	27.63/82	28/75	52/99	110/52
NLL	32/46	15/64	6.82/51	43/73	46/75	78/28
SLL	31/47	19/69	11.67/59	40/70	42/74	75/25
SML	37/86	24/131	27.56/107	27/89	50/105	111/50
SHL	41/74	45/133	50.87/114	38/84	50/82	125/54

v6.0/FR	20–200 hPa	10–20 hPa	20–50 hPa	50–100 hPa	100–200 hPa	200–500 hPa
GLO	365/476	406/490	395/496	391/503	376/486	266/303
NHL	515/416	531/398	513/406	503/419	523/423	338/300
NML	537/372	564/380	557/384	558/392	530/381	295/235
NLL	438/356	625/425	624/427	604/426	430/399	334/272
SLL	322/343	421/453	418/453	416/431	308/349	259/237
SML	316/489	312/484	306/489	312/505	324/495	228/283
SHL	179/483	220/491	192/494	192/505	217/496	203/289

v6.0/OR	20–200 hPa	10–20 hPa	20–50 hPa	50–100 hPa	100–200 hPa	200–500 hPa
GLO	−8/279	−30/310	−33/303	−18/296	5/298	109/178
NHL	−45/310	−64/329	−67/325	−53/319	−41/322	88/200
NML	−26/281	−67/309	−64/303	−48/295	−3/290	92/154
NLL	−81/201	−122/246	−131/241	−82/247	−84/216	30/66
SLL	−69/186	−97/226	−106/222	−69/232	−74/200	43/54
SML	37/277	7/294	10/291	21/287	62/292	134/160
SHL	62/264	58/313	59/297	62/284	82/287	159/189

negative bias over the whole altitude range which is in contrast to all other months in the OR period. One can see that only the mean exhibits this feature. The median does not show this. In contrast, it is 0 almost over the full height range.

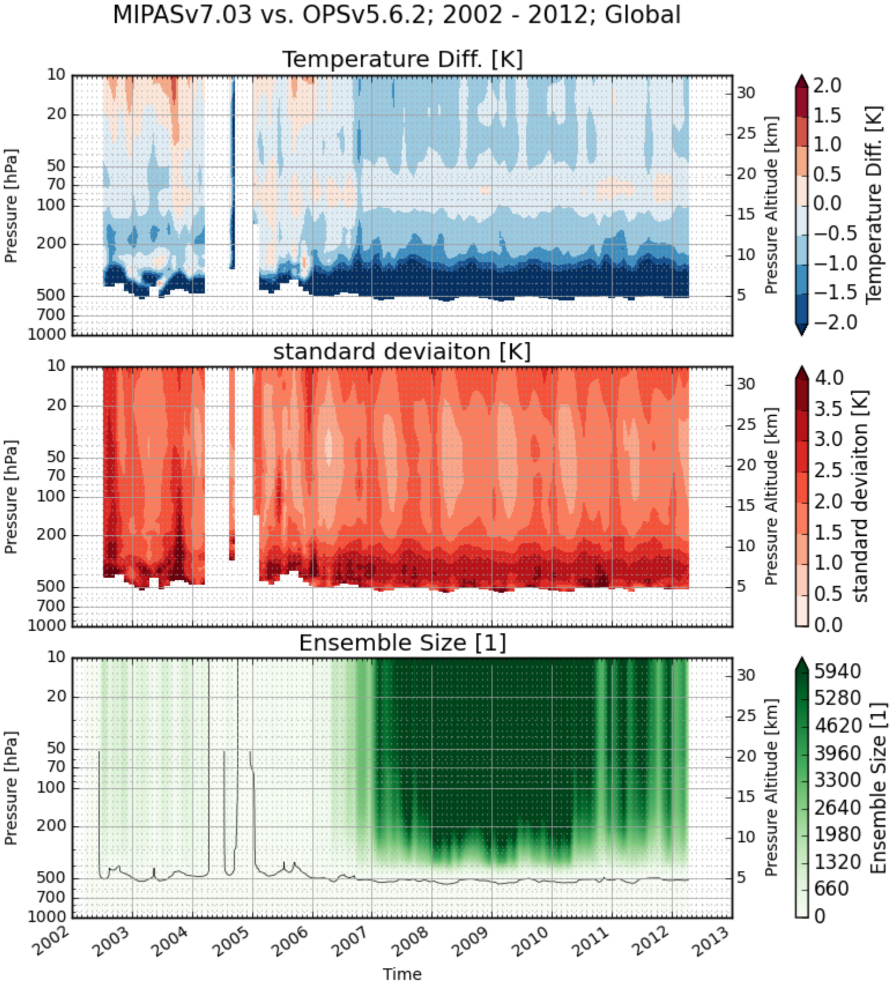

Figure 2.3: Global MIPAS versus RO temperature validation results and the number of collocated profile pairs as a function of time from 2002 to 2012.

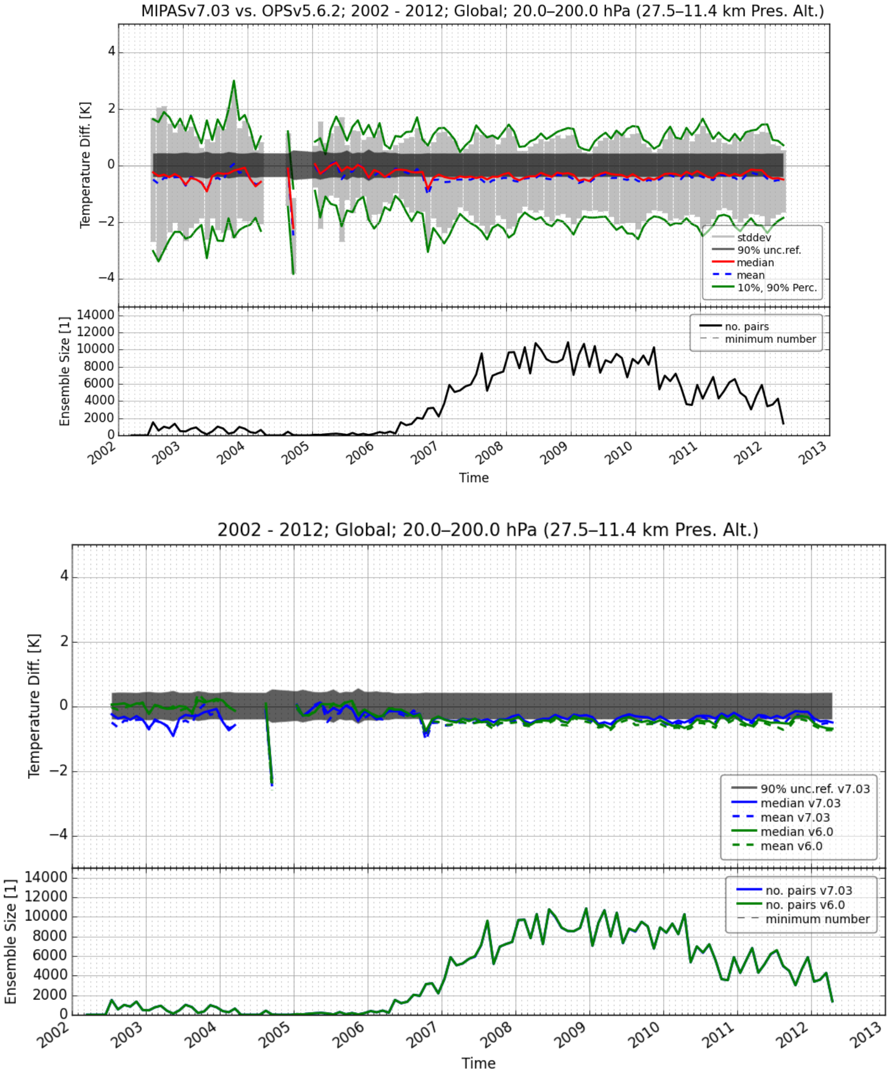

Figure 2.4: Global MIPAS versus RO temperature validation results for the UTLS core region (200 hPa to 20 hPa) and the number of collocated profile pairs as a function of time. Top panel: detailed statistical measures for MIPASv7.03; mean differences: blue; median: red; standard deviation: light-gray bars; 10 % and 90 % Percentiles: green; 90 % RO uncertainty range: dark gray. Bottom panel: Comparison of MIPASv7.03 vs. OPSv5.6 (blue) and MIPASv6.0 (green) vs. OPSv5.6 from 2002 to 2012; mean differences: dashed; median differences: solid.

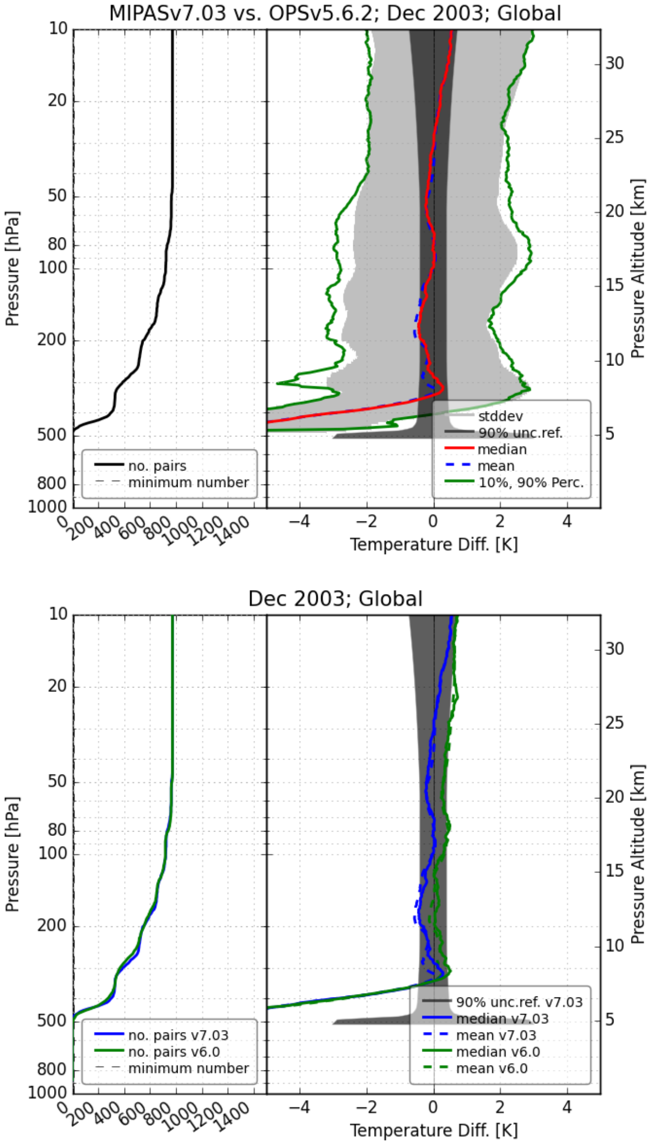

Figure 2.5: Global MIPAS versus RO temperature validation results from 1000 hPa to 10 hPa and the number of collocated profiles for December 2003. Top panel: detailed statistical measures for MIPASv7.03; mean differences: blue; median: red; standard deviation: light-gray bars; 10 % and 90 % Percentiles: green; 90 % RO uncertainty range: dark gray. Bottom panel: Comparison of MIPASv7.03 vs. OPSv5.6 (blue) and MIPASv6.0 (green) vs. OPSv5.6; mean differences: dashed; median differences: solid.

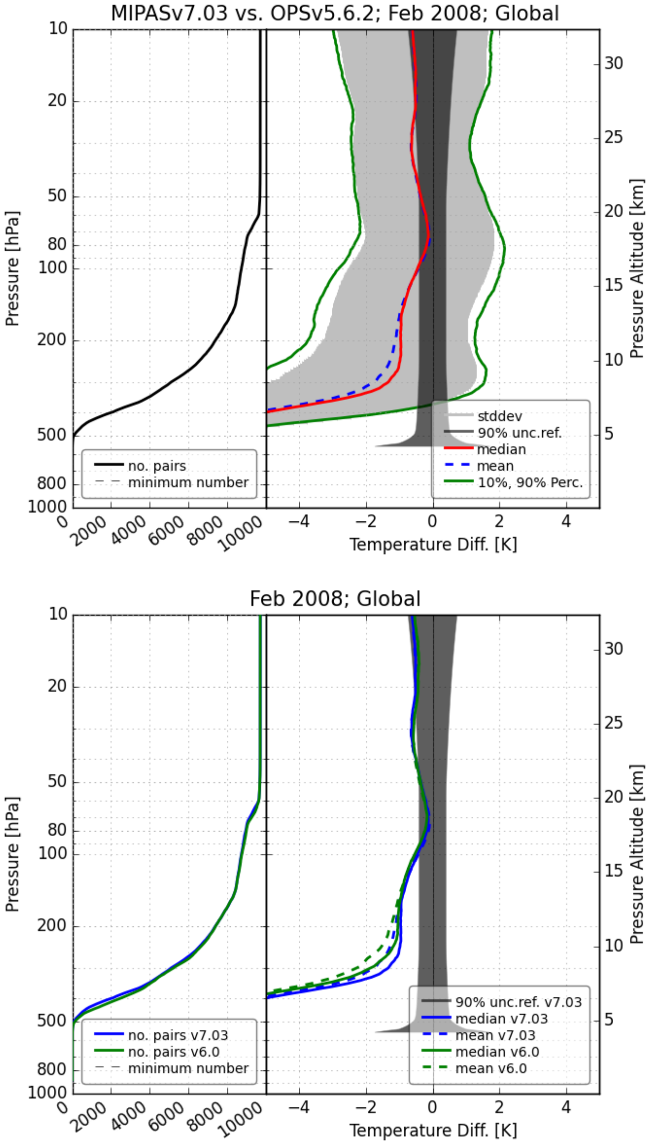

Figure 2.6: Global MIPAS versus RO temperature validation results from 1000 hPa to 10 hPa and the number of collocated profiles for February 2008. Top panel: detailed statistical measures for MIPASv7.03; mean differences: blue; median: red; standard deviation: light-gray bars; 10 % and 90 % Percentiles: green; 90 % RO uncertainty range: dark gray. Bottom panel: Comparison of MIPASv7.03 vs. OPSv5.6 (blue) and MIPASv6.0 (green) vs. OPSv5.6; mean differences: dashed; median differences: solid.

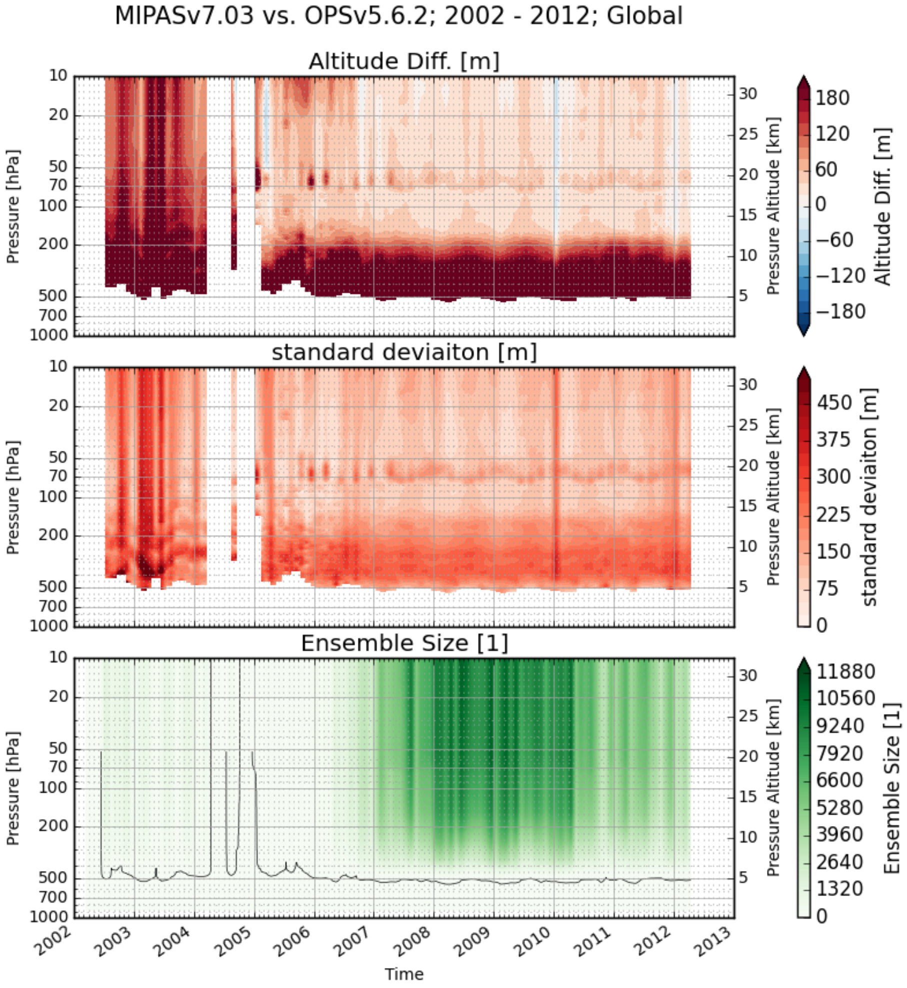

Figure 2.7: Global MIPAS versus RO alititude validation results and the number of collocated profiles as a function of time from 2002 to 2012.

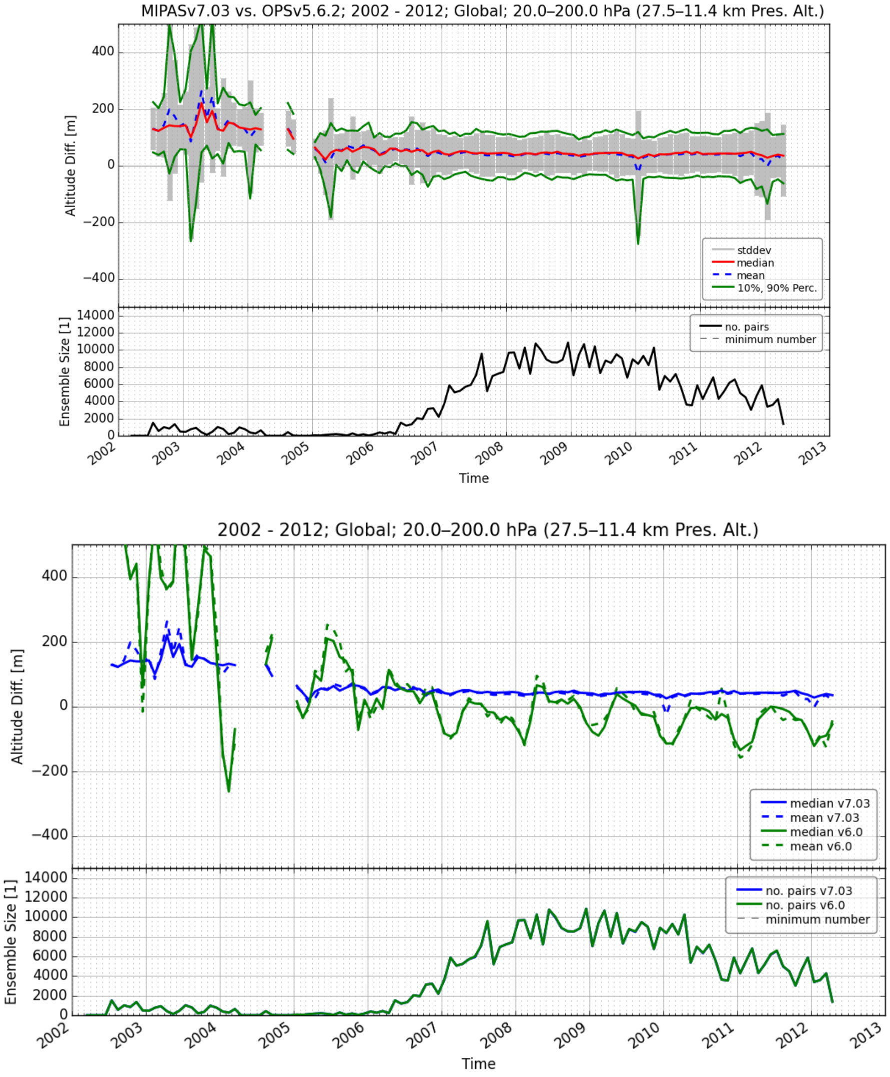

Figure 2.8: Global MIPAS versus RO altitude validation results for the UTLS core region (200 hPa to 20 hPa) and the number of collocated profile pairs as a function of time. Top panel: detailed statistical measures for MIPASv7.03; mean differences: blue; median: red; standard deviation: light-gray bars; 10 % and 90 % Percentiles: green;. Bottom panel: Comparison of MIPASv7.03 vs. OPSv5.6 (blue) and MIPASv6.0 (green) vs. OPSv5.6 from 2002 to 2012; mean differences: dashed; median differences: solid.

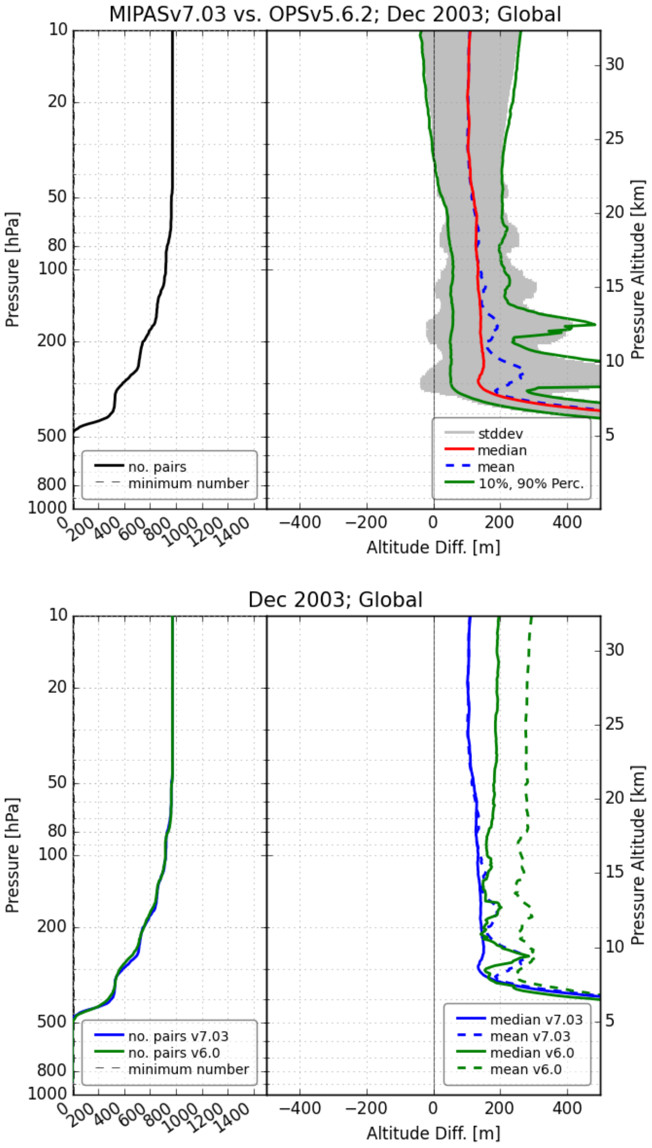

Figure 2.9: Global MIPAS versus RO altitude validation results from 1000 hPa to 10 hPa and the number of collocated profiles for December 2003. Top panel: detailed statistical measures for MIPASv7.03; mean differences: blue; median: red; standard deviation: light-gray bars; 10 % and 90 % Percentiles: green;. Bottom panel: Comparison of MIPASv7.03 vs. OPSv5.6 (blue) and MIPASv6.0 (green) vs. OPSv5.6; mean differences: dashed; median differences: solid.

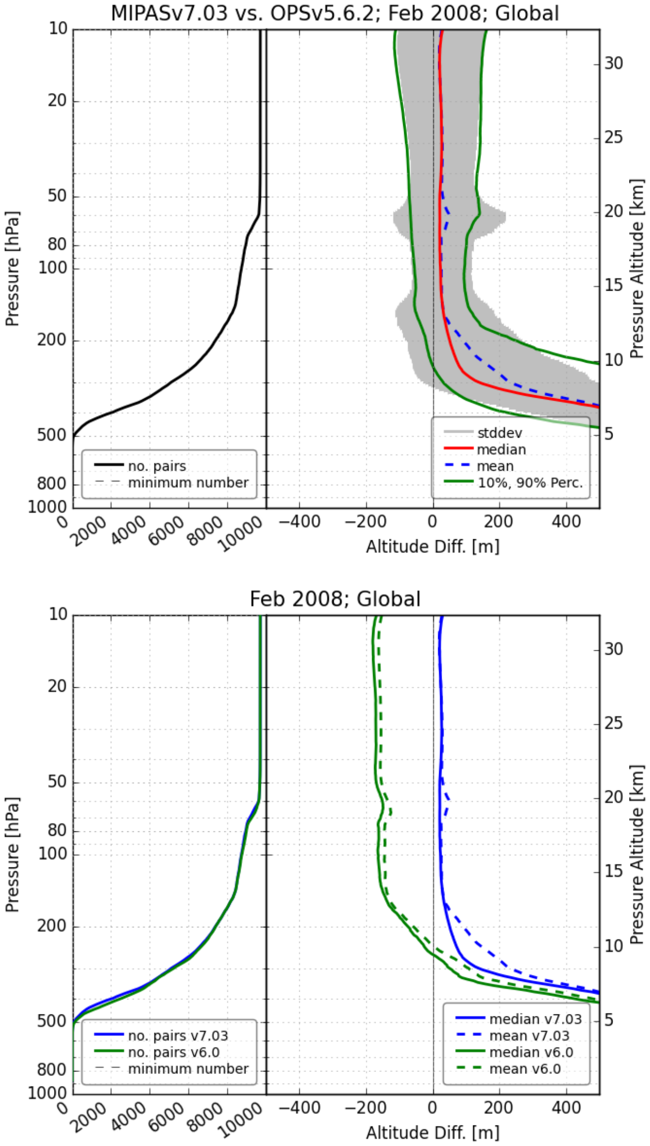

Figure 2.10: Global MIPAS versus RO altitude validation results from 1000 hPa to 10 hPa and the number of collocated profiles for February 2008. Top panel: detailed statistical measures for MIPASv7.03; mean differences: blue; median: red; standard deviation: light-gray bars; 10 % and 90 % Percentiles: green;. Bottom panel: Comparison of MIPASv7.03 vs. OPSv5.6 (blue) and MIPASv6.0 (green) vs. OPSv5.6; mean differences: dashed; median differences: solid.

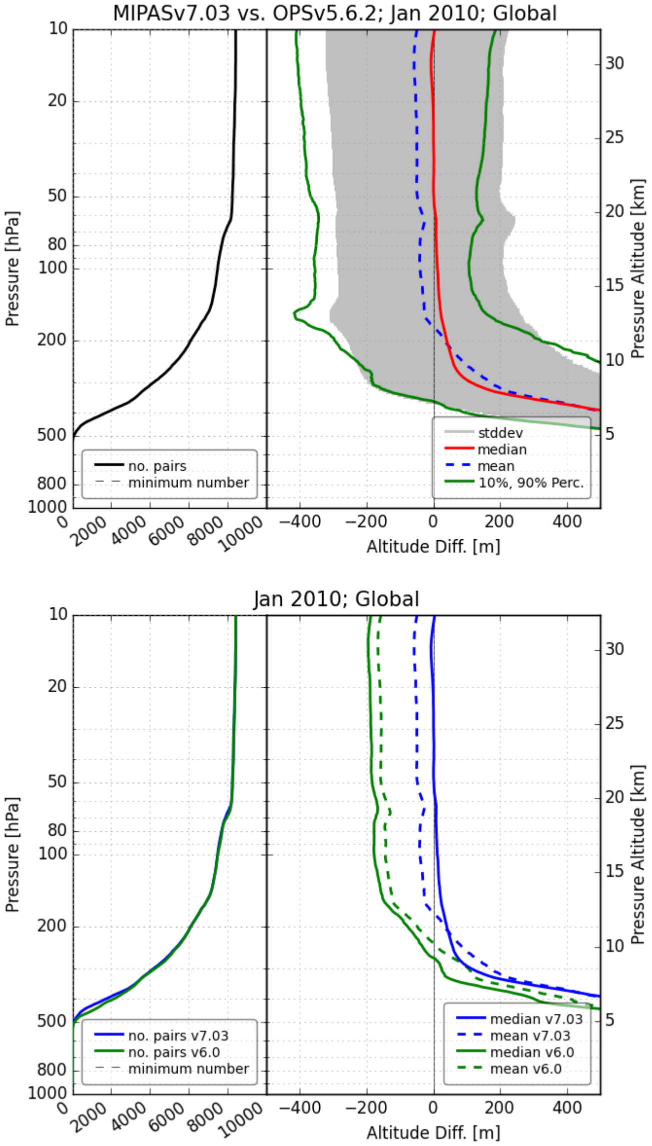

Figure 2.11: Global MIPAS versus RO altitude validation results from 1000 hPa to 10 hPa and the number of collocated profiles for January 2010. Top panel: detailed statistical measures for MIPASv7.03; mean differences: blue; median: red; standard deviation: light-gray bars; 10 % and 90 % Percentiles: green;. Bottom panel: Comparison of MIPASv7.03 vs. OPSv5.6 (blue) and MIPASv6.0 (green) vs. OPSv5.6; mean differences: dashed; median differences: solid.

2.2 GOMOS Validation by RO for the Period 2002 to 2012

2.2.1 Input Data Flows and GOMOS-RO Collocations 2002 to 2012

The candidate data input flow consisted of the GOMOSv6.01 reprocessing dataset 2002 to 2012. The reference input data flow of OPSv5.6 (2002 to 2012 and beyond) was obtained from the satellites CHAMP, COSMIC (major fraction), C/NOFS, SAC-C, and GRACE. 300 km/3 h space-time distance was used as collocation criterion. GOMOS temperature and density were validated against RO temperature and density for the collocated ensemble of profiles, on a global scale. The GOMOS profiles were from the so-called HRTP[19] products (see links to further information on GOMOS products at validate.globclim.org or at esa's gomos website). The profiles were interpolated to an equidistant altitude grid with 350 levels between 0.1 km to 35 km (for details cf.Subsection 3.1.4). A vertical smoothing was performed on both measurements as explained in Subsection 3.1.4 using an effective resolution of 3 km.

Figure 2.12 shows, on a monthly scale over the time period studied, the number of profiles from the candidate (GOMOS) and reference (RO) data sources as well as for the single RO satellites/ satellite constellations, together with the number of collocated profiles (L.H.S. ordinate) found in each month. In addition, Figure 2.13 shows the representative collocation distributions for July 2005 and July 2008. The color bar indicates the space-time distance between the validated and the reference profile. The time distance is converted to a spatial distance by applying a conversion factor of 100 km per hour. A more detailed view on such collocation distributions for the whole ENVISAT period can be found on the Wegener Center's MMValRO validation website `http://validate.globclim.org`.

The GOMOS data stream, retrieved from ESA's D-PAC[20], features a fairly variable number of about 2 000 to near 15 000 profiles per month from September 2002 until April 2012, except in the period between February 2005 and June 2005 where no or almost no data were available. Generally after July 2005 the number is not higher than about 10 000 profiles per month, while over 2003 and 2004 it is highest in the period, typically within 10 000 to 15 000 profiles per month. The RO data stream is small, below 5000 profiles per months, before the "COSMIC data era" starts as of mid 2006, from which on 40 000 to 70 000 RO profiles are available per month.

Reflecting these input data streams, the number of collocated profiles is smaller up to June 2006, from about 100 to 800 collocations per month, and higher from July 2006 onwards, typically more than 1000 collocations per month (exceptions are some individual months with nearly no GOMOS data – e.g. the period between February to October 2009).

---

[19] High Resolution Temperature Profile

[20] German Processing and Archiving Centre

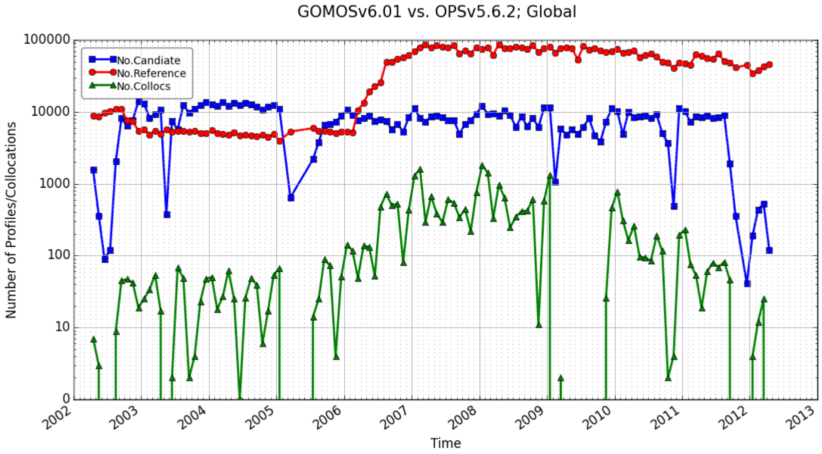

Figure 2.12: Overview on the number of events of GOMOS and RO data, as well as on the collocated profiles, over 2002 to 2012.

2.2.2 GOMOS Temperature Validation by RO

Figure 2.14 and Figure 2.15 shows overall results for GOMOS temperature validation. It has to be noted here once more that below 16 km the RO physical temperature is correlated with the ECMWF short term forecast field because of the 1D-Var approach.

As a reference information on how the temperature errors of the RO data behave see the respective notes in Subsection 2.1.2; we just recall here the essential point that they are generally <0.3 K within 8 km to 25 km and stay <0.8 K up to 35 km and down to 5 km, respectively. As for the discussion of the MIPAS results in the previous section see the MMValRO validation website `http://validate.globclim.org` for detailed results for different altitude layers (relevant for GOMOS are the 15 km to 20 km up to 30 km to 35 km layers) and individual months.

It is to be noted—in the auxiliary panel of Figure 2.15, which shows the number of collocated profiles that actually entered the validation after passing the GOMOS quality control—that the collocated ensemble size for the validation is fairly small (often less than 10 %) compared to the basic number of collocated profiles that fulfill the space-time distance criterion: The reason is that the quite selective GOMOS quality control (summarized in Subsection 3.1.4) eliminates a significant number of profiles that would further degrade the performance compared to the validation results discussed here. The quality control for GOMOS is based on experience from the GOMOS user community on what influences the quality of those data (Viktoria Sofieva, FMI Helsinki, personal communications, 2013).

Generally speaking, the GOMOS temperature bias against RO is within about 0 K to 1.5 K in the GOMOS core range from 20 km to 30 km throughout all years with the exception of

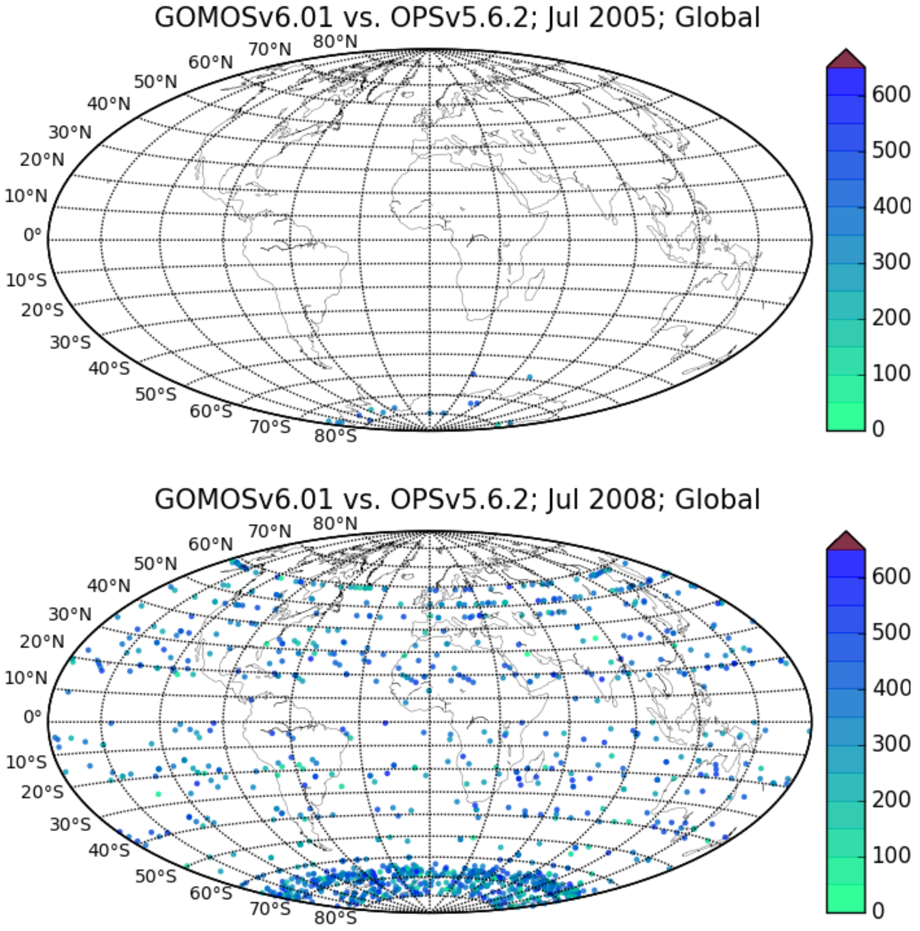

GOMOSv6.01 vs. OPSv5.6.2; Jul 2005; Global

GOMOSv6.01 vs. OPSv5.6.2; Jul 2008; Global

Figure 2.13: Collocation distribution for GOMOS, months July 2005 and 2008.

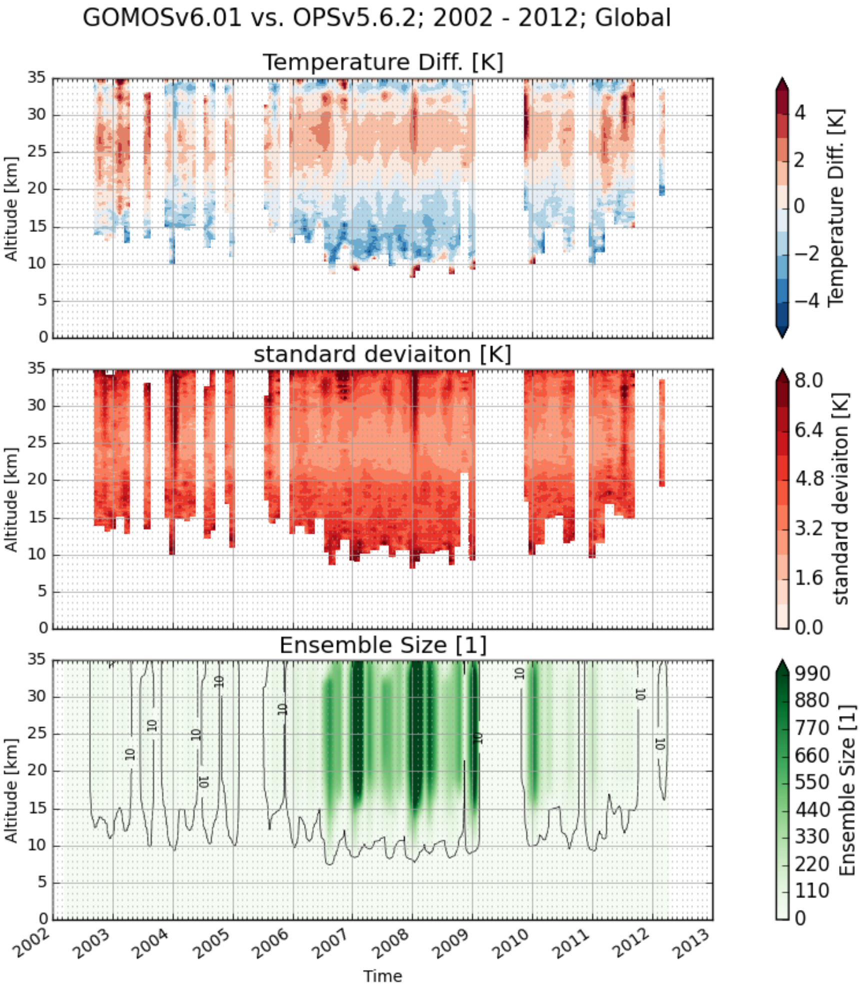

Figure 2.14: Global GOMOS versus RO temperature validation results and the number of collocated profiles as a function of time from 2002 to 2012.

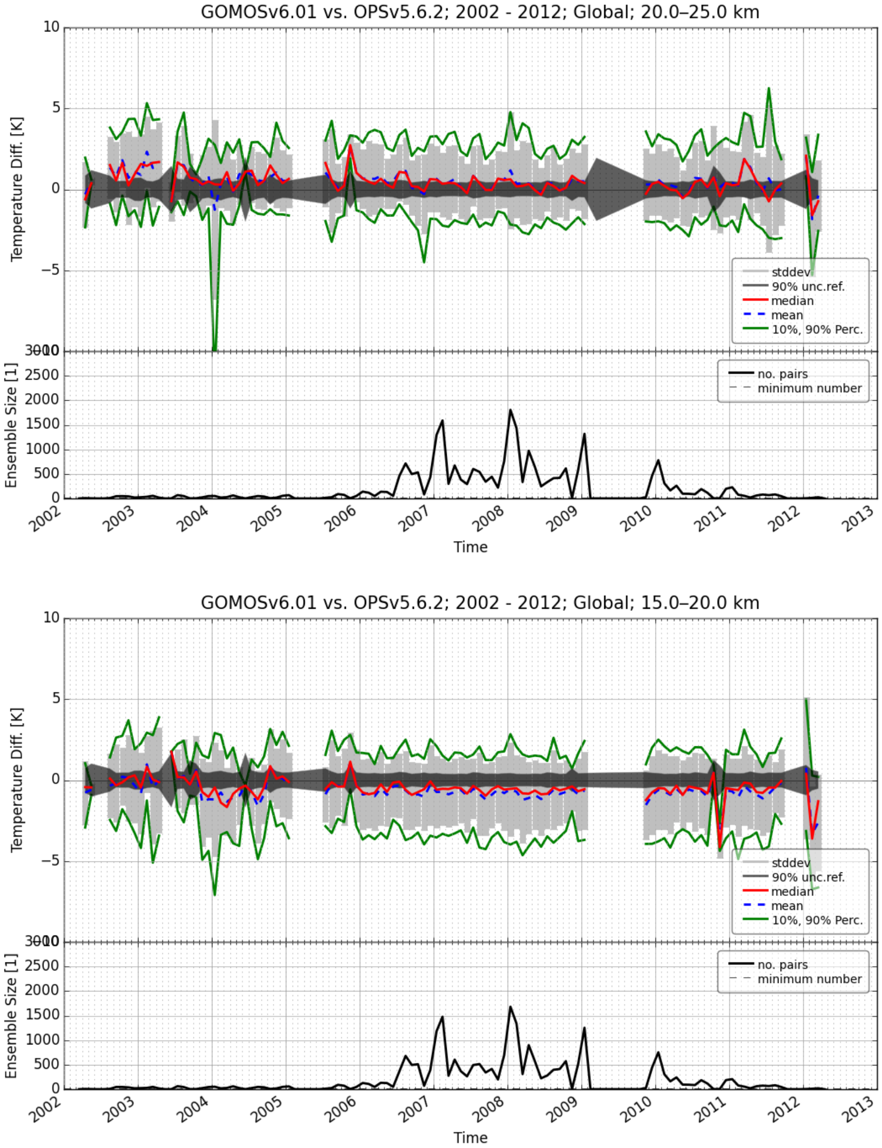

Figure 2.15: Global GOMOS versus RO temperature validation from 20 km to 25 km (top panel) and 15 km to 20 km (bottom panel) and the number of collocated profiles as a function of time on a monthly scale. Mean systematic differences: blue; median differences: red; standard deviation: light-gray bars; 10 % and 90 % Percentiles: green; 90 % RO uncertainty range: dark gray.

a few individual months exceeding this (February to August 2003, with a stronger positive bias, or January 2004, exhibiting a stronger negative bias). Compared to the MIPAS–RO comparison, the biases are considerably larger. Additionally, the RMSE[21] is larger, too.

But the comparison to the validation results of the old dataset the quality of the GOMOS data has increased strongly (cf. differences between the upper and lower panel in Figure 2.15).

From 20 km to 30 km over the lower stratosphere the quality of the GOMOS temperature is most valuable compared to regions below and above, consistent with the GOMOS Handbook quoting relatively best quality for this region (see links to detailed GOMOS-related information via `http://validate.globclim.org`). The general agreement with RO has increased significantly.

Inspecting the GOMOS HRTP time record more precisely throughout different altitude layers we can see that it exhibits negative bias between about -0.5 K to -1.5 K in the height layer from about 15 km to 20 km (cf. lower panel of Figure 2.15), up to a positive bias between about 0.5 K to 2 K in the height layer from 25 km to 30 km with an intermediate bias between about 0 K to 1 K in the height layer from 20 km to 25 km (cf. upper panel of Figure 2.15). In the 30 km to 35 km layer the bias stays most time within the estimated RO 90 % uncertainty range.

Looking finally beyond the overall picture towards specific conclusions, the following stand out: The quality of the GOMOSv6.01 HRTP temperature product has increased significantly compared to the previous mixed product (GOMOSv4-6, not shown here) in both the general bias structure and the RMSE throughout all layers and times; the best region is the relatively confined altitude range from 20 km to 30 km and it is confirmed here that the reprocessing of the GOMOS data was really a valuable and needed activity.

Table 2.3 shows the mean temperature bias and the mean standard deviation (in Kelvin) of GOMOSv6.01 versus OPSv5.6 for different regions (explanation of the abbreviations cf. description of Table 2.1) for the full ENVISAT period. We can clearly see that there is a very strong reduction in the standard deviation (at least by a factor of 3) in standard deviation. The bias was also strongly reduced in the layers between 15 km to 20 km and 30 km to 35 km. In the other layers the structure of the bias is now consistent throughout all geographic regions within the layers.

As for MIPAS, in order to enable a more detailed look at the behavior of individual months, also separate plots as a function of altitude are available per month, showing the GOMOS validation in an altitude-resolved manner. As examples, Figure 2.16 and Figure 2.17 show this detailed look for two months with typical altitude-dependent GOMOS HRTP temperature error behavior (December 2005, Figure 2.16, and June 2008, Figure 2.17). The same type of plots is available for all months with a sufficient number of collocated profiles at `http://validate.globclim.org`.

---

[21] Root-Mean-Square Error

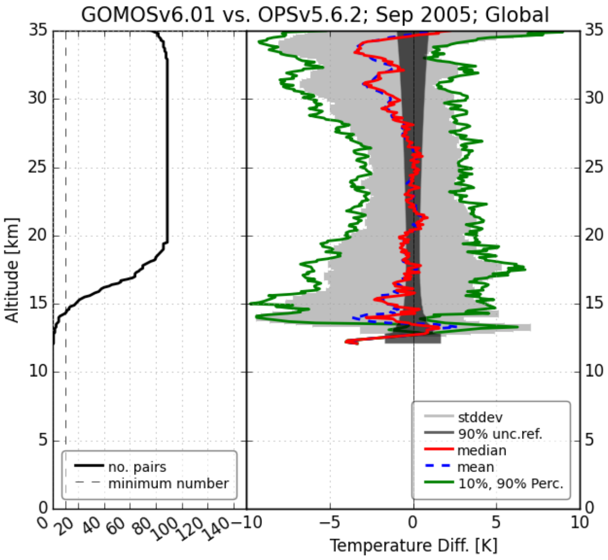

Figure 2.16: Global GOMOS versus OPSv5.6 temperature validation results from 0 km to 35 km; actual data down to about 18 km/13 km) and the number of collocated profiles for September 2005. Mean systematic differences: blue; median differences: red; standard deviation: light-gray bars; 10 % and 90 % Percentiles: green; 90 % RO uncertainty range: dark gray.

Table 2.3: Mean temperature bias and mean standard deviation (in Kelvin) of GOMOS vs. OPSv5.6 profiles for different regions. Statistics is calculated for the whole ENVISAT period.

	10–15 km	15–20 km	20–25 km	25–30 km	30–35 km
GLO	−0.85/1.94	−0.64/2.19	0.52/2.30	1.29/2.30	0.12/2.88
NHL	−0.81/1.74	−0.24/2.11	0.72/2.80	1.46/2.80	0.95/3.38
NML	−0.33/1.50	−0.68/2.12	0.25/1.86	1.28/1.86	0.02/2.34
NLL	−1.18/1.52	−1.03/2.12	0.51/2.32	1.87/2.32	0.36/2.69
SLL	−0.86/1.67	−0.58/1.90	0.41/1.79	0.92/1.79	−0.71/2.46
SML	−0.17/1.24	−0.55/2.06	0.44/1.79	0.73/1.79	−0.72/2.51
SHL	−0.62/2.00	−0.45/2.06	1.29/2.55	2.04/2.55	1.29/2.42

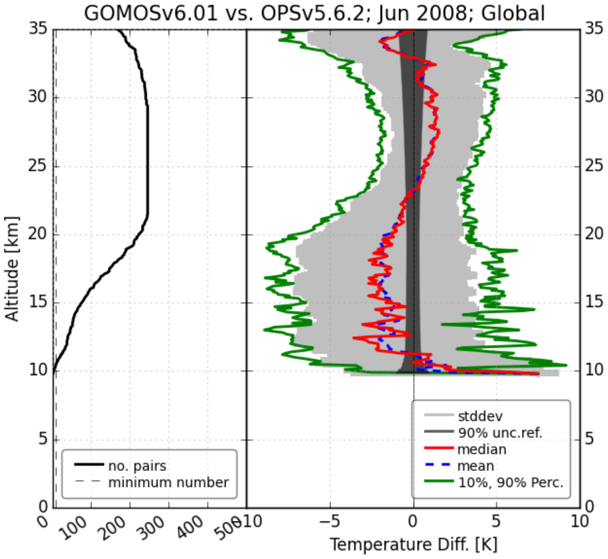

Figure 2.17: Global GOMOS versus OPSv5.6 temperature validation results from 0 km to 35 km; actual data down to about 18 km/13 km) and the number of collocated profiles for June 2008. Mean systematic differences: blue; median differences: red; standard deviation: light-gray bars; 10 % and 90 % Percentiles: green; 90 % RO uncertainty range: dark gray.

Figure 2.16 acts as an example for the validation period with fewer collocations due to the fact that for RO only the CHAMP satellite has delivered data during this time period. It exhibits a quite good bias structure and is almost everywhere within the RO uncertainty bounds between 17 km to 27 km.

Figure 2.17 serves as an example for the validation period with a larger number of collocations. It exhibits the typical nature of deviations of the more and less valuable regions of this GOMOS product. The bias is typically negative up to about 22 km to 23 km and then becomes positive up to about 32 km to 33 km. This type of figures is evidently a good means to more closely explore the individual climatological time periods (e.g., single months) that have spotted special interest.

2.2.3 GOMOS Density Validation by RO

Figure 2.18 and Figure 2.19 show the overall results for GOMOS density validation. It has to be noted here once more that below 16 km the RO physical density is correlated with the ECMWF short term forecast field because of the 1D-Var approach.

As for the temperature results in the previous section see the website `http://validate.globclim.org` for detailed results for different altitude layers (relevant for GOMOS are the 15 km to 20 km to 30 km to 35 km layers) and individual months.

As a reference information on RO, as available from RO literature [SP+11a; SP+11b], we note that the OPSv5.4 monthly-mean RO density data have a systematic error of <0.2 % within 8 km and 25 km, increasing to <0.5 % up to 35 km and down to 5 km, respectively. The OPSv5.6 has similar error characteristics in the UTLS, as comparison against OPSv5.4 shows, so the same error estimates apply and were built into the visualized 90 % RO uncertainty ranges. Also RO data are long-term stable, i.e., based on literature information ([SP+11b; Ste+13], and references therein) their systematic density error over 2002 to 2011 is expected to change by <0.2 % per decade over this period. The validation can be interpreted with this error information on RO in mind.

Generally GOMOS density is biased against RO by about −1.5 % to −2 % (except November 2009: −5 %; but here the number of collocation pairs is very low) in the new dataset compared to about 5 % with variations mostly within 2 % and 8 %, throughout all years. This first of all confirms all GOMOS data are overall in the right ballpark, there is no illegitimate, i.e., truly non-physical outlier in terms of monthly GOMOS climatologies.

Assessing the validation in more quantitative detail, the bias of around −1.5 % to −2 %, that also applies in the altitude range of best quality within 20 km to 30 km (cf. previous subsection on GOMOS temperature validation), is likely some type of “calibration offset” of these GOMOS data (such as altitude mis-location seen above also for MIPAS pressure data). This level of bias is somewhat too large for many practical atmospheric applications. There is also a trend tendency visible over the time period with two resets – one at the beginning of 2006 and the other after the large validation gap in 2009, with e.g. biases of

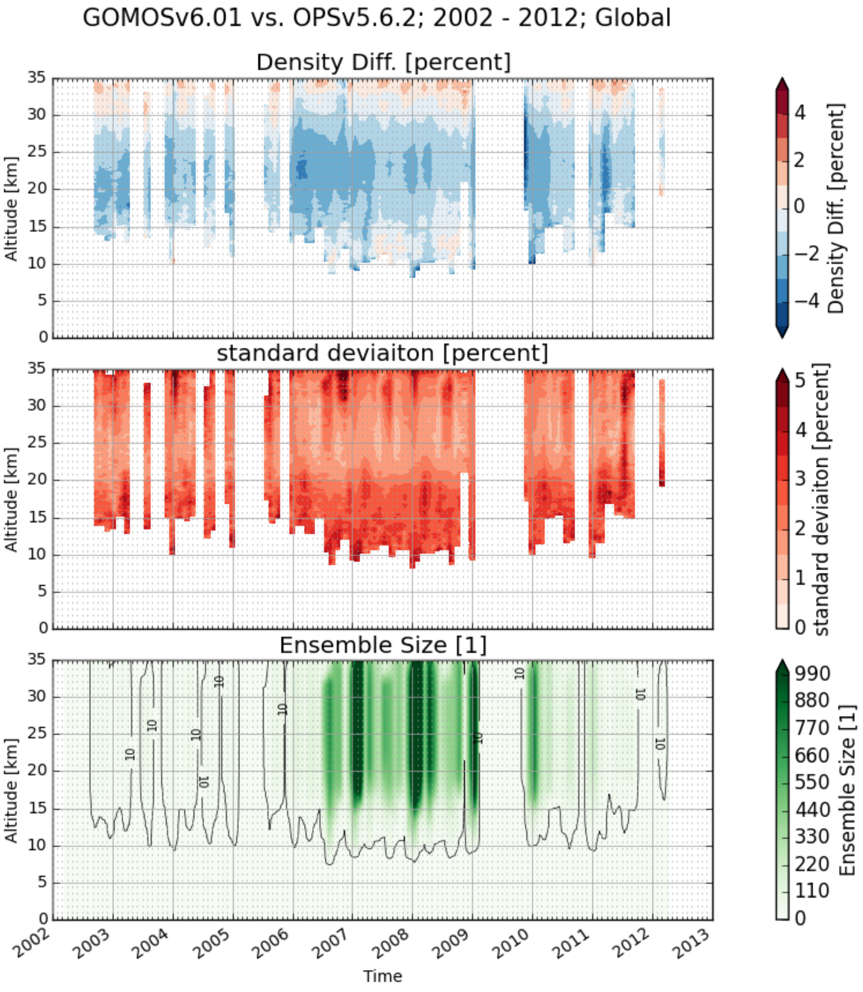

Figure 2.18: Global GOMOS versus RO density validation results and the number of collocated profiles as a function of time from 2002 to 2012.

Table 2.4: Mean density bias and mean standard deviation (in percent) of GOMOS vs. OPSv5.6 profiles for different regions. Statistics is calculated for the whole envisat period.

	20–30 km	15–20 km	20–25 km	25–30 km	30–35 km
GLO	−0.49/1.29	−1.25/1.70	−2.03/1.48	−1.44/1.48	−0.05/1.71
NHL	−0.35/1.13	−1.77/1.31	−2.09/1.42	−1.58/1.42	−0.45/2.08
NML	−0.38/1.06	−1.18/1.57	−2.05/1.00	−1.66/1.00	−0.21/1.33
NLL	−0.49/1.12	−1.35/1.76	−2.52/1.41	−2.00/1.41	−0.17/1.41
SLL	−0.39/1.18	−1.13/1.43	−1.89/1.16	−1.14/1.16	0.41/1.42
SML	−0.25/0.79	−1.00/1.51	−1.60/1.17	−0.89/1.17	0.39/1.60
SHL	−0.28/1.20	−1.33/1.38	−1.97/2.21	−1.18/2.21	−0.11/1.87

about −2 % at the beginning of 2006, and more around −1 % at the end of 2009. Thereby, in the last drift period, starting at the end of 2009 March and April 2011 an exception of lower biases occurs. Within 30 km to 35 km, where temperature biases above have been seen to stay more or less within the estimated RO uncertainty bounds, the density bias jumps to the positive side, to settle within a range of about 0.5 % to 1.5 %.

Looking finally in Figure 2.19 beyond the overall picture towards specific conclusions, the following stand out: The quality of the GOMOS density product is comparable to the quality of the temperature product having a varying bias between −2 % to 0 % in the range of 15 km to 20 km and between −2.5 % to −1 % in the GOMOS core altitude range of 20 km to 30 km. This negative bias could be an indication for an altitude registration issue for GOMOS. Also these density validation results in comparison to the previous ones have confirmed that the reprocessing of the GOMOS data was really a valuable and needed activity.

Table 2.4 shows the mean density bias and standard deviation (in percent) of GOMOSv6.01 versus OPSv5.6 for different regions (explanation of the abbreviations cf. description of Table 2.1).

As for temperature, in order to enable a more detailed look at individual months, separate plots as a function of altitude are available per month at `http://validate.globclim.org`, showing the GOMOS validation in an altitude-resolved manner. As examples, Figure 2.20 shows the validation results for the period with fewer collocations due to the fact that for RO only the CHAMP satellite has delivered data during this time period. Figure 2.21 show this detailed look for the validation period with a larger number of collocations.

Inspecting Figure 2.20 and Figure 2.21 exhibits the typical nature of deviations of this GOMOS data product and this type of plots is evidently a good means and starting point to more closely analyze elementary climatological time periods (here individual months) that

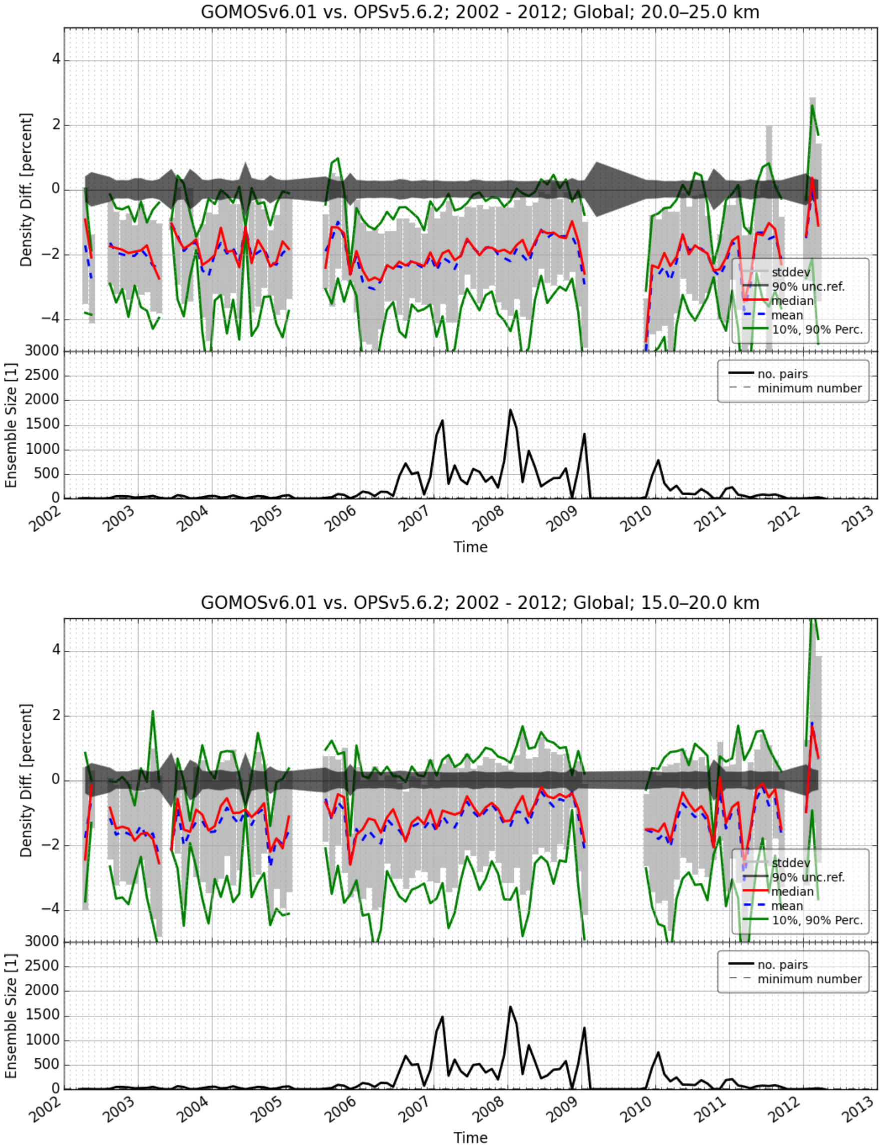

Figure 2.19: Global GOMOS versus RO density validation from 20 km to 25 km (top panel) and 15 km to 20 km (bottom panel) and the number of collocated profiles as a function of time on a monthly scale. Mean systematic differences: blue; median differences: red; standard deviation: light-gray bars; 10 % and 90 % Percentiles: green; 90 % RO uncertainty range: dark gray.

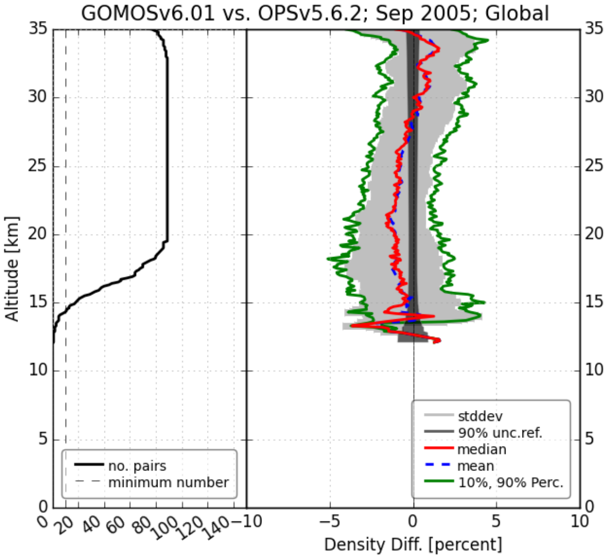

Figure 2.20: Global GOMOS versus OPSv5.6 density validation results from 0 km to 35 km; actual data down to about 18 km/13 km) and the number of collocated profiles for September 2005. Mean systematic differences: blue; median differences: red; standard deviation: light-gray bars; 10 % and 90 % Percentiles: green; 90 % RO uncertainty range: dark gray.

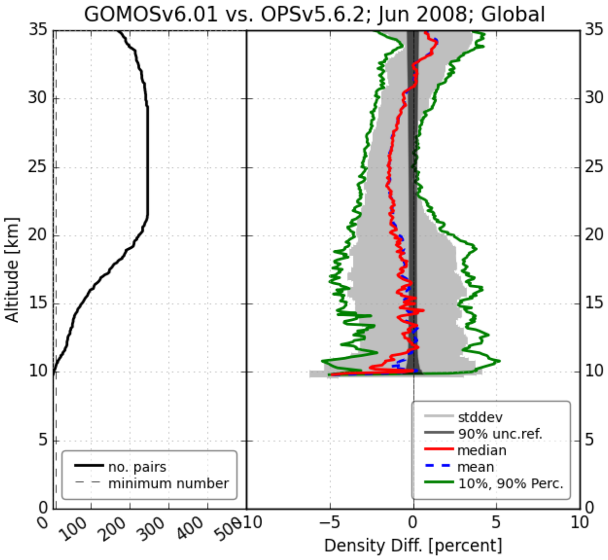

Figure 2.21: Global GOMOS versus OPSv5.6 density validation results from 0 km to 35 km; actual data down to about 18 km/13 km) and the number of collocated profiles for June 2008. Mean systematic differences: blue; median differences: red; standard deviation: light-gray bars; 10 % and 90 % Percentiles: green; 90 % RO uncertainty range: dark gray.

have spotted special interest.

2.3 RO vs. RAOB Comparison for the Period 2002 to 2016

2.3.1 Input Data Flows and RAOB-RO Collocations 2002 to 2016

The reference data input flow consisted on the one hand of the Vaisala RS 80/90/92/41 radiosonde data (RAOB observations) from the ECMWF reanalysis archive from 2002 to 2016 and on the other hand of the GRUAN[22] dataset obtained from the GRUAN lead center at DWD[23]. The candidate (RO) input data flow of OPSv5.6 (2002 to 2016) was obtained from the satellites CHAMP, COSMIC (major fraction), and GRACE. 300 km/3 h space-time distance was used as collocation criterion. It turned out that this criteria is too relaxed for specific humidity as discussed at the end of the humidity section (cf. Subsection 2.3.3). RO temperature and specific humidity were compared with RAOB temperature and specific humidity for the collocated ensemble of profiles, on a global scale. In addition, RO temperature and specific humidity measurements were also compared with measurements from GRUAN stations. The profiles were interpolated to an equidistant log-pressure grid with 350 levels between 1000 hPa to 5 hPa (for details cf.Subsection 3.1.4). A vertical smoothing was performed on both measurements as explained in Subsection 3.1.4 using an effective resolution of 1 km.

Figure 2.22 shows, on a monthly scale over the time period studied, the number of profiles from the candidate (RAOB) and reference (RO) data sources as well as for the single RO satellites/ satellite constellations, together with the number of collocated profiles (L.H.S. ordinate) found in each month. In addition, Figure 2.23 shows the collocation distributions for July 2005 and July 2008. The color bar indicates the space-time distance between the validated and the reference profile. The time distance is converted to a spatial distance by applying a conversion factor of 100 km per hour, reflecting typical stratospheric wind speeds. A more detailed view on such collocation distributions for the whole comparison period can be found on the Wegener Center's MMValRO validation website `http://validate.globclim.org`.

The RAOB data stream, retrieved from the ECMWF reanalysis archive and obtained with support by the University of Vienna (L. Haimberger, personal communications, 2012), features a rather stable number of about 15 000 profiles per month from September 2002 until July 2016. From the geographic distribution plot it can be seen that in the early RAOB years the observations mostly took place over Europe (with some exceptions of French and U. K. oversea areas) and then distributing more and more around the world starting in the year 2006. It has to be mentioned that the RAOB are mostly over land. In addition, the Vaisala RS 80/90/92/41 radiosonde type is not used in countries with large geographic extension like Russia, China, India, or the USA during the whole study period. Their usage in most regions of Africa is also very sparse. Here we chose just the Vaisala RS 80/90/92/41

---

[22] GCOS Reference Upper Air Network

[23] Deutscher Wetterdienst

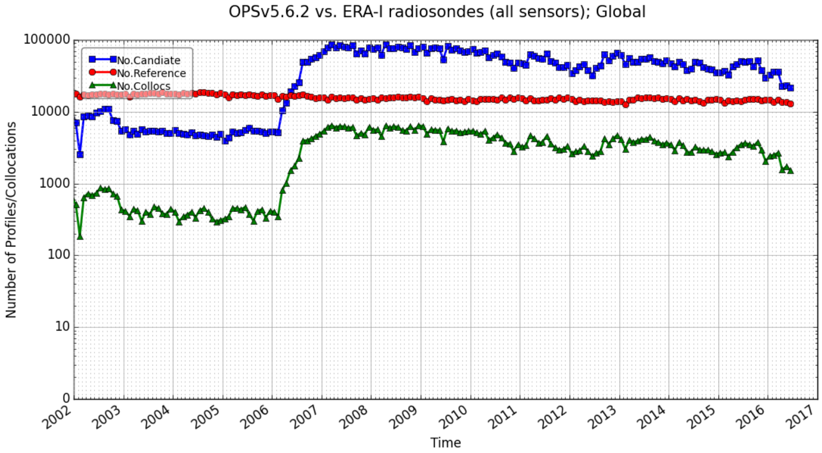

Figure 2.22: Overview on the number of events of RAOB and RO data, as well as on the collocated profiles, from 2002 to 2016.

type for its known credibility to sustainably ensure high-quality radiosonde observations.

As mentioned in Subsection 2.1.1 and Subsection 2.2.1 the RO data stream is small, below 5000 profiles per months, before the "COSMIC data era" starts as of mid 2006, from which on 40 000 to 70 000 RO profiles are available per month (cf. Table 3.4).

Reflecting these input data streams, the number of collocated profiles is small up to the beginning of 2006, from about 200 to 300 collocations per month, starting to increase slightly at the beginning of 2006, followed by a strong increase at the beginning of the COSMIC RO era, where the number of collocations reaches a level of about 7000 profile pairs per month which then gradually decrease to a number of about 3000 profile pairs at the beginning of 2016.

2.3.2 RO vs. RAOB Temperature Comparison

Figure 2.24 and Figure 2.25 show overall results for RAOB temperature validation. It has to be noted here once more that below 16 km the RO physical temperature is correlated with the ECMWF short term forecast field because of the 1D-Var approach.

As a reference information on how the temperature errors of the RO data behave see the respective notes in Subsection 2.1.2; we just recall here the essential point that they are generally <0.3 K within 8 km to 25 km and stay <0.8 K up to 35 km and down to 5 km, respectively. As for the discussion of the MIPAS results in one of the previous sections see the MMValRO validation website `http://validate.globclim.org` for detailed results for different altitude layers (relevant for RAOB temperature are the 500 hPa to 200 hPa up to 10 hPa to 20 hPa layers) and individual months.

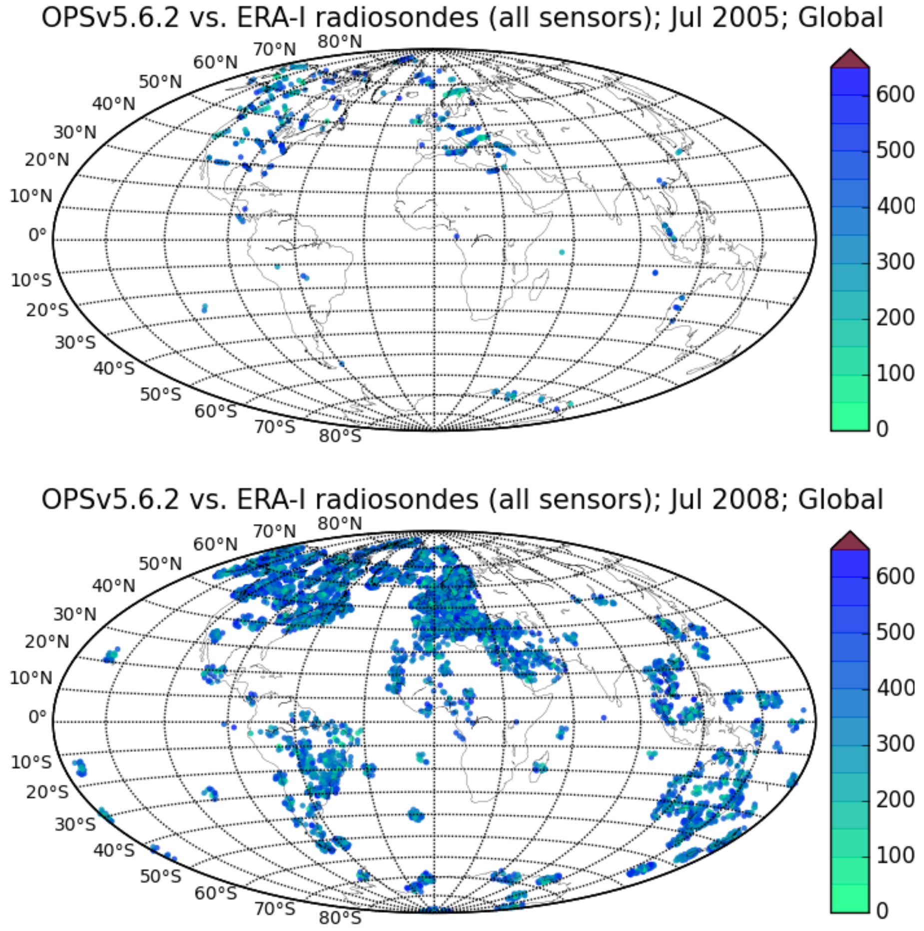

Figure 2.23: Collocation distribution for RAOB, months July 2005 and 2008.

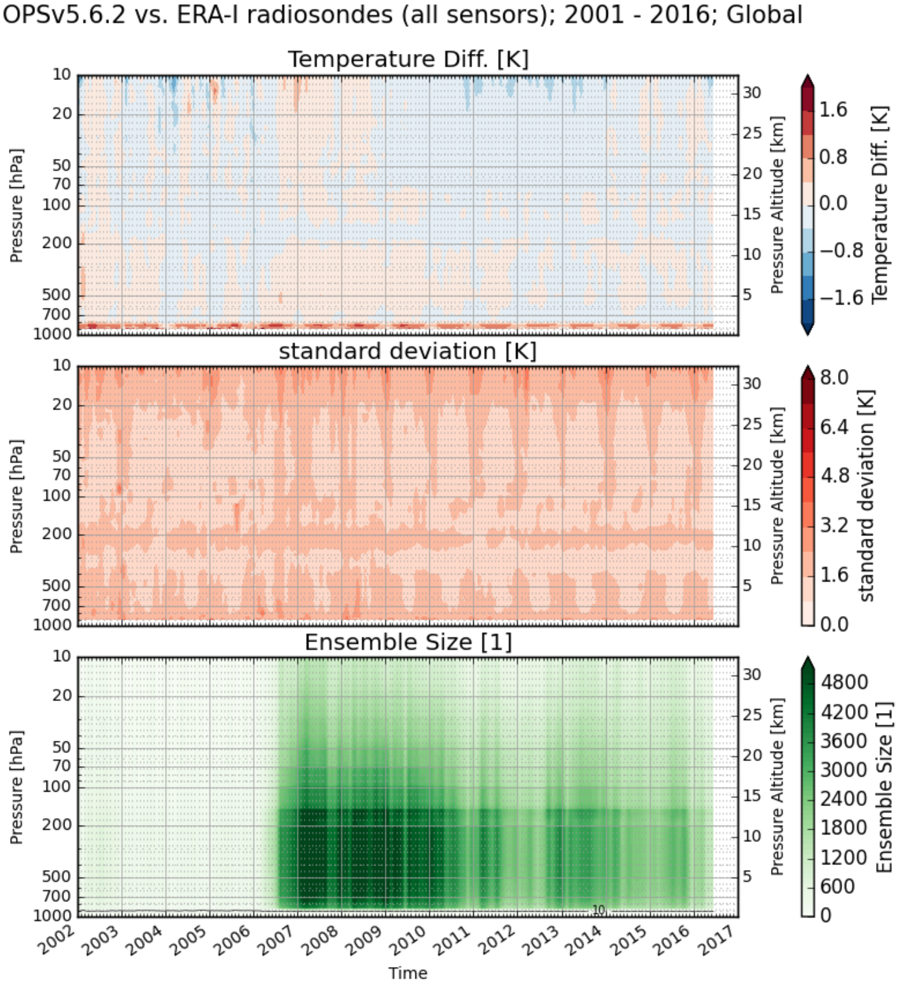

Figure 2.24: Global RAOB versus RO temperature validation results from 1000 hPa to 10 hPa and the number of collocated profiles as a function of time from 2002 to 2012.

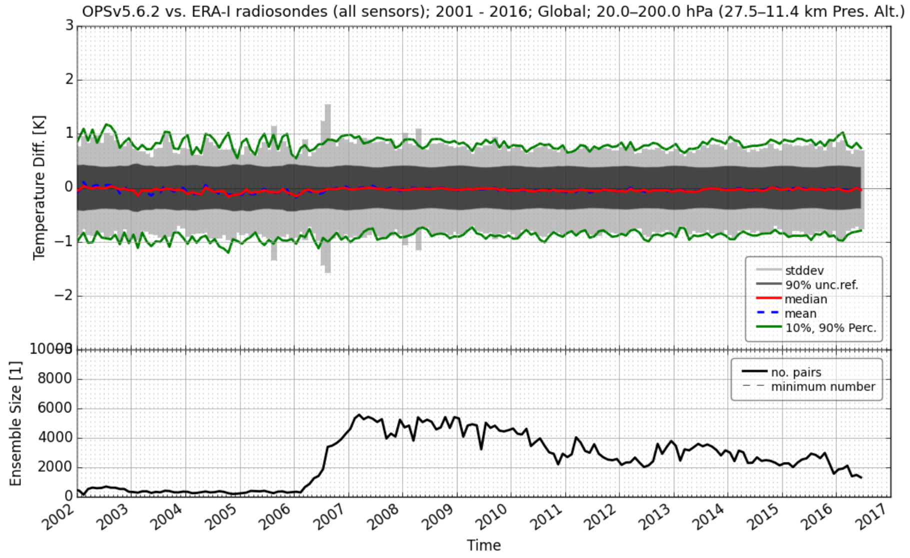

Figure 2.25: Global RAOB versus RO temperature validation results of the UTLS core region (200 hPa to 20 hPa) and the number of collocated profiles as a function of time from 2002 to 2012. Mean systematic differences: blue; median differences: red; standard deviation: light-gray bars; 10 % and 90 % Percentiles: green; 90 % RO uncertainty range: dark gray.

Figure 2.24 shows that we have a decrease in the number of collocations with altitude starting at about 50 hPa (about 20 km pressure altitude) which results from the different heights of the RAOB measurements. This results in an increase of the standard deviations at these altitudes. The spots of rather high standard deviation result from a insufficient quality control of the rather new radiosonde dataset which apart from radiosonde type RS90 and RS92 now includes also data from sondes of the type RS80 and RS41. This features can also be seen in Figure 2.25. Both figures clearly show that the two datasets are in very good agreement.

Looking at the mean (top panel of Figure 2.24) we find very small positive systematic difference of RO against the RAOB data up to about 200 hPa. In the tropopause region the systematic difference tends to be negative and becomes positve again beyond the tropopause, up to about 70 hPa. In the region higher than 70 hPa the systematic difference changes with time. From mid 2006 to end of 2008 it is positive then becomes negative until end of 2014 and returns to a more positive systematic difference afterwards.

Also the mix of Vaisala RS 80/90/92/41 radiosonde types changes over time (cf. Figure 2.26), and at the same time also their overall number changes; also this may contribute

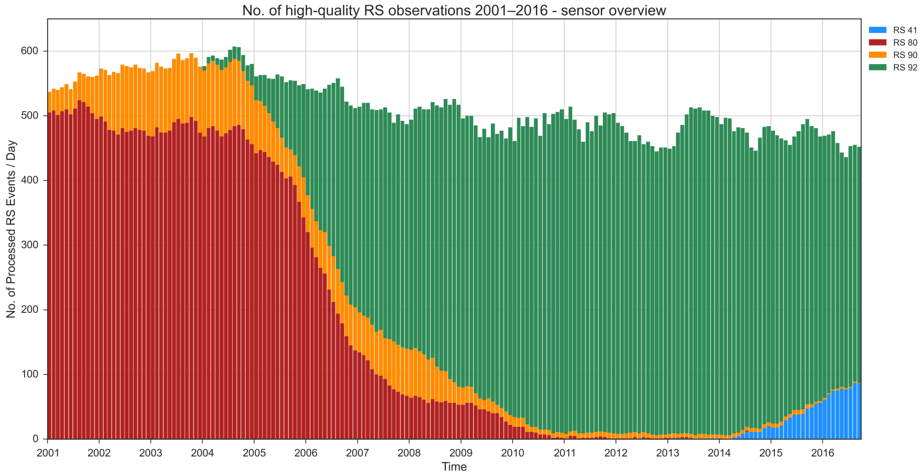

Figure 2.26: Number of high quality RAOB measurements separated into different radiosonde types (Vaisala RS80, RS90, RS92, RS41)on a daily basis from 2001 to 2016.

to some small long-term drifts in the average RAOB temperature estimates.

Generally speaking the RO versus RAOB comparison shows that the RAOB measurements are well within the RO uncertainty bounds over the whole study period especially in the RO core region. Figure 2.25) shows that ROis almost unbiased with keeping a tendency for a slight negative systematic difference against RAOB until mid 2006.

In order to enable a more detailed look at the behavior of individual months beyond inspecting the altitude layers over time, the separate plots as a function of altitude that are available per month are useful. They show the RAOB validation in an altitude-resolved manner. As examples Figure 2.27 and Figure 2.28 show this detailed look for a "CHAMP only" month (May 2003; Figure 2.27) and a "CHAMP/COSMIC" month (July 2007; Figure 2.28); the same type of plots is available for all months on the webpage `http://validate.globclim.org`.

Compared to Figure 2.28, Figure 2.27 has fewer collocations and hence a less smooth statistics. Figure 2.27 exhibits a transition to a negative systematic difference at about 200 hPa. The RAOB mean profiles sit, except for small parts of the profile, within the uncertainty bounds of the RO measurements.

Figure 2.28 exhibits a large number of collocations (more than 3000 between about 900 hPa to 70 hPa). It is within the RO uncertainty bounds over the whole profile and shows almost no systematic difference between RAOB and RO over the whole comparision range.

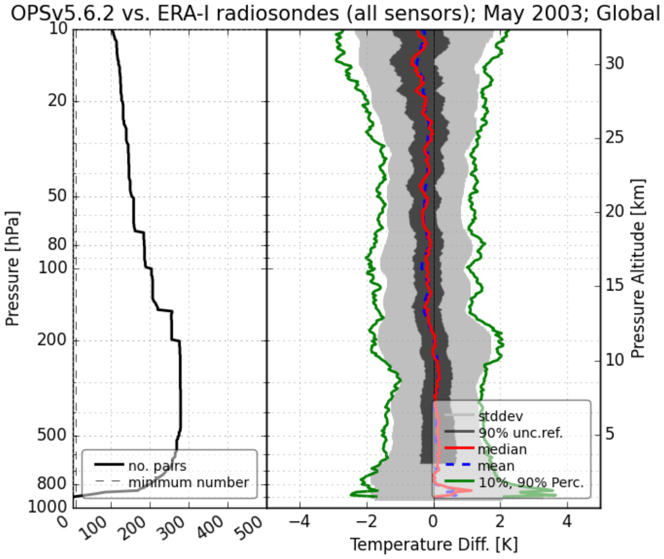

Figure 2.27: Global OPSv5.6 versus RAOB temperature validation results from 1000 hPa to 10 hPa and the number of collocated profiles for May 2003. Mean systematic differences: blue; median differences: red; standard deviation: light-gray bars; 10 % and 90 % Percentiles: green; 90 % RO uncertainty range: dark gray.

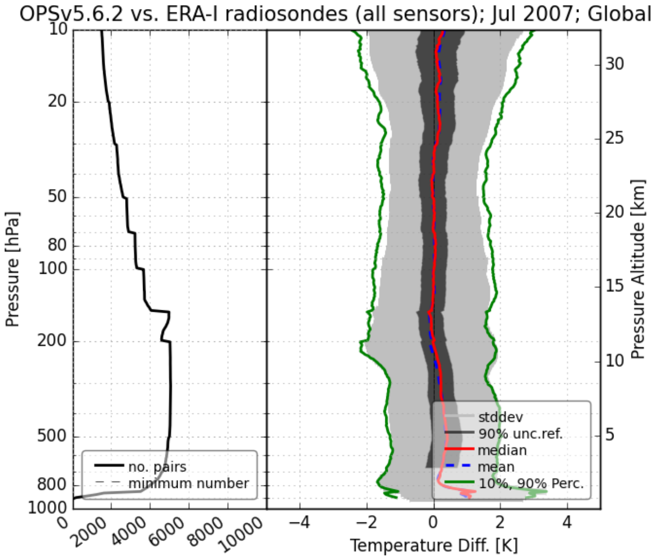

Figure 2.28: Global OPSv5.6 versus RAOB temperature validation results from 1000 hPa to 10 hPa and the number of collocated profiles for July 2007. Mean systematic differences: blue; median differences: red; standard deviation: light-gray bars; 10 % and 90 % Percentiles: green; 90 % RO uncertainty range: dark gray.

2.3.3 RO vs. RAOB Humidity Comparison

The specific humidity profiles as well as the specific humidity altitude slice are plotted up to a height of 100 hPa. Figure 2.29 and Figure 2.30 shows overall results for RAOB humidity validation. It has to be noted here once more that below 16 km, i.e. for the whole domain of the validation of the specific humidity data, the RO specific humidity is correlated with the ECMWF short term forecast field because of the 1D-Var approach.

For the humidity currently there is not yet an RO error model defined so that no dary gray uncertainty ranges are plotted here; as a rough guess, the RO specific humidity uncertainty should be expected to be not smaller than about 10 % to 25 % (as for example shown in Ladstädter et al. [Lad+15]).

As for the discussion of the MIPAS results in one of the previous sections see the MM-ValRO validation website http://validate.globclim.org for detailed results for different altitude layers (relevant for RAOB humidity are the 800 hPa to 500 hPa and the 500 hPa to 200 hPa layers) and the individual months.

In mid 2006 the bias characteristics above about 200 hPa changes. Figure 2.29 shows that before mid 2006 there was a change from a positive to a negative bias of RO vs. RAOB. After mid 2006 this change vanishes. In general Figure 2.29 does not give a good view on the systematic differences between RO and RAOB since the mean differs a lot from the median for specific humidity. This can clearly be seen in Figure 2.30. Top panel of Figure 2.30 shows the validation time series for the 500 hPa to 200 hPa layer whereas in the bottom panel the same is shown for the 800 hPa to 500 hPa layer. One can clearly see here that the mean of the 500 hPa to 200 hPa layer lies between 70 % to 80 % whereas the median is almost eveywhere below 50 %. For the layer between 800 hPa to 500 hPa the same is true although the absolute values are a little bit less.

An interesting feature which can be found in top panel of Figure 2.30 is that there a quite strong seasonal dependency of the median between 2007 and 2012 which seems to decrease afterwards. In addition, it can be found that the general offset between RAOB and RO is changing for about 20 %. The reason for that could be on the one hand the transition from a single satellite to a multi-satellite RO dataset but – more reasonable – a big change in the global usage of sonde-types: In 2006 the Vaisala RS80 sondes are strongly decreasing and the Vaisala RS92 sondes are strongly increasing.

In order to enable a more detailed look at the behavior of individual months beyond inspecting the altitude layers over time, the separate plots as a function of altitude that are available per month are useful. They show the RO validation in an pressure-resolved manner. As examples Figure 2.31 and Figure 2.32 show this detailed look for a “CHAMP only” month (November 2005; Figure 2.31) and a “CHAMP/COSMIC” month (July 2007; Figure 2.32); the same type of plots is available for all months on the webpage http://validate.globclim.org.

Figure 2.31 is one of the best-matching humidity comparisons. Note that humidity is

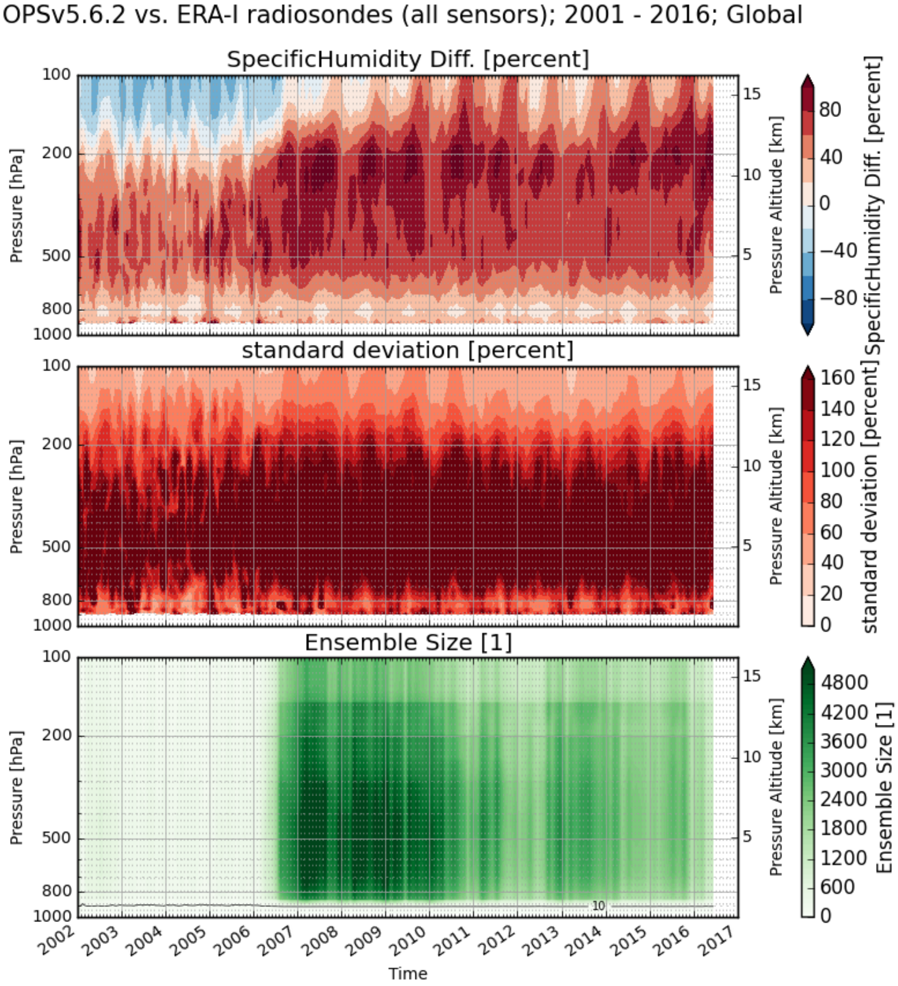

Figure 2.29: Global RO versus RAOB humidity validation results of the troposphere (1000 hPa to 100 hPa) and the number of collocated profiles as a function of time from 2002 to 2016.

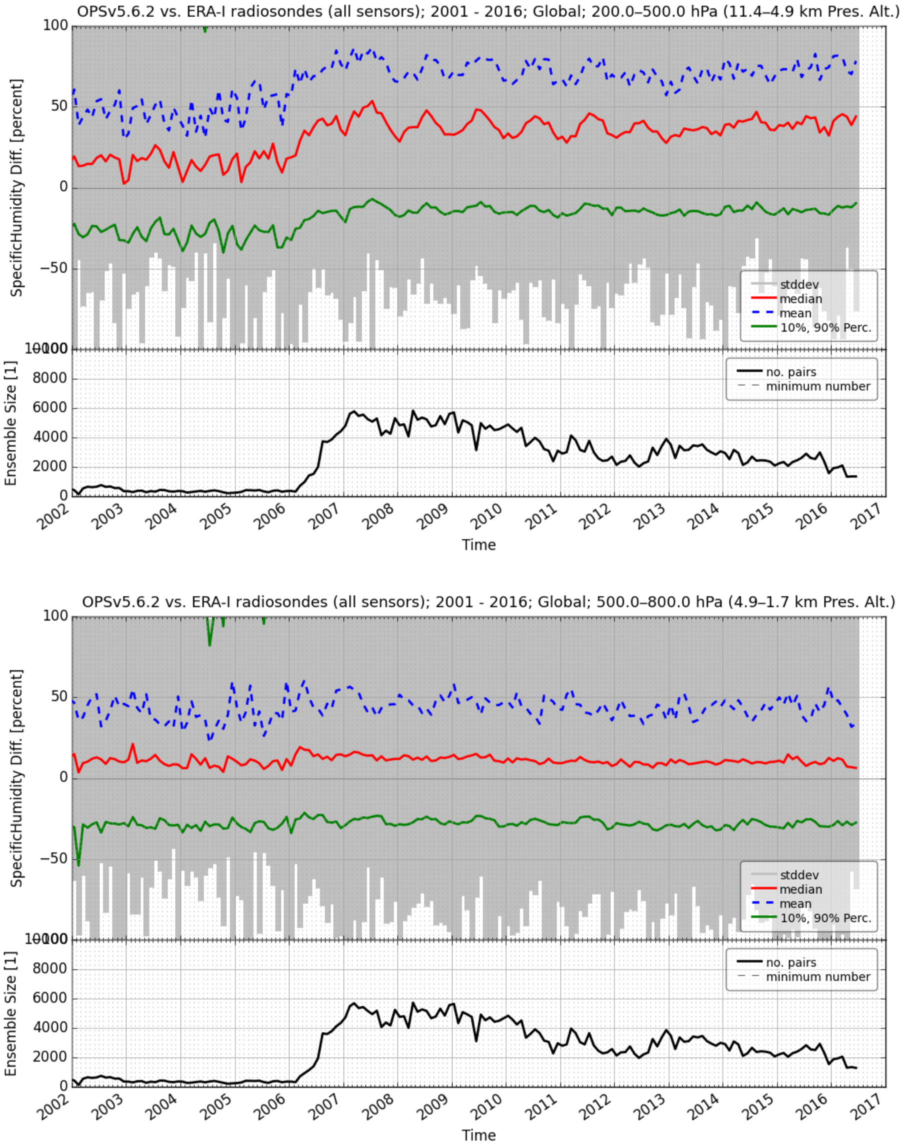

Figure 2.30: Global RO versus RAOB humidity validation results for the troposphere (800 hPa to 500 hPa and 500 hPa to 200 hPa) and the number of collocated profiles as a function of time from 2002 to 2016. Mean systematic differences: blue; median differences: red; standard deviation: light-gray bars; 10 % and 90 % Percentiles: green.

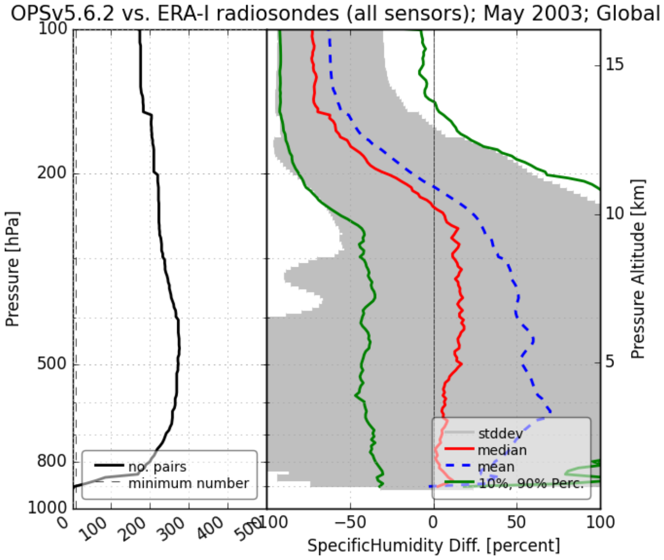

Figure 2.31: Global RO versus RAOB humidity validation results from 1000 hPa to 100 hPa and the number of collocated profiles for May 2003. Mean systematic differences: blue; median differences: red; standard deviation: light-gray bars; 10 % and 90 % Percentiles: green.

a variable showing strong vertical and horizontal variability, so the standard deviation is expected to be relatively large.

Figure 2.32 shows the general structure of a specific humidity validation profile in the time after beginning of 2006. It is worth mentioning that there is a big difference between the median and the mean systematic difference profile although the number of collocation pairs is quite high. In addition, the standard deviation is much larger than the 10 percent and 90 percent quantiles which implies that there have to be several large outliers in the humidity profile samples.

In general it has to be said, that due to the new RAOB dataset and some remaining QC issues the mean differences in humidity seem to be very high. It has to be mentioned that the vertical and horizontal structure of specific humidity is much more edged than that of temperature or pressure. Recent validation studies for specific humidity (cf. [Rie+16]) have shown that the differences of two collocated specific humidity measurements can be quite large due to frontal structures. This could imply that a tightening of our collocation criteria is needed for specific humidity.

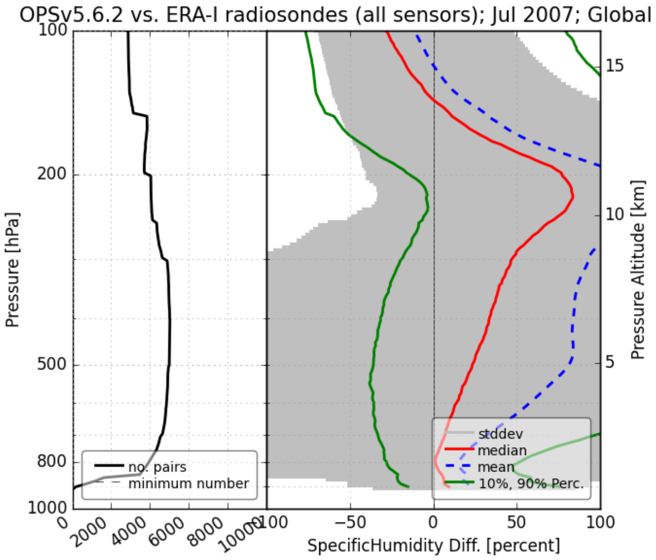

Figure 2.32: Global RO versus RAOB humidity validation results from 1000 hPa to 100 hPa and the number of collocated profiles for July 2007. Mean systematic differences: blue; median differences: red; standard deviation: light-gray bars; 10 % and 90 % Percentiles: green.

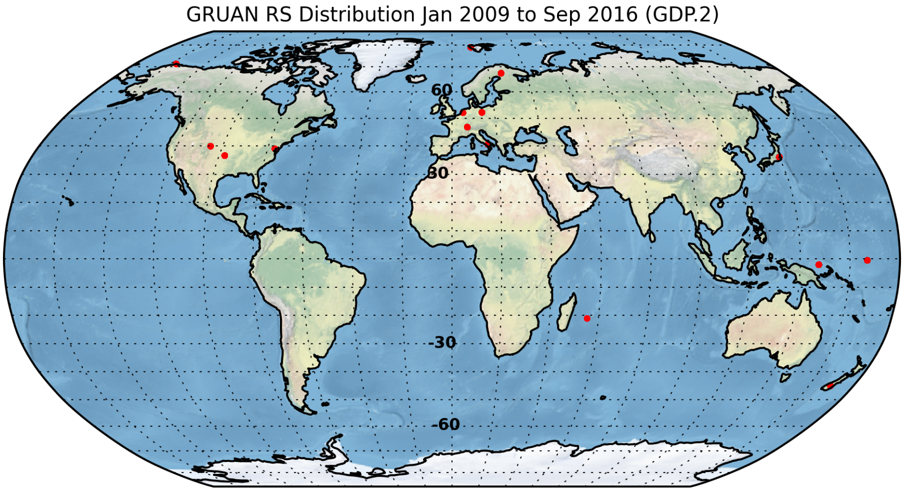

Figure 2.33: Map of GRUAN stations which were active in the study time period 2009 to 2016.

2.3.4 RO vs. GRUAN Comparison

Observations from the GPS[24] RO satellite technique and from the newly established GCOS Reference Upper Air Network are both candidates to serve as reference observations in the Global Climate Observing System. GRUAN delivers data only from a sparse selective network of radiosonde stations (cf.Figure 2.33; 12 stations 2009 – 2016) with an in-situ measurement principle and bias corrections applied.Owing to the strongly differing techniques, RO and GRUAN have their unique strengths and weaknesses. The current comparison shows the validation results between both datasets over 2009 to 2016.

Due to the sparse setup of the GCOS Reference Upper Air Network only two latitude bands are shown here: The northern mid-latitudes (30°N to 60°N) and the tropics (30°S to 30°N).

Figure 2.34 shows the comparison results between RO and GRUAN temperature profiles for the northern mid-latitudes (30°N to 60°N) between January 2009 and September 2016. The number of profiles which have been used for the comparison were 4523. One can see that RO and GRUAN are consistent within 0.2 K up to 30 hPa and stay whithin about 0.5 K up to 10 hPa. The biases above about 30 hPa can be attributed to a radiosonde daytime warm radiation bias, with only small possible contributions of a solar activity-related bias of the RO measurements. For a more detailed investigation of these biases cf.Ladstädter et al. [Lad+15].

---

[24] Global Positioning System

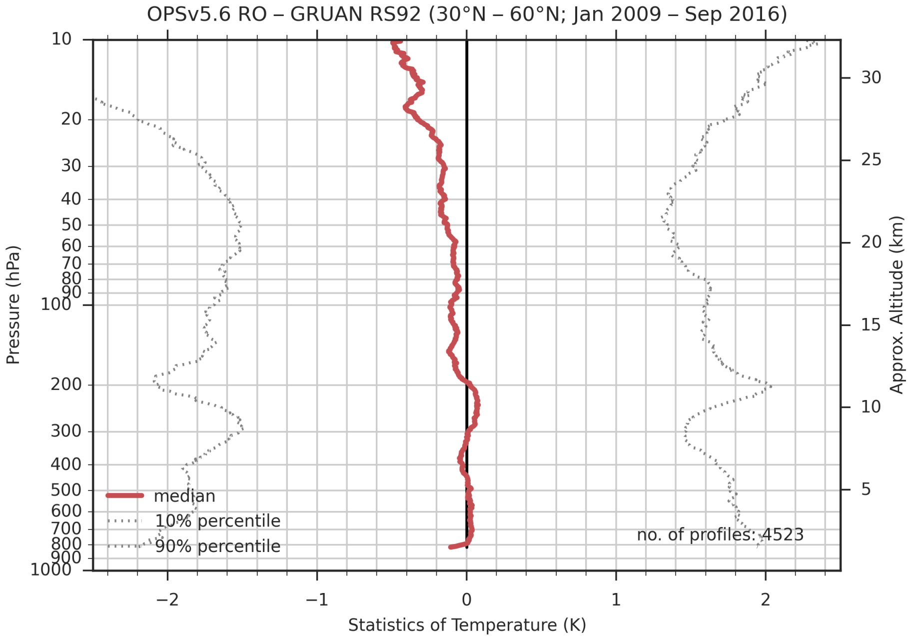

Figure 2.34: Comparison of temperature between RO and GRUAN for the time period 2009 to 2016 for all profile pairs between 30°N to 60°N.

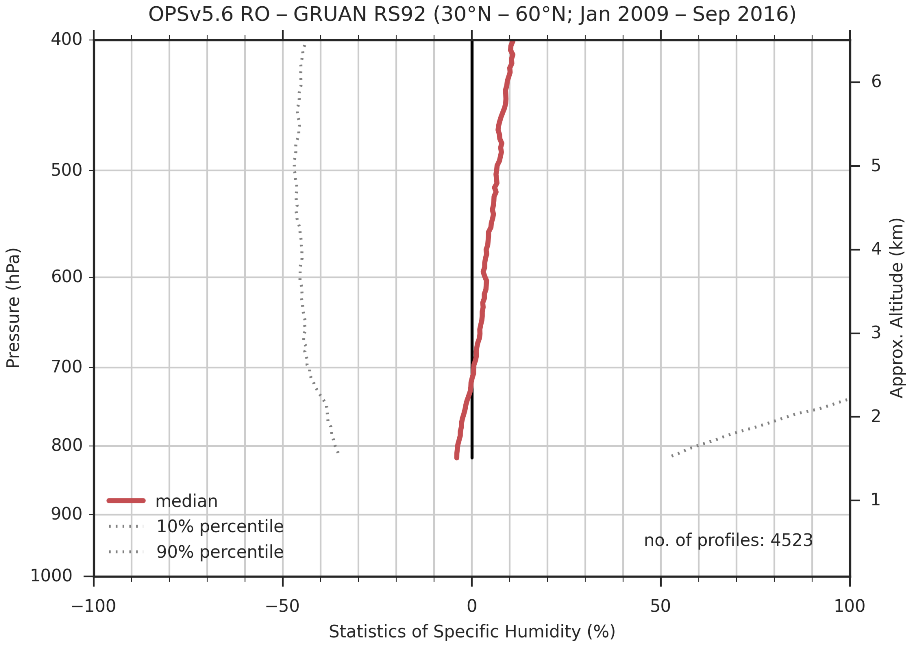

Figure 2.35: Comparison of specific humidity between RO and GRUAN for the time period 2009 to 2016 for all profile pairs between 30°N to 60°N.

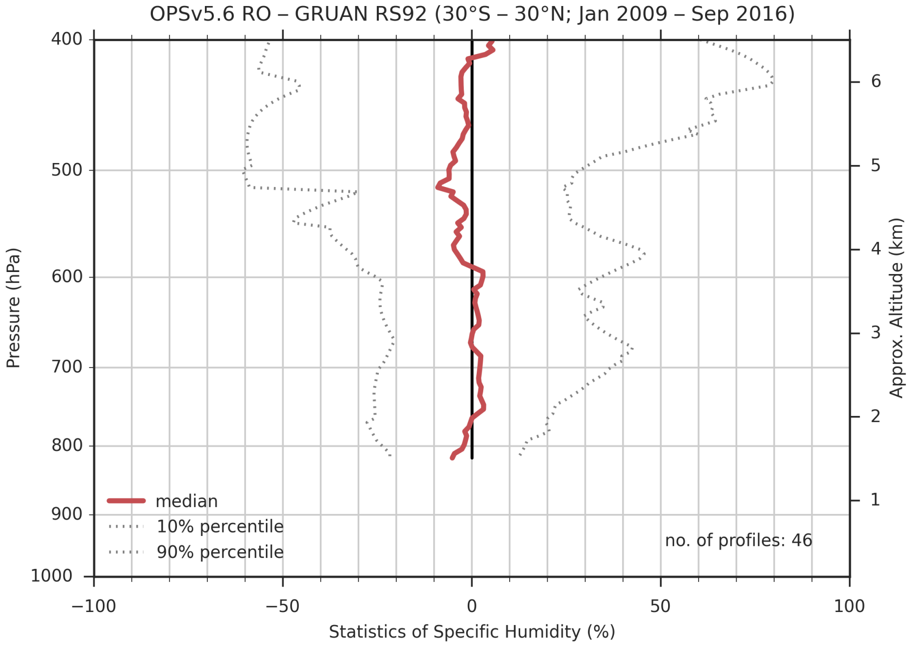

Figure 2.36: Comparison of specific humidity between RO and GRUAN for the time period 2009 to 2016 for all profile pairs between 30°S to 30°N.

Figure 2.35 shows the comparison results between RO and GRUAN specific humidity profiles for the northern mid-latitudes (30°N to 60°N) between January 2009 and September 2016. The number of profiles which have been used for the comparison were 4523. One can see that RO and GRUAN are consistent within 10 % up to 400 hPa. The large values of the 90 % percentile compared to the 10 % percentile implies that the distribution has a strong asymmetry. The reason therefore is not clear yet but is currently under investigation.

Figure 2.36 shows the comparison results for humidity for the tropics (30°S to 30°N). It serves as an example comparison for a region exhibiting high specific humidity. Since there are only two GRUAN stations in this latitude band which were active only between 2009 and 2011 the number of collocation pairs is rather small (46 pairs). Nevertheless, the median difference still stays within 10 % up to 400 hPa. The strong asymmetry between the 90 % percentile and the 10 % percentile are not present in this region. This could imply that values of small humidity or vertical regions where a strong humidity gradient occurs is not captured well by the RO measurements due to the more coarse vertical resolution; this will be subject of further studies.

3 The MMValRO Profiles Processing System – Structure and Process Design (PPS – SPD)

In this chapter the new version of the PPS[1] of the current MMValRO-E[2] project is described. The PPS performs the central tasks of the ESA[3] project ESRIN/Contract No. 4000110769/14/I-AM–MMValRO-E, in particular it handles the requirements of the work packages 3 and 4. As far as relevant for the MMValRO[4] project, also issues of other parts of WOCAS[5] are described here, i.e. the issues of the OPS[6] that delivers the input profiles for the PPS. Both PPS and OPS position and functions within the WOCAS are depicted in Kirchengast and Schwärz [KS10]. A semantic definition in this document's context is the distinction between external or non-RO[7] or candidate profiles, used synonymously, and internal or RO or reference profiles.

PPS Module identifiers have the prefix pps- throughout the software project and throughout this chapter.

3.1 Profiles Processing System Top-view Structure

Figure 3.1 depicts an overview on the PPS information flows, processes, and data. The general view shows the data streams and relevant processes starting from the registration of the L2[8] datasets in the specific databases over the collocation task and finishing on the one hand in the presentation of the validation results on a webpage (`validate.globclim.org`) and on the other hand on the production of HDF5[9]-files which are compliant to the

---

[1] Profiles Processing System

[2] Multi-Mission Validation by Satellite Radio Occultation – Extension Project

[3] European Space Agency

[4] Multi-Mission Validation by Satellite Radio Occultation

[5] Wegener Center Occultation and Climate Analysis System

[6] Occultation Processing System

[7] Radio Occultation

[8] Level 2

[9] Hierarchical Data Format Version 5

GEOMS[10] metadata standard. These files are then submitted to the NILU[11] Cal/Val[12] database.

It can be clearly seen that the main advantages compared to the previous setup of the PPS [cf. Sch+10] are the performing of the collocation via database requests, and the presentation of the validation results on a webpage.

Since the last updates of the of the PPS described in Schwärz et al. [Sch+13] further updates have been implemented:

- The database structure was completely redesigned. With the advantage of the know-how gathered in the last years this redesign led to less complicated queries and further improved the speed of the different applications like the validation or climatology creation, etc.
- Due to this restructuring we could generalize the validation application. Compared to the previous setup where it was possible to validate everything with RO data as reference only the current setup allows for validating each dataset registered in the database by any other dataset which is also registered in the database.
- In addition, it is possible to perform a validation where more than one candidate dataset is compared with the same reference dataset. In this setup it is also possible to select only those collocation pairs where profiles of both candidate datasets have the same reference profile as collocation partner.
- The new database design combined with the lessons-learned from the previous setup resulted in a further update in speed of about a factor 15 compared to the setup described in Schwärz et al. [Sch+13].

The database is organized utilizing different major tables/database applications. One is called PROF[13]. In this DB[14] the meta-data of the L1b[15] and L2 datasets which are produced internally and externally are stored. Further database applications used here are COLLOC[16] (for saving the data regarding the collocation pairs), VAL[17] (for storing the validation datasets and for providing the plot datasets for presentation on the webpage).

Within the MMValRO-E project the current design needs to handle the following data sources:

---

[10] Generic EO Metadata Standard

[11] Norwegian Institute for Air Research

[12] Calibration/Validation

[13] Wegener Center Profile and Phase-delay database application

[14] database

[15] Level 1b

[16] Wegener Center database for collocation datasets

[17] Wegener Center database for validation datasets

- ESA's processing centers for atmospheric MIPAS[18], GOMOS[19], etc. L2 profiles via straightforward ftp access. The meta-data of these profiles are stored in the so called PROF.

- Vaisala RS 80/90/92/41 radiosonde data from the ECMWF[20] reanalysis archive.

- The internally provided RO profiles (L2). The meta-data of these profiles are stored in the PROF. A more detailed view on the production of the retrieved RO profiles is given in Subsection 3.1.1.

As mentioned before, one of the major advantages compared to the previous setup is that the collocation task is now performed via database requests. In addition, the collocation and validation results as well as the produced plots are also registered in the database. The newly implemented usage of the database for storing the meta-data of the validation runs and the produced plots provides a strong advantage for presenting the results on the web. In addition, it gives the possibility for an in-depth examination of the statistics data for e.g. different months, etc.

3.1.1 Occultation Processing System

In this subsection a short overview on the OPS is provided. Figure 3.2 shows the processes and storage systems which form the OPS.

As can be seen two independent processes perform the download of ECMWF analysis and forecast fields as well as of the RO excess phase delay, POD[21], etc. data and their registration in the database. A *retrieval control process*, which is initiated by the Job-scheduler (cf. Subsection 3.1.3), then performs the database request for all excess phase delay data which have not been processed yet, as well as for the corresponding ECMWF analysis and forecast fields needed by the retrieval.

The central controlling unit for the OPS is the so called *grid-resource manager.* This part of the OPS controls the distribution of the retrieval jobs to the different computing nodes (a quite heterogeneous set of different machines on which the special OPS software package has to be installed on them). In addition it checks for already processed measurements and moves them to a place where they are automatically registered in the database.

---

[18] Michelson Interferometer for Passive Atmospheric Sounding
[19] Global Ozone Monitoring by Occultation of Stars
[20] European Centre for Medium-Range Weather Forecasts
[21] Precise Orbit Determination

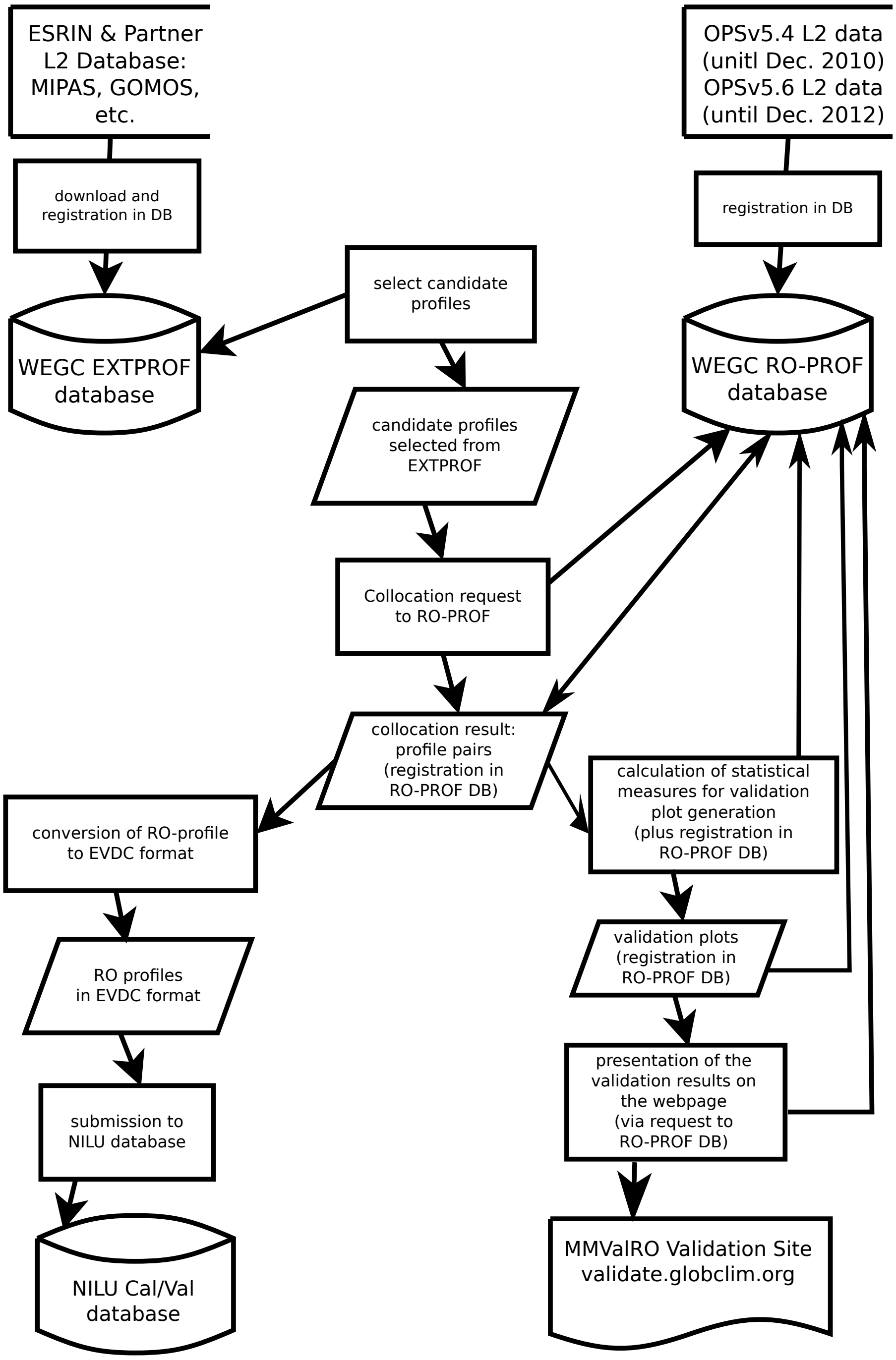

Figure 3.1: MMValRO PPS structure: information flows, processes and input and output data.

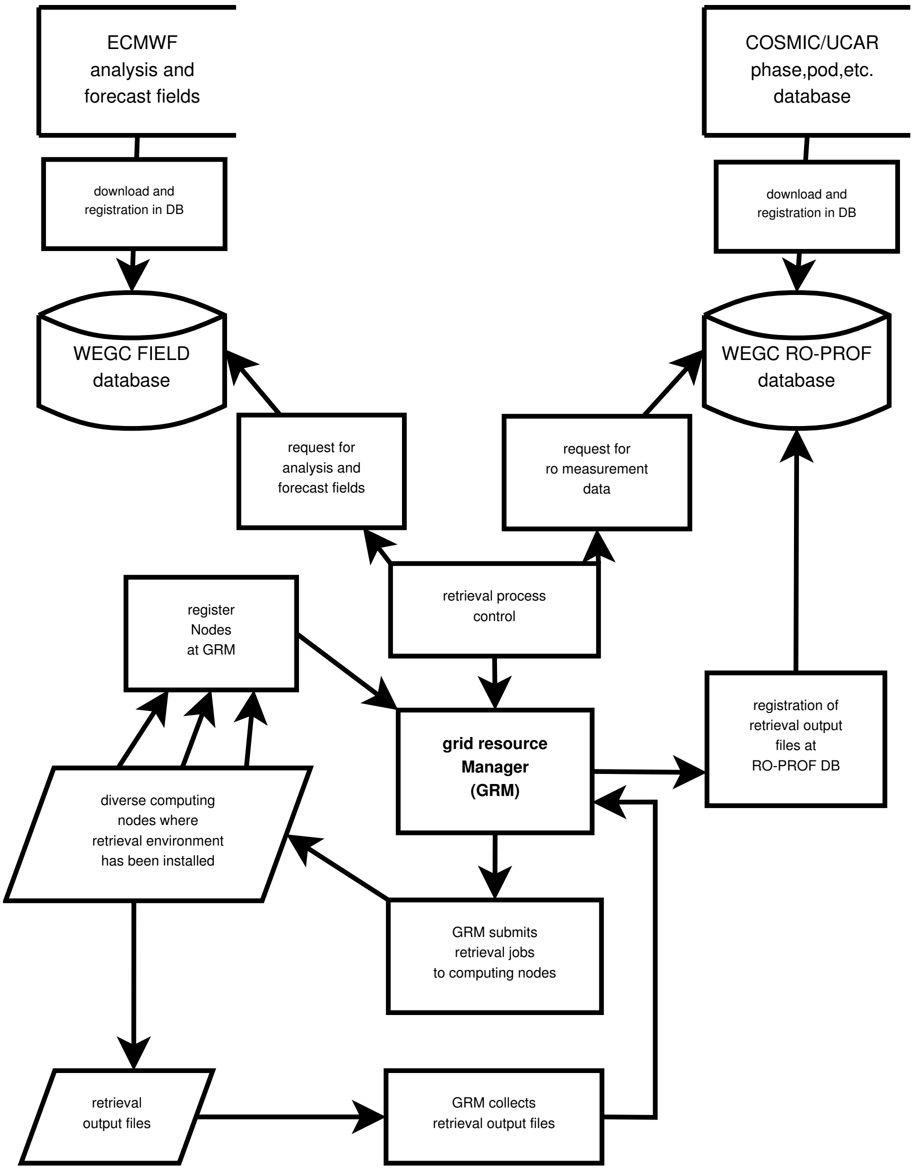

Figure 3.2: OPS structure: information flows, processes and input and output data.

3.1.2 Workload Assessment

The data stream for the external data regards incorporates L2 profiles of the ENVISAT[22] instruments GOMOS and MIPAS, as well as profiles of RAOB[23] data obtained from the reanalysis archive of the ECMWF. Even for the parsing of profile meta-data only, each profile file needs to be downloaded completely. From ground sites (Multi-TASTE[24] and VALID[25]) and validation campaigns basically no incoming data traffic arises (occasionally tables with updated coordinates only). Table 3.1 and Table 3.2 show the incoming amount of measurements for MIPAS and GOMOS, respectively.

The reprocessed data of the GOMOS and MIPAS data archive at ESA's processing centers is entirely mirrored to the PROF database. A more specific view on the data is given in Chapter 2. The overall size of the data managed by the PROF database is currently several Terabytes.

The outgoing data stream consists of the collocated RO profiles, which have to be submitted to the NILU Cal/Val database. Depending on the selected collocation criterion and the operational RO missions envisioned for use, the fraction of external profiles having an RO collocation partner is about 20 % (for estimates of the practically possible number see Table 3.4, showing the RO number of event statistics).

The internal data stream from the in-house RO retrieval is currently (November 2013) largely dominated by the F3C[26] part. Table 3.4 shows the amount of measurements for RO retrieval datasets.

The PPS *fast-track* data stream will generally cover a fraction of these numbers only, because here only those RO L1[27] data will be downloaded and processed through the OPS, which are available "near real time" or at least within a latency of 42 hours in order to ensure completion of the fast-track processing within the follow-on day of measurements (i.e., at least within 48 hours from the beginning of the previous day for which all retrievals need to be available during the follow-on day). The *postprocess-track* data stream (processing the "time delayed" RO L1a[28] data) will cover all available "time delayed" data. In general this means that after about a month the *fast-track* validation results will be replaced by the *postprocess-track* results.

---

[22] Environmental Satellite

[23] Radiosonde Observation (Rawinsonde Observation)

[24] Multi-Mission Validation by Sounders, Spectrometers, and Radiometers

[25] Satellite Validation with LIDAR Data

[26] FORMOSAT-3/COSMIC

[27] Level 1

[28] Level 1a

Table 3.1: Number of MIPAS profiles until April 2012.

MIPASv6.0	**2002**	**2003**	**2004**	**2005**	**2006**	
All	93359	306952	87885	124784	164713	
Jan	0	30652	25502	15342	15604	
Feb	0	24115	21334	10912	12288	
Mar	0	22834	19090	16415	9763	
Apr	0	18380	0	13779	5721	
May	0	16272	0	6915	18495	
Jun	0	25133	0	10434	17960	
Jul	0	29523	0	10540	12618	
Aug	0	29839	19378	0	19548	
Sep	20749	23433	2581	2979	11431	
Oct	19198	30382	0	12736	15118	
Nov	25057	29647	0	10984	13570	
Dec	28355	26742	0	13748	12597	
MIPASv6.0	**2007**	**2008**	**2009**	**2010**	**2011**	**2012**
All	290491	425787	429678	424334	428848	119790
Jan	21937	37986	35243	39948	37497	37274
Feb	19200	35678	34360	34937	35141	34522
Mar	16838	36605	38925	39555	38197	38398
Apr	23828	35694	27558	38199	34405	9596
May	21955	28933	39798	30279	30312	
Jun	18834	37221	38397	36272	37073	
Jul	30299	38209	38760	38157	39616	
Aug	30961	36055	36483	36341	37149	
Sep	24308	35350	35327	36483	33156	
Oct	24139	28247	36901	20957	28410	
Nov	28998	36773	28702	34350	37718	
Dec	29194	39036	39224	38856	40174	

Table 3.2: Number of GOMOS profiles until April 2012.

GOMOSv6.01	**2002**	**2003**	**2004**	**2005**	**2006**	
All	36254	85089	126007	39194	93378	
Jan	0	12882	12633	11029	10590	
Feb	0	8230	12197	0	9059	
Mar	0	9206	13625	0	7665	
Apr	0	10675	12133	0	8264	
May	0	0	13329	0	8905	
Jun	0	0	0	0	7488	
Jul	0	5693	13277	2184	7847	
Aug	0	12460	12689	3786	7397	
Sep	8182	0	11789	6605	5723	
Oct	6358	0	0	6787	6784	
Nov	7625	12365	11807	0	5252	
Dec	14089	13578	12528	8803	8404	
GOMOSv6.01	**2007**	**2008**	**2009**	**2010**	**2011**	**2012**
All	96638	106173	30006	84644	70668	968
Jan	11116	12146	11637	10088	10268	0
Feb	8238	9278	0	4869	7197	438
Mar	7254	9451	0	9892	8654	530
Apr	8682	8920	0	8466	8304	0
May	8829	10373	0	8646	8786	
Jun	8485	9072	0	8716	8220	
Jul	7595	6132	0	8207	8382	
Aug	7697	8578	0	9163	8947	
Sep	4917	6312	0	5004	1910	
Oct	6791	8242	0	0	0	
Nov	7676	6126	7254	484	0	
Dec	9358	11543	11115	11109	0	

Table 3.3: Number of RAOB profiles until May 2012.

RAOB	**2002**	**2003**	**2004**	**2005**	**2006**	
All	35610	38288	43946	53740	115244	
Jan	2407	3273	3511	3775	6921	
Feb	2370	2913	3287	3326	6927	
Mar	2807	3290	3494	3779	8031	
Apr	2888	3117	3477	3712	8146	
May	3112	3164	3773	4048	8901	
Jun	3093	3079	3634	4268	9515	
Jul	3312	3266	3968	4639	10470	
Aug	3236	3202	3958	4663	11276	
Sep	3085	3170	3723	4569	11001	
Oct	3116	3262	3614	5048	11286	
Nov	3015	3124	3559	5476	11129	
Dec	3169	3428	3948	6437	11641	

RAOB	**2007**	**2008**	**2009**	**2010**	**2011**	**2012**
All	149872	167186	160726	176454	179392	72188
Jan	11772	13386	13740	13768	15348	15189
Feb	10934	12913	12470	13418	14312	14086
Mar	12348	13970	13794	14469	15202	14738
Apr	12074	13533	13019	14685	14406	13878
May	12682	14092	13102	14709	14290	14297
Jun	12369	13791	13097	14666	14713	
Jul	13019	14246	13242	14418	14764	
Aug	13118	14226	13936	15500	15506	
Sep	12393	14111	12988	14507	14524	
Oct	13337	14361	13789	15606	15617	
Nov	12741	14171	13218	15166	15050	
Dec	13085	14386	14331	15542	15660	

Table 3.4: Number of RO profiles until May 2012.

OPSv5.6	**2002**	**2003**	**2004**	**2005**	**2006**	
All	58591	62624	57425	53783	368362	
Jan	2952	5463	5385	3614	4973	
Feb	2541	5079	4965	4151	4811	
Mar	4656	5313	4612	5308	10666	
Apr	5201	4761	4702	3940	13522	
May	5451	5684	5288	4250	19609	
Jun	4497	5266	4344	4647	22894	
Jul	6187	5616	4478	4826	25263	
Aug	6232	5352	4798	3381	50593	
Sep	5523	5363	4220	4244	44613	
Oct	5156	5089	4574	5535	53734	
Nov	4798	4883	5035	4809	56164	
Dec	5397	4755	5024	5078	61520	
OPSv5.6	**2007**	**2008**	**2009**	**2010**	**2011**	**2012**
All	882388	877759	837641	678959	603757	192245
Jan	68211	70437	80615	69909	46877	34359
Feb	77373	76364	61879	61389	44578	36924
Mar	86173	56622	73459	67147	62155	40600
Apr	77545	85581	75787	66877	58210	43621
May	82946	72731	72713	50598	51433	36741
Jun	72688	71398	51159	56302	53219	
Jul	76337	79349	80113	62290	62900	
Aug	82323	78545	70124	57858	50818	
Sep	61479	73143	72140	50708	48109	
Oct	66151	80294	68390	47658	40820	
Nov	57218	66811	65145	39353	39631	
Dec	73944	66484	66117	48870	45007	

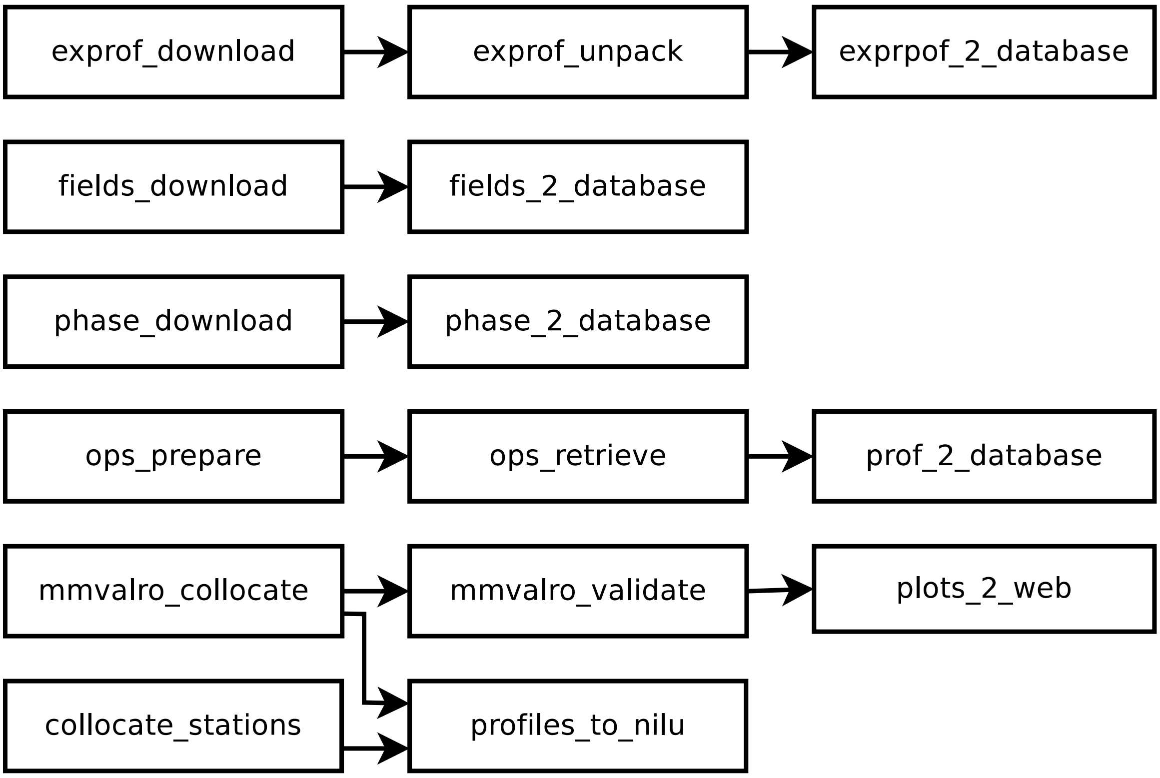

Figure 3.3: Job chains implemented via the job scheduler.

3.1.3 PPS and OPS Automation Issues

The redesigned OPS system control and the newly designed PPS system have been implemented in terms of automatic and smart recoveries on failures, to minimize human workload in the long term.

Both operational processes mentioned here (PPS and OPS), are controlled by the job scheduling and monitoring software *Job Scheduler*, an open source project with the homepage `http://www.sos-berlin.com/`. This job scheduler allows to organize different dependent jobs in so called job chains to ensure sequential processing. Job starts can be triggered by directory notification, built-in calendars or a web user interface.

Figure 3.3 shows the job-chains relevant to the PPS. Currently there are six independent job-chains defined—three for the download of the data from diverse data providers, two for the processing, and one for uploading the collocated RO profiles to the NILU Cal/Val database:

- download external profiles and register them in the PROF database;

- download the ECMWF fields and register them in the FIELD[29] database;
- download the phase delay datasets and register them in the PROF database;
- prepare the input data for the OPS processing, process the data, and then register the resulting RO profiles in the PROF database;
- perform the collocation and validation between the external profiles and the RO profiles;
- perform the collocation between the Multi-TASTE and VALID station locations and the RO profiles;
- upload collocated RO profiles to NILU.

The presentation of the validation results on the webpage is independent of these job-chains: as soon as a plot is registered in the database it can be viewed on the web.

In Table 3.5 the system runtime schedule as well as a description what exactly the chain is responsible for is presented.

3.1.4 Key PPS Algorithms

In this subsection the key algorithms used in this validation framework are briefly described.

Collocation Between "Candidate" and "Reference" Profiles

According to the results presented in [Sof+08], the collocation procedure is set up as follows: In a first step all RO profiles with a maximum space distance of 300 km and a maximum time distance of 3 hours are selected within the database. For the calculation of the spatial distance between the two profile locations the PostgreSQL database provides internal routines, which are based on spherical trigonometry (great circle distances). The time distance is converted with an adopted wind speed of $100\,\mathrm{km\,h^{-1}}$ to a space distance, which is added to the great circle distance to yield the total effective distance (e.g., a time distance of 1 hour of a candidate profile from the RO profile leads to an additional distance of 100 km). From the set of returned profiles the first one with the smallest effective distance is chosen, since the set of profiles is returned in increasing order of effective distance.

Provision of RAOB Profiles

For the provision of the high-quality Vaisala RS 80/90/92/41 RAOB measurements we apply the following steps:

---

[29] Wegener Center Atmospheric Field database

Table 3.5: Overview on the time lines and dependencies of the PPS.

chain name	start time	performs
exprof_2_database	once per day	download of external profile data (RAOB) and registration in the PROF database
field_2_database	once per day	download of ECMWF fields and registration in the FIELD database
pd_2_database	once per day	download of phase delay data and registration in the PROF database
ops_process	once per day	provision of matching phase delay files and ECMWF fields; processing of the retrieval; registration of the results in the PROF database
collocate_validate	each 1st and 16th per month	collocation between the external profiles and the RO profiles; validation of the collocated profiles; presentation of the validation results on a webpage; submission of the collocated profiles to the NILU atmospheric database
collocate_stations	once per day	collocation of the retrieved RO profiles with the Multi-TASTE and VALID station locations; conversion of these profiles to the EVDC[30] format and submission of these profiles to the NILU atmospheric database

- a minimum pressure range between 200 hPa and 500 hPa has to be present for both temperature and humidity.
- in this core range the maximum pressure altitude gap must not be larger than 4 km.
- outside the core range the profile is cut at the occurrence of the first gap which is larger than the maximum pressure altitude gap allowed within the core range.
- for the resulting profile, values within the remaining gaps are interpolated from the existing values.

MIPAS Quality Control

For MIPAS no extra quality control step is included after the collocated profiles have been selected. If there is a temperature and pressure profile present in the MIPAS profile dataset (that is in the respective Level 2 files) the profile is included in the validation ensemble. From experience so far it is rare that the MIPAS meta-data flag that indicates a suitable temperature and pressure retrieval is indicating a problem.

GOMOS Quality Control

The quality control for GOMOS contains the following criteria—based on experience from the GOMOS user community on what influences the quality of those data (Viktoria Sofieva, personal communications, 2013)—in order to allow a GOMOS profile to be included in the validation ensemble:

- The magnitude of the star involved in the stellar occultation event has to be lower or at least equal to a magnitude 2.5.
- The value for the parameter "star-illumination-condition" has to be 0 or 3.
- For the obliquity (*ob*) the following constraint has been introduced: $|\mathrm{ob}| < 45$.

In particular, these criteria hold for the HRTP[31] data but not necessarily for the O_2/density data. They lead to significant reduction (often more than 90 %) of the number of collocated GOMOS profiles that actually enter the validation ensemble. The criteria may be further fine-tuned in the future (e.g., defining a separate set of exclusion reasons for the O_2/density data).

---

[31] High Resolution Temperature Profile

RAOB Quality Control

For the Vaisala RS 80/90/92/41 RAOB measurements we apply the following criteria:

- A profile is rejected if the RAOB provision algorithm fully rejects the profile.
- A profile is rejected if only one geopotential height entry exists for the whole profile (so that no interpolation is possible)

In general, except these few criteria no additional quality control step is currently performed, i.e. if the RAOB measurement passed the provision process it is used in the validation step. This might possibly also be refined in future, in particular if the RAOB selection is desired to be restricted to the highest-quality class of profiles.

Estimation of the Statistical Measures Used for the Validation

The statistical measures used for the validation, the bias (systematic difference) and the standard deviation, are defined as follows [see e.g., SK04, or any good standard statistical textbook]:

We define difference profiles $\Delta\mathbf{x}$ ($\Delta\mathbf{x} = (\Delta x_1, \ldots, \Delta x_i, \ldots, \Delta x_N)^{\mathrm{T}}$, with i denoting the height levels, N the number of height levels in the profiles, and ^{T} the matrix transpose) between the candidate profile, $\mathbf{x}_{\mathrm{cand}}$, and the reference profile, $\mathbf{x}_{\mathrm{ref}}$, in the form:

$$\Delta\mathbf{x} = (\mathbf{x}_{\mathrm{cand}} - \mathbf{x}_{\mathrm{ref}})\,. \tag{3.1}$$

Given these difference profiles, the calculation of the mean of the difference profiles leads to the bias profile, $\mathbf{b}$:

$$\mathbf{b} = \left[\frac{1}{n}\sum_{k=1}^{n}\Delta\mathbf{x}_k\right], \tag{3.2}$$

where n denotes the number of events in the ensemble. As a next step, the bias is subtracted from each profile, giving the bias-free profiles, $\Delta\mathbf{x}_{\mathrm{biasfree}}$:

$$\Delta\mathbf{x}_{\mathrm{biasfree}} = \Delta\mathbf{x} - \mathbf{b}. \tag{3.3}$$

With these bias-free profiles we can compute the empirical error covariance matrix, $\mathbf{S}_{\mathrm{empir}}$:

$$\mathbf{S}_{\mathrm{empir}} = \left[\frac{1}{n-1}\sum_{k=1}^{n}(\Delta\mathbf{x}_{k,\mathrm{biasfree}})\,(\Delta\mathbf{x}_{k,\mathrm{biasfree}})^{\mathrm{T}}\right], \tag{3.4}$$

with its diagonal elements, S_{ii}, representing the variances at height level i and with its non-diagonal elements, S_{ij}, representing the covariances between height levels i and j. The square root of the diagonal of the error covariance matrix gives the standard deviation profile, $\mathbf{s}$:

$$\mathbf{s} \qquad \text{with:} \qquad s_i = \sqrt{S_{ii}}. \tag{3.5}$$

The root mean square error profile, rms, finally reads:

$$\text{rms} \qquad \text{with:} \qquad \text{rms}_i = \sqrt{b_i^2 + s_i^2}. \tag{3.6}$$

The PPS validation system focuses on using the resulting bias profiles and standard deviation profiles, which are provided as validation results in visualized form at the MMValRO validation website (`http://validate.globclim.org`); see also the results section below for example results.

Interpolation to a common vertical grid

In order to build the differences between the two profiles of a collocation pair first the data has to be interpolated to a common vertical grid. Depending on the used atmospheric parameter the following interpolation methods were used:

Temperature, dry temperature : linear interpolation

Pressure, dry pressure : the logarithm of the pressure values are linearly interpolated

Altitude : linear interpolation

Specific humidity : the logarithm of the humidity values are linearly interpolated

Density : the logarithm of the density values are linearly interpolated

Additionally, in case of a pressure grid the grid values were chosen to be equidistant on a log-pressure grid.

Data Smoothing for Matching Data Resolution

To use both the candidate and reference profiles at the same vertical resolution, both are smoothed to the same matching resolution, before computing the validation statistics. For this purpose we use, based on experience of the remote sensing validation community (cf.[SD10]), a Gaussian window of the width w equal to the quadratic difference of the widths of the averaging kernels of the low-resolution data, $w_{\text{low-resolution}}$, and the high-resolution data, $w_{\text{high-resolution}}$:

$$w^2 = w^2_{\text{low-resolution}} - w^2_{\text{high-resolution}}. \tag{3.7}$$

Note that for a Gaussian window the FWHM[32] is 2.355σ (with σ as the standard deviation); this is important to implement the Gaussian window properly. Consistent with the averaging

---

[32] Full Width at Half Maximum

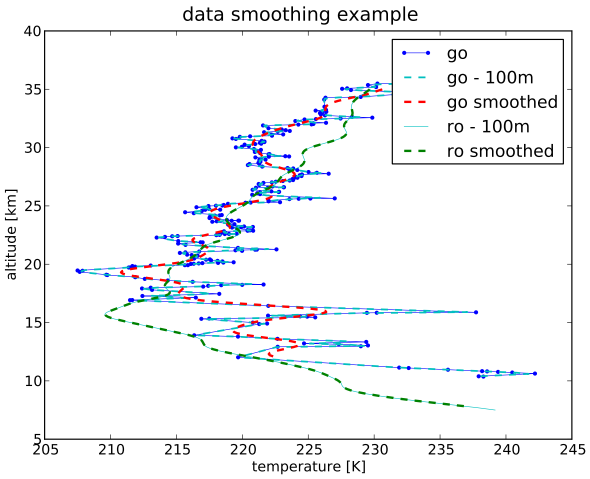

Figure 3.4: Data smoothing example for an arbitrarily chosen collocated profile pair of GOMOS and RO data from August 8, 2005. Explanation see text.

kernel resolution of the respective data, the FWHM is set to 250 m for the GOMOS HRTP data, 2 km for the MIPAS data (this was chosen by inspecting representative averaging kernels of MIPAS profiles), and 1 km for the RO profiles.

Practically speaking, the higher-resolution data are smoothed to the resolution of the lower-resolution data, i.e., in case of GOMOS these data are smoothed towards the RO resolution, while in case of MIPAS the RO data are smoothed towards the MIPAS resolution.

As an example for the application of data smoothing via a Gaussian window filter, Figure 3.4 shows the smoothed and non-smoothed profiles for an arbitrarily chosen collocated profile pair of GOMOS and RO data from August 8, 2005. The GOMOS profile was measured at latitude 36.0°S, longitude 127.8°E, 13:53 UTC[33] and the RO profile at latitude 33.8°S, longitude 129.5°E, 16:25 UTC.

Figure 3.4 shows the raw GOMOS data indicated by the blue data points connected by the blue line. The bold dashed line shows the GOMOS data linearly interpolated to a 100 m grid. This interpolation is needed since the Gaussian window filter is applicable only on an equidistant grid. One can see that there is almost no difference between these two curves. The dashed red line finally shows the GOMOS profile after the application of the Gaussian window filter. One can clearly see that the smoothed data result in a better match between the GOMOS and the collocated RO profile, indicated by the bold dashed green line.

From Figure 3.4 it can also be seen that the smoothing of the lower-resolved dataset (in

---

[33] Universal Time Coordinated

this case the RO dataset) is not changed by the smoothing procedure; there is no appreciable difference between the raw RO profile (light cyan line) and the smoothed RO profile (bold dashed green line).

In case of the MIPAS data we also decided to use the approach of smoothing the data with a Gaussian window although the MIPAS dataset contains the averaging kernels. Wang et al. [Wan+04] found that the different vertical resolutions of RO and MIPAS can introduce a bias of about 1 K only near the tropical tropopause, i.e., where there is a sharp kink that in case of non-matched resolution is better resolved by RO. At other heights, the MIPAS vs. RO differences show virtually no changes in magnitude between matched to non-matched resolutions, just some small vertical structures, and the standard deviations are increased by less than 0.5 K. In future we intend to take the altitude-dependent MIPAS resolution, as expressed by the averaging kernels, more directly into account.

3.2 Specification of the PPS Modules

3.2.1 pps-exprof-download

Description

Mirroring of the external ESA L2 profile archives for GOMOS and MIPAS, and of the external RAOB profiles, to a local disc.

Inputs

ESA/ESRIN[34] ENVISAT archive data (for MIPAS and GOMOS). ECMWF ERA-Interim archive data (for RAOBs).

Outputs

- MIPAS, GOMOS: Unpacked datasets in a format which is readable by the BEAT[35] library.
- RAOBs: one netcdf files per RAOBs station per month.

Technical Description

Used infrastructure	standard x64 Linux compute server
Programming language	Python
Current status	operational

---

[34] European Space Research Institute

[35] Basic ENVISAT Atmospheric Toolbox

3.2.2 pps-exprof-2-db

Description

Registration of the external ESA L2 profile datasets, and of the external RAOB datasets, in the PROF database.

Inputs

- MIPAS, GOMOS: Unpacked datasets in a format which is readable by the BEAT library.
- RAOBs: netcdf files for each single RAOBs measurement.

Outputs

Database entries for each single profile dataset.

Technical Description

Used infrastructure	standard x64 Linux compute server, PostgreSQL database version 9.4
Programming language	Python
Current status	operational

3.2.3 roprof-2-db

Description

Registration of new local OPS L2 RO profile datasets in the PROF database.

Inputs

RO profile datasets retrieved by the OPS.

Outputs

Database entries for each single profile dataset.

Technical Description

Used infrastructure	standard x64 Linux compute server, PostgreSQL database version 9.4
Programming language	Python
Current status	operational

3.2.4 pps-sel-cand

Description

Selection of candidate profiles for the collocation according to the specified input.

Inputs

- Time range for the profile selection;
- Candidate instrument (MIPAS, GOMOS, and RAOB);
- Used processor version;
- Diverse quality control specifications specific for the respective instruments.

Outputs

The meta-data of a set of candidate profiles.

Technical Description

Used infrastructure	standard x64 Linux compute server, PostgreSQL database version 9.4
Programming language	Python
Current status	operational

3.2.5 pps-collocate

Description

Collocation request to the PROF database for RO reference profiles for the previously selected candidate profiles.

Inputs

- Candidate profile set selected by *pps-sel-cand* (cf. Subsection 3.2.4).
- Maximum spatial distance between the two profiles.
- Maximum temporal distance between the two profiles.

Outputs

Collocated RO reference profiles for the previously selected candidate profiles.

Technical Description

Used infrastructure	standard x64 Linux compute server, PostgreSQL database version 9.4
Programming language	Python
Current status	operational

3.2.6 pps-collocations-2-db

Description

Registration of the collocated profile pairs in the COLLOC table.

Inputs

- Candidate profile set (MIPAS, GOMOS, and RAOB) selected by *pps-sel-cand* (cf. Subsection 3.2.4);
- Collocated RO reference profiles for the previously selected candidate profiles (cf. Subsection 3.2.5);
- Actual space distance between candidate and reference profiles;
- Actual time difference between candidate and reference profiles;
- Measurement time of candidate profile;
- Measurement location of the candidate profile.

Outputs

Database entries for each single collocation dataset.

Technical Description

Used infrastructure	standard x64 Linux compute server, PostgreSQL database version 9.4
Programming language	Python
Current status	operational

3.2.7 pps-collocate-special-stations

Description

Collocation request to the PROF database for RO reference profiles for the station locations of the Multi-TASTE and VALID projects.

Inputs

- Locations of the Multi-TASTE and VALID station locations;
- Maximum spatial distance between the two profiles.

Outputs

Collocated RO reference profiles for the selected station locations.

Technical Description

Used infrastructure	standard x64 Linux compute server, PostgreSQL database version 9.4
Programming language	Python
Current status	operational

3.2.8 pps-validate

Description

Calculation of the statistical comparison measures between candidate profiles and reference profiles.

Inputs

- Profile pairs to validate selected by *pps-collocate* (cf. Subsection 3.2.5) and obtained from database.
- Minimum profile pair number for performing the calculation of the statistical measures.
- Borders for spatial region (spatial-bin) in which profiles are selected.
- Time range (time-bin) in which profiles are selected.

Outputs

- Statistical measures: estimated systematic difference, estimated standard deviation, and 10 %, 50 % (median), and 90 % percentiles of candidate versus reference profiles; uncertainty estimates for the reference (RO) profiles.
- Number of collocated profiles used for calculating the statistical measures.
- Statistical measures for layer averages: estimated systematic difference, estimated standard deviation; uncertainty estimates for the reference (RO) layer averages.

Technical Description

Used infrastructure	standard x64 Linux compute server, PostgreSQL database version 9.4
Programming language	Python
Current status	operational

3.2.9 pps-validate-2-db

Description

Registration of the validation datasets in the VAL table.

Inputs

- Statistical measures calculated by *pps-validate* (cf. Subsection 3.2.8);
- Number of collocated profiles calculated by *pps-validate* (cf. Subsection 3.2.8);
- Borders for spatial region (spatial-bin) in which profiles are selected;
- Time range (time-bin) in which profiles are selected.

Outputs

Database entries for each single validation dataset.

Technical Description

Used infrastructure	standard x64 Linux compute server, PostgreSQL database version 9.4
Programming language	Python
Current status	operational

3.2.10 pps-plot

Description

Plot generation for all validation datasets registered in the database (cf. Subsection 3.2.9).

Inputs

Statistical measures and number of collocated profiles calculated by *pps-validate* (cf. Subsection 3.2.8) and obtained from database.

Outputs

Plots for each database entry of a validation dataset.

Technical Description

Used infrastructure	standard x64 Linux compute server, PostgreSQL database version 9.4
Programming language	Python
Current status	operational

3.2.11 pps-plot-2-db

Description

Registration of the plots generated by *pps-plot* in the database (cf. Subsection 3.2.10).

Inputs

Plots generated by *pps-plot* (cf. Subsection 3.2.10) and obtained from database.

Outputs

Database entries for each single plot.

Technical Description

Used infrastructure	standard x64 Linux compute server, PostgreSQL database version 9.4
Programming language	Python
Current status	operational

3.2.12 pps-present

Description

Presentation of the validation results on the webpage: `http://validate.globclim.org`.

Inputs

- Vertical-profile plots of the statistical measures for each time bin (e.g., each month);
- Time-series plots for each year since the start year of each mission;
- Overall time-series plots for the whole mission duration;
- Overall time-altitude slice plots for the whole mission duration.

Outputs

webpage: `http://validate.globclim.org`

Technical Description

Used infrastructure	standard x64 Linux compute server, apache 2.2.9 webserver, PostgreSQL database version 9.4
Programming language	Python, Javascript
Current status	operational

3.2.13 pps-convert

Description

Conversion of the collocated RO reference profiles to a HDF5 file satisfying the EVDC format needed for submitting the files to the NILU Cal/Val database.

Inputs

- Collocated RO reference profiles selected by *pps-collocate* (cf. Subsection 3.2.5) and *pps-collocate-special-stations* (cf. Subsection 3.2.7).

Outputs

EVDC compliant HDF5 files.

Technical Description

Used infrastructure	standard x64 Linux compute server, PostgreSQL database version 9.4
Programming language	Python
Current status	operational

3.2.14 pps-submit-2-nilu

Description

Submission of the collocated RO reference profiles which have been converted to an EVDC compliant HDF5 file to the NILU atmospheric database.

Inputs

EVDC compliant HDF5 files

Outputs

None.

Technical Description

Used infrastructure	standard x64 Linux compute server, standard ftp client.
Programming language	Python
Current status	operational

4 Summary and Outlook

Summarizing the MMValRO system implementation, it can be said that the currently implemented final system (final one from the current MMValRO-E project) works well. That is, all basic modules are properly functioning, controlled by a job scheduler, and work in an automated manner.

Chapter 1 focused on the evaluation of the quality of RO data from different satellites. The newest Wegener Center data version OPSv5.6[1] was evaluated, which was subsequently used as reference data for the MIPAS, GOMOS, and RAOB validation. The chapter gave a short overview on the occultation database at WEGC[2] and then discussed in more detail the data quality of the diverse atmospheric profiles obtained by this technique. In addition, the temporal evolution of the data quality over the years as well as a consistency evaluation were discussed. It turns out that RO data are an unique data source with an amazing consistency of generally better than 0.1 K in temperature and also very low errors in general (i.e., overall systematic temperature errors generally smaller than 0.3 K). RO provides thus an excellent reference dataset for validating the data of other observing systems like MIPAS and GOMOS on ENVISAT regarding temperature, pressure, density, and to some degree (in the troposphere) also humidity.

Chapter 2 gave a description of the validation results from the project. The newest available ESA multi-year dataset (full ENVISAT period 2002 to 2012) of MIPAS (ML2PPv7.03[3]) and GOMOS (GOMOSv6.01) has been validated against the WEGC OPSv5.6 RO dataset. In addition, a high-quality RAOB dataset (Vaisala RS 80/90/92/41 RAOB profiles from ECMWF reanalysis archive) has been validated over 2002 to July 2016. The generated time series as well as the more detailed monthly profile evaluation plots available via `http://validate.globclim.org` show a fairly good agreement between the MIPAS and RO data products, in fact markedly further improved in the new ML2PPv7.03 data version compared to the previous MIPASv6.0 version evaluated in 2013 by Schwärz et al. [Sch+13]. For the GOMOS data no new version was available since the last validation (cf. [Sch+13]) run. The currently shown validation exhibit very similar results although more collocations could be found due to an increase of the number and quality of the new OPSv5.6.2[4] dataset. The validation of the high-quality RAOB data indicates very high consistency of

---

[1] Occultation Processing System version 5.6

[2] Wegener Center for Climate and Global Change

[3] ESA ML2PP processor version 7.03

[4] Occultation Processing System version 5.6.2

RAOB temperatures and RO temperatures over the full time period 2002 to 2016; also the tropospheric humidity agrees fairly well in the lower troposphere and a reasonably in the upper troposphere. Differences and changes in bias structures are part of ongoing studies. The website `http://validate.globclim.org` allows to conveniently explore the detailed results of all these validations.

Regarding specific issues and recommendations on the data quality of MIPAS (ML2PPv7.03) temperature and altitude profiles as well as of GOMOS (GOMOSv6.01) HRTP temperature and density profiles, we summarize the following from the present validation against RO based on monthly-mean data over the full ENVISAT period 2002 to 2012.

1. MIPAS ML2PPv7.03 temperature data:
   MIPAS temperatures in the UTLS[5] core region (over 10 km to 30 km) generally exhibit a standard deviation of only about 2 K throughout the period (except for northern hemisphere summer 2002 and October 2003 where it exceeds 3 K) and are generally accurate to within estimated RO uncertainty (90 % confidence interval) of <0.5 K during the time up to August 2006 (except for September 2004 showing a MIPAS systematic difference of −3 K). From September 2006 onwards the MIPAS systematic difference appears to be about −0.5 K to −0.9 K, i.e., still fairly small at <1 K but outside the estimated RO uncertainty. This apparent “regime shift” occurs during 2006 where the number of collocation pairs strongly increases, mainly from introduction of the COSMIC[6] constellation at the RO side. We therefore tested also the case of just continuing with CHAMP[7] RO collocations during CHAMP’s lifetime until September 2008—leaving the number of collocations essentially unchanged over 2006 to 2008—but the apparent “regime shift” of MIPAS systematic differences to about −0.5 K to −1 K remained so that RO is very likely not the main cause for the difference. This is supported by the intervalidation of the high-quality RAOBs and RO, where RAOB systematic differences are found essentially within RO uncertainty throughout all years, so that MIPAS data have an increased negative mean difference from 2006 onwards also against RAOB data.

   This hints to the fact that also ECMWF did some substantial assimilation and forecast system upgrades in 2006 (specifically in February 2006 and September 2006; regarding ECMWF model changes cf.ECMWF [ECM16]), which may have impacted the MIPAS processing from using ECMWF auxiliary information in some way; MIPAS systematic differences as function of altitude appear to show characteristic changes just by February 2006 and September 2006. As a general altitude dependence, the MIPAS accuracy is largely within RO uncertainty above about 17 km, while below a negative systematic difference of about −1 K occurs, especially since September 2006,

---

[5] Upper Troposphere–Lower Stratosphere

[6] Constellation Observing System for Meteorology, Ionosphere, and Climate

[7] Challenging Mini-Satellite Payload

which below about 10 km increases further to typically reach more than −5 K near the bottom of the UTLS at 5 km. The mean differences also include, on more detailed inspection, a visible annual (and partly semi-annual) cycle, of typically just roughly half a Kelvin magnitude, which nevertheless deserves further inspection and explanation.

The consistency of the MIPASv7.03 temperature dataset improved significantly against the previous version MIPASv6.0 due to the fact that the strong jump between the FR[8] and the OR[9] period was decreased or has vanished.

2. MIPAS ML2PPv7.03 altitude data:
   MIPAS altitudes in the UTLS core region (over 10 km to 30 km) generally exhibit a standard deviation of about 100 m to 200 m throughout the period (except for February, March, April, and June 2003 where it exceeded 300 m.

   The systematic difference in the core range is about 100 m to 150 m in the FR period and about 50 m in the OR period of the MIPAS instrument. Overall the MIPAS altitude quality before 2005 (from the FR period) is inferior to the one after 2005 (from the OR period).

   Compared to the MIPASv6.0 dataset the MIPASv7.03 dataset exhibits a clear increase in quality. The seasonal dependency of the bias has been removed and the absolute amount of the bias could be reduced to about 50 m, i.e., the usage of the ECMWF corrected altitudes was really worth doing.

3. GOMOSv6.01 temperature data:
   GOMOS temperatures in the GOMOS core region (over 20 km to 30 km) generally exhibit a standard deviation of only about 2 K to 3 K throughout the period (except a few months exceeds 4 K) and are generally accurate to within about 0.5 K to 1.5 K (except for a few months exceeding a sys.diff. of 2 K), which is mostly outside the estimated RO uncertainty (90 % confidence interval) of about 0.5 K.

   The most salient features of difference include a positive systematic difference of around 1 K for all years from 2006 onwards, while before (during the period of a significantly smaller number of collocations) there is somewhat more month-to-month variation but with the majority of the months exhibiting smaller mean differences of within 0 K to 1 K.

   Regarding altitude dependence of differences, the positive systematic deviations of GOMOS temperatures roughly occur between about 22 km to 32 km while above about 33 km (except before 2004) and below about 21 km negative systematic deviations become visible, which frequently exceed −1 K near 35 km and below about 20 km, respectively.

---

[8] Full Resolution Period

[9] Optimized Resolution Period

4. GOMOSv6.01 density data:
   GOMOS densities in the GOMOS core region (over 20 km to 30 km) generally exhibit a standard deviation of only about 2 % throughout the period (a few months only exceeding this) and are generally accurate to within about 1 % to 2 % (except for a few months exceeding a systematic difference of 2 % and only November 2009 exceeding 4 %), which is outside the estimated RO uncertainty (90 % confidence interval) of <0.5 %.

   The most salient features of difference include a negative systematic difference of within −1 % to −2 % for most of the months, whereby before 2006 (during the period of a significantly smaller number of collocations) there is not much multi-year trend in these monthly differences which cluster mostly within about −1 % to −1.5 %. From 2006 onwards there appears a multi-year positive trend in the differences over 2006 to 2008, from somewhat exceeding −2 % in early 2006 to reaching only about −1 % in fall 2008. After the GOMOS data gap in 2009 again a similar trend in the differences is visible (though with somewhat more month-to-month variation), from about −2 % in early 2010 to around −1 % in northern hemisphere summer 2011 and by the end of the ENVISAT mission in early 2012.

   Regarding altitude dependence of differences, the negative systematic deviations of GOMOS densities roughly occur between about 15 km to 30 km while above about 32 km postive systematic deviations become visible, which frequently exceed 3 % near 35 km. Below about 15 km the quality of the data clearly degrades and only a relatively small fraction of GOMOS profiles penetrates below this altitude; given the challenging scintillation conditions at these comparatively low altitudes for stellar occultation signals this behavior is fully in line with expectations.

It is recommended that the MIPAS and GOMOS data processing experts, respectively, look into the potential causes of the MIPAS–RO and GOMOS–RO differences as summarized above. It is recommended that these experts also consult for this purpose the website `http://validate.globclim.org` for detailed gegraphically and annually resolved results; this report only includes a small selected set of visualizations. We expect that this can help to inform and guide next steps of processing improvements for retrieval of the thermodynamic variables both for MIPAS and GOMOS, and indirectly therefore also help improvement of trace species retrievals.

We note that also on the RO side the data processing is currently undergoing a next step of advancement over 2016 to mid 2017, where the uncertainty estimation is again substantially improved by finishing the work to implement SI-traceability and uncertainty propagation from raw data to the derived thermodynamic profiles (cf.Section A.5). This shall serve to provide as of 2017 even more reliable RO reference data, with integrated uncertainty estimates, for future long-term validation activities.

Following the key chapter on the validation results, Chapter 3 described the structure and the process design of the MMValRO system PPS, which is part of the WOCAS. The PPS is performing all core tasks of the MMValRO project, in particular it handles the delivery of collocated RO data to the ESA ENVISAT Cal/Val centre at NILU (Kjeller, Norway) as well as the provision of validation results for MIPAS, GOMOS, and RAOB[10] data via the MMValRO website `http://validate.globclim.org` that was established by the project. As far as relevant for the MMValRO project, also issues of another part of WOCAS were addressed here, i.e., the issues of the operationalization of the OPS that delivers the input profiles for the PPS.

In Appendix A the RO method, being a leading remote sensing technique for the basic thermodynamic state of the atmosphere (temperature, pressure, density; and some humidity information in the troposphere) was explained. The RO method belongs to the active limb sounding techniques and utilizes signals transmitted by GNSS[11] satellites. On the way through the ionosphere and neutral atmosphere these signals are refracted and received on a LEO[12] satellite. Physical characteristics of the atmosphere between the transmitter and the receiver satellite and movements of the both satellites yield a Doppler shift of the electromagnetic signals, which is then inverted to atmospheric state variables, the basic one being atmospheric refractivity, from which subsequently the thermodynamic variables are derived.

For retrieving these atmospheric variables, the WEGC OPS was developed in partner projects of MMValRO; currently the WEGC OPSv5.6 retrieval is utilized. This latest processing system, which provided the RO data for the current validation, was therefore described here in more detail. The OPSv5.6 uses profiles of atmospheric excess phase and precise orbit information (position and velocity vectors of LEO and GPS[13] satellites) for generating atmospheric profiles of dry temperature, pressure, density, but also physical atmospheric parameters like physical temperature and pressure, and specific humidity.

Following a special request of ESA/ESRIN for complementary background information, an atlas of all collocation maps for the MIPAS, GOMOS, and RAOB collocations with RO are presented at the website `http://validate.globclim.org`. Collocations for all months for the whole study period are visualized on global geographic maps for all three validation datasets, which gives a fair impression of how the collocation conditions, and the size of collocation ensembles obtained, varied over the years; most saliently, the collocation conditions significantly improved from 2006 onwards.

In this report we showed that the collocation/validation system PPS, and the RO data provision system OPS that feeds it, are now working very adequately in providing long-term collocation and validation results of considerable value over the full ENVISAT period;

---

[10] Radiosonde Observation

[11] Global Navigation Satellite System

[12] Low Earth Orbit

[13] Global Positioning System

results that are then conveniently presented via http://validate.globclim.org. The MMValRO system is thus prepared for continuing its operations for next steps of cal/val activities and it is flexible enough to be extended to further capabilities and to cope with further tasks planned to be implemented in MMValRO follow-on projects.

Acknowledgments. The authors thank A. Dehn, ESA Tech. Officer for MMValRO-E, S. Casadio, (ESA/ESRIN Frascati, Italy) for support and advice to this study and to the report finalization. They also thank L. Haimberger (Univ. of Vienna, Austria) and B. Biadeglgne (Bureau of Meteorol., Melbourne, Australia) for advice and assistance in understanding and preparing the RAOB dataset for integration into WEGC's WOCAS system. Access to the MIPAS and GOMOS datasets was provided by ESA/ESRIN, and access to the RAOB dataset and to analysis and forecast fields (supporting the RO processing and validation) by ECMWF Reading, UK. The work was funded by ESA under the MMValRO project (ESRIN/Contract No. 4000110769/14/I-AM).

A The Radio Occultation Method and the Wegener Center OPS

The RO[1] method is a state-of-the-art remote sensing technique used to probe the Earth's atmosphere. It has originally been developed in planetary sciences where it has been used to study atmospheres, e.g., from Mars, Venus, and Jupiter [Esh73; FE68].

Different studies showed that the RO technique offers independent, very precise, and accurate measurements of the UTLS[2] region (temperature error less than 1 K, [see e.g., Kur+97]). Data are characterized by a very high vertical resolution, are long-term stable, and available globally. Measurements of different satellites can be combined without the need of inter-calibration so that they can be used for global climate monitoring on a long time scale [Foe+11; Ste+11].

In 1995 the first proof-of-concept mission sensing the terrestrial atmosphere has been launched into Earth orbit. Data from this GPS/MET[3] mission [War+96] confirmed that RO data are of importance for operational meteorology, i.e., numerical weather prediction, [Kuo+00], climate monitoring [Ste+01], ionospheric research [Sch+99], and space weather science [Jak+02]. For a review on RO applications, see [Ant11].

A.1 Measurement Principle

The RO method belongs to the active limb sounding techniques. It utilizes artificial signals transmitted by GNSS[4] satellites. These radio signals penetrate the atmosphere, where they are affected by the Earth's atmospheric density field. On the way through the ionosphere and neutral atmosphere these signals are refracted and received on a LEO[5] satellite (see Figure A.1). Physical characteristics of the atmosphere between the transmitter and the receiver satellite and movements of the both satellites yield a frequency shift of the electromagnetic signal.

The measured quantity aboard the LEO satellite is the phase change between the intrinsically transmitted signal (replicated in the receiver) and the Doppler-shifted incoming signal

---

[1] Radio Occultation

[2] Upper Troposphere–Lower Stratosphere

[3] Global Positioning System/Meteorology

[4] Global Navigation Satellite System

[5] Low Earth Orbit

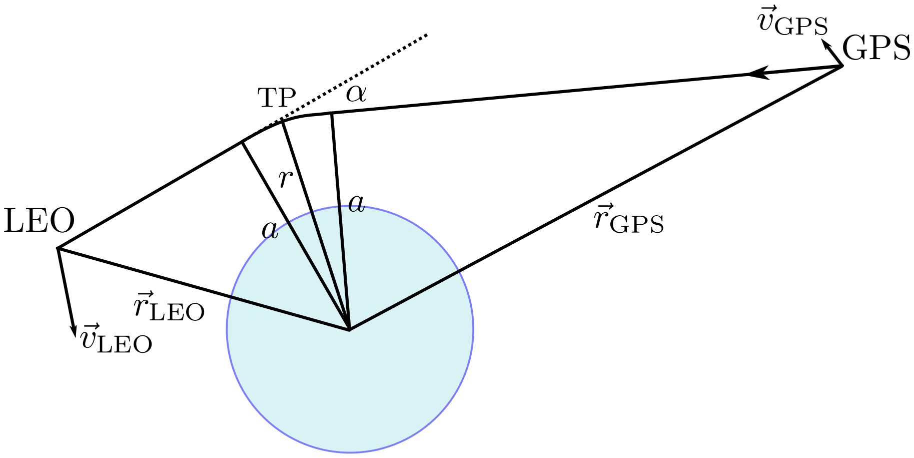

Figure A.1: Occultation geometry of a setting RO event. The signal, which is transmitted by a GPS satellite, is refracted by the ionosphere and neutral atmosphere before it is received at a LEO satellite. TP is the tangent point, r is the tangent radius, a the impact parameter (the perpendicular distance between either of the ray asymptotes and the center of refraction), α the bending angle, and $\vec{r}_{\text{LEO}}$ and $\vec{r}_{\text{GPS}}$ the position vectors of the LEO and the GPS satellite, respectively.

and the amplitude of this signal as a function of time. These measurements are performed on both GPS[6] frequencies, $f_1 = 1575.42\,\text{MHz}$ and $f_2 = 1227.60\,\text{MHz}$. The artifice of the RO retrieval is to extract the signal delay, which is caused by the neutral atmosphere (i.e., to correct all other proportions to phase delay), and to derive atmospheric characteristics by applying an inversion technique.

Due to the relative motion of the GPS and the LEO satellite, the radio signals (continuously broadcast by the GPS satellite) penetrate the atmosphere at different tangent heights and the atmosphere is scanned from top downwards (setting event) or from bottom up (rising event). This results in a near vertical profile of phase and amplitude measurements as a function of time. Within the upper troposphere, the lower stratosphere and above, the excess phase[7] relative to vacuum phase can be inverted to profiles of atmospheric parameters using simple principles of GO[8]. The performance of the RO retrieval in the lower troposphere is improved applying WO[9].

---

[6] Global Positioning System

[7] Excess phase is also called phase delay, atmospheric phase delay, excess phase delay, or excess phase path [Syn99].

[8] Geometrical Optics

[9] Wave Optics

A.2 The Global Positioning System and Excess Phase Delay

Each GPS satellite transmits right-handed circular polarized electromagnetic waves at two (carrier) frequencies, $f_1 = 1575.42\,\text{MHz}$ and $f_2 = 1227.60\,\text{MHz}$ ($\lambda_1 = 0.190\,\text{m}$, $\lambda_2 = 0.244\,\text{m}$) [HWLW08]. At these microwave wavelengths, the phase of an electromagnetic wave can be measured with a precision better than 0.01 cycles [HWLW08].

The measured phase pseudorange depends on the kinematic Doppler shift and on transmitter and receiver clock errors. However, pseudorange measurements are also affected by an ionosphere induced Doppler shift, a neutral atmosphere induced Doppler shift, and by diverse measuring inaccuracies like orbital errors or delays in electronic hardware.

The "conventional" GPS community, which is interested in time, position, and velocity of an object, favors the knowledge of the range due to kinematic Doppler shift and tries to correct the other parts. The RO community, however, tries to separate the phase change, which results from the neutral atmosphere only, to infer physical atmosphere characteristics.

After correction of receiver and transmitter clock errors, errors due to antenna phase center variations, multipath errors, relativistic effects, and cycle slips, the residual excess phase only contains contributions, which stem from the relative motion of the satellites (kinematic Doppler effect), from the ionosphere, and the neutral atmosphere. The separation of these phase changes follows later in the retrieval process.

A.3 Characteristics of Radio Occultation

The measurement principle itself, the use of microwave signals, and the specifications of the satellite orbits, which have been used for RO measurements so far, determine the characteristics of RO measurements and account for their potentials to be used for atmospheric sciences such as numerical weather prediction or climate monitoring [Ant11].

Self-calibration and long-term stability: The information used in the retrieval process is not the phase profile itself, but the excess phase relative to the phase measured above the atmosphere. For that reason, the single assumption to call the measurement "self-calibrating" is that the atmosphere has to be stable within the measurement time of one or two minutes. This self-calibrating characteristics also implies that the measurements are long-term stable and do not contain biases or drifts. This feature is particularly important for RO data to be used for climate monitoring purposes since data of different satellites can be combined without the need of inter-calibration [Foe+11; Ste+11].

Penetration of clouds and independence of sunlight: The frequency domain of GNSS signals enables measurements to be performed during virtually all weather conditions. This comes true because the signals are able to penetrate through most of the clouds

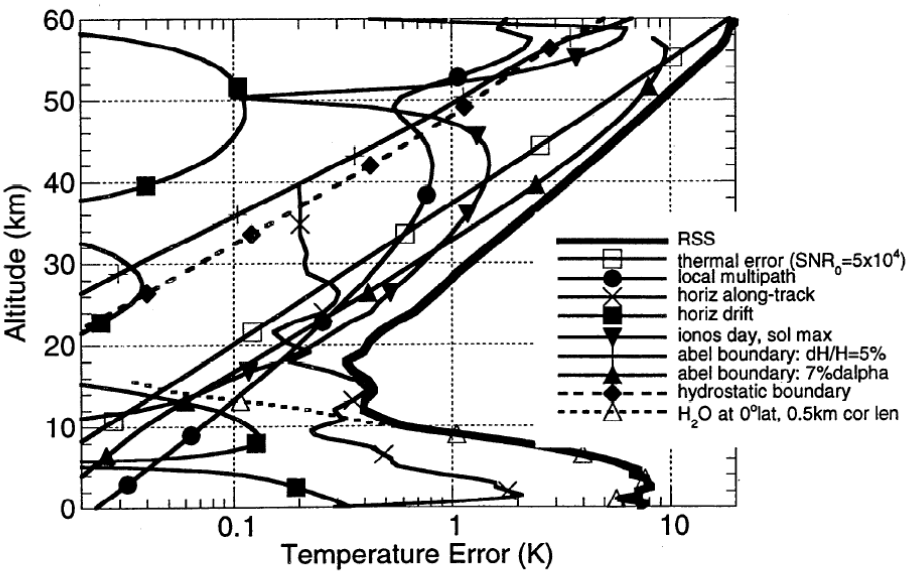

Figure A.2: Summary of dry temperature errors as a function of altitude. Largest errors are found under daytime, solar maximum ionosphere conditions. Temperature accuracies are found to be better than 1 K between 8 km and 30 km altitude (from Kursinski et al. [Kur+97]).

and the measurement, the excess phase, is not significantly degraded by clouds. In tropical regions, however, where atmospheric humidity is large, atmospheric multipath causes a severe degradation of the signal, which can only be handled by a WO retrieval. Furthermore, GPS signals are not affected by the presence or absence of sunlight so that measurements can be performed during day and night.

Accuracy: The accuracy of RO measurements depends on the instruments quality (e.g., thermal receiver noise), ionospheric and atmospheric conditions (e.g., residual ionospheric errors, water vapor ambiguity, or atmospheric multipath errors), accuracy of orbit determination, horizontal drift of the tangent point, and inversion procedures (e.g., initialization errors of the Abelian integral) [Kur+97]. Between 8 km and 30 km altitude, the temperature error is less than 1 K even in worst case scenarios (see Figure A.2). As discussed by Kursinski et al. [Kur+97], contributions from initialization errors of the Abelian integral, thermal noise, local multipath, and residual ionosphere limit the accuracy of temperature profiles at high altitudes. At low altitudes (especially at equatorial latitudes) the accuracy is limited by the uncertainty in water abundance.

Vertical and horizontal resolution: Limb sounding measurements are characterized by a high vertical but low horizontal resolution. The same holds true for RO measurements. The horizontal resolution amounts to about 300 km [Kur+97]. The GO vertical resolution is limited by the diameter of the first Fresnel zone, which decreases with height. It amounts to about 1.4 km in the stratosphere and about 0.5 km near the Earth's surface [Kur+97]. Using a WO retrieval, the vertical resolution can be as high as 60 m [Gor+04].

Global coverage: The orbit's inclination of GPS satellites is fixed at $i = 55°$. For that reason, the inclination of the LEO satellite determines the geographical coverage of RO measurements. The higher the inclination of the satellites' orbit, the higher the latitudes which can be reached by RO measurements. Until now, most RO measurements have been performed by nearly polar orbiting satellites (exception: C/NOFS[10] is a satellite in low inclination, $i = 13°$). Satellites with orbit inclinations of 72° and 800 km orbit altitude (F3C[11] orbit) are able to perform measurements at polar latitudes. So far, global coverage of RO events has been achieved by almost all RO missions.

Thus, GPS occultations offer independent, very precise, and accurate measurements of the UTLS region with a high vertical resolution. Measurements are available globally and are long-term stable and data, provided by different satellites, can be combined without the need of inter-calibration so that they can be used for global climate monitoring on a long time scale.

A.4 Occultation Processing System version 5.6—Derivation of Atmospheric Parameters from Excess Phase

At the WEGC[12], University of Graz, an RO retrieval scheme has been established, which uses excess phase and amplitude profiles and precise orbit information (level 1 data) provided by other data centers.

A.4.1 OPSv5.6 Input Data

In the UTLS, the WEGC OPSv5.6[13] retrieval is a GO retrieval, which uses profiles of excess phase obtained in PLL[14]-mode and precise orbit information (position and velocity vectors of LEO and GPS satellites) for generating GO bending angle profiles.

---

[10] Communications/Navigation Outage Forecasting System

[11] FORMOSAT-3/COSMIC

[12] Wegener Center for Climate and Global Change

[13] Occultation Processing System version 5.6

[14] Phase Locked Loop

Recent GPS receivers onboard F3C and TerraSAR-X[15] provide measurements received in PLL- and OL[16]-mode. While the last WEGC OPS[17] version (OPSv5.4[18]) was not able to handle excess phase data received in OL-mode, the OPSv5.6 retrieval is now able use these data. In the lower and middle troposphere, the WEGC OPSv5.6 retrieval is a WO retrieval, which uses profiles of excess phase and amplitude obtained in PLL- and OL-mode as well as precise orbit information. The OPSv5.6 retrieval output is a combined GO and WO bending angle profile.

Figure A.3 shows the minimal impact height of F3C/FM[19]-1 measurements recorded on September 5, 2007. Data, which have been obtained from the OPSv5.4 retrieval are derived only with PLL data, whereas the OPSv5.6 retrieval uses both, PLL and OL data. OPSv5.6 bending angles stop at approximately 2 km impact height, which corresponds to the Earth's surface. The lower limit of OPSv5.4 bending angles varies between 8 km for F3C setting occultation events and 12 km impact height for F3C rising occultation measurements. This clearly indicates the improvement of the OPSv5.6 relative to OPSv5.4.

All OPSv5.6 input data are provided by UCAR[20]/CDAAC[21] but OPSv5.6 can also handle EUMETSAT[22] MetOp[23] satellite data and data provided by GFZ[24].

A.4.2 Occultation Geometry

Knowledge of space vectors of the LEO and the GPS satellites allows the determination of the occultation geometry, e.g., the mean tangent point location or the distance of the mean occultation event to the LEO or to the GPS satellite.

Within the OPS retrieval, the location of the mean tangent point of an occultation event is defined as that point, where the straight line between the LEO and the GPS satellite is tangent to the Earth's surface. That straight line corresponds to a bent ray at an altitude of about 10 km to 15 km.

At mean occultation event location, co-located profiles of other data sets are extracted to be used as background information within the retrieval and for validation purpose after the retrieval.

---

[15] Terra Synthetic Aperture Radar

[16] Open Loop

[17] Occultation Processing System

[18] Occultation Processing System version 5.4

[20] University Corporation for Atmospheric Research

[21] COSMIC Data Analysis and Archive Center

[22] European Organization for the Exploitation of Meteorological Satellites

[23] Meteorological Operational

[24] German Research Centre for Geosciences

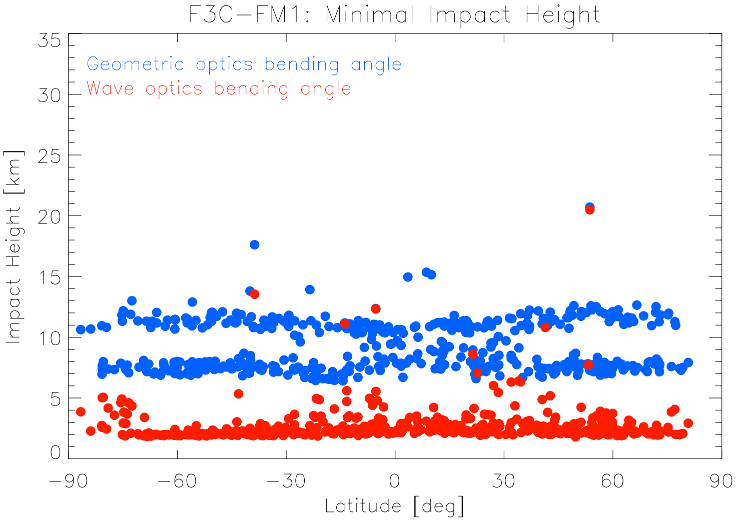

Figure A.3: Minimal impact height of bending angle profiles. Data stem from one day of F3C/FM-1 data (September 5, 2007). OPSv5.4 GO bending angles (which only use excess phase data received in PLL-mode, blue dots) are compared to OPSv5.6 bending angles (which also utilizes OL input data, red dots). OPSv5.6 WO bending angles stop at approximately 2 km impact height, which corresponds to the Earth's surface.

A.4.3 Data Preparation

Some plausibility checks and corrections are applied to the input data before entering in the retrieval. Outliers of excess phase profiles are removed separately for the L1[25]- and the L2[26]-signal. This is done by calculating the mean and standard deviation of the data recorded within one second (50 data points because sampling rate is 50 Hz). If the point in the middle of the second deviates by more than three standard deviations from the interval's mean, it is replaced by the intervals mean. L1- and L2-phases are smoothed using a regularization method [FH99; Syn99]. It aims at removing high frequency noise, which is necessary to avoid non-physical data and non-physical oscillations in the retrieved data products.

A.4.4 Correction of the Earth's Oblateness

Meteorological parameters are not exactly spherically distributed around the globe. The Earth's gravitational field yields contours of constant values of atmospheric parameters to follow the shape of the geoid. The geoid approximates to an ellipsoid and the oblateness of

---

[25] L band signal no. 1 transmitted by GPS satellites (centered at 1.57542 GHz)

[26] L band signal no. 2 transmitted by GPS satellites (centered at 1.22760 GHz)

the ellipsoid has to be accounted for in the retrieval process to first order because spherical symmetry is assumed in the retrieval process and neglecting the Earth's oblateness causes a temperature bias of up to 3 K at an altitude of 10 km and about 6 K at the ground [Syn98]. Spherical symmetry is assumed in the retrieval of bending angle so that all satellite positions have to be referred to the local center of refraction instead of the Earth's center. The center of refraction is defined by the origin of a sphere, which is tangential to the ellipsoid at the mean occultation event location. The OPSv5.6 retrieval applies the correction procedure proposed by Syndergaard [Syn98].

A.4.5 Bending Angle Retrieval

The bending angle retrieval is one main part in the RO processing chain. Excess phase profiles are used to calculate atmospheric Doppler profiles, from which raw bending angle profiles are derived. Ionosphere-corrected bending angle profiles are statistically optimized using background information. Using a Gaussian transition, GO bending angles are merged with WO bending angles.

This section focuses on the GO bending angle retrieval. For more information on the WO bending angle retrieval used in the OPSv5.6, we refer to Gorbunov [Gor02] and Gorbunov et al. [Gor+04].

Excess Doppler and Doppler Shift

The excess Doppler of L1 and L2, $\mathrm{d}L_i/\mathrm{d}t$, is derived by differentiating the excess phase. Within the OPSv5.6 retrieval a 3-point differentiation formula is used.

The atmospheric Doppler shift Δf_i is the negative excess Doppler scaled by the frequency f_i and the speed of light c

$$\Delta f_i = -\frac{f_i}{c}\frac{\mathrm{d}L_i}{\mathrm{d}t}. \tag{A.1}$$

Bending Angle

Knowledge of excess Doppler and occultation geometry (space and velocity vectors of both, GPS and LEO satellites) enables the calculation of atmospheric GO bending angle α as a function of impact parameter a. The only assumption is local spherical symmetry, which is valid after correcting the Earth's oblateness (cf. Subsection A.4.4). The determination of GO bending angle is done separately for each frequency.

Ionospheric Correction

The input data used for the OPSv5.6 retrieval, the atmospheric excess phase, does not only include neutral atmospheric excess phase, but also ionospheric excess phase. Because the neutral atmosphere characteristics are of our main interest, the ionospheric influence on the atmospheric excess phase has to be removed.

The OPSv5.6 retrieval applies an ionospheric correction where low-pass filtered GO bending angle profiles, $\overline{\alpha}_1$ and $\overline{\alpha}_2$, are linearly combined but the high-pass fraction of the L1 GO bending angle, $\delta\alpha_1(a) = \alpha_1(a) - \overline{\alpha}_1(a)$, which actually accounts for small-scale features appearing in the neutral atmosphere, is added again [HIT03]:

$$\alpha_c(a) = \frac{f_1^2\overline{\alpha}_1(a) - f_2^2\overline{\alpha}_2(a)}{f_1^2 - f_2^2} + \delta\alpha_1(a). \tag{A.2}$$

Bending Angle Bias, Noise, and Observational Error

The GO bending angle bias and noise are estimated by comparing the ionosphere-corrected GO bending angle profile to its co-located MSIS[27] [Hed91] profile between 65 km and 80 km. At these height levels, the measurement is dominated by measurement noise and ionospheric residuals because atmospheric density is small.

The bias[28] is found as the difference between the mean GO bending angle and the mean MSIS bending angle within that altitude range.

The GO bending angle noise is defined as the standard deviation of the RO profile relative to the shifted MSIS profile (shifted by the bias).

The characteristic of the observational data noise (i.e., the observational error) is needed for statistical optimization of GO bending angle at high altitudes as it determines the weight of the measurement (see Section A.4.5).

Experience with CHAMP[29] data showed that the GO bending angle noise often does not reflect the real quality of the measurement [Gob05] so that, in some cases, the observational error is not equal to GO bending angle noise but is modified according to some additional quality checks.

The most important quality checks comprise:

1. After the ionospheric correction, the GO bending angles at high altitudes are sometimes smaller than zero because of superimposed noise. However, the atmospheric density field yields signals bending and atmospheric bending angle should not be negative below 65 km. If negative GO bending angles occur below 65 km, the observational error is set to $10\,\mu\text{rad}/\sqrt{5}$. Negative GO bending angles are removed and the top of the profile is cut off.

---

[27] Mass Spectrometer and Incoherent Scatter Radar (model)

[28] The term "bias" may be confusing because both, the RO and the MSIS bending angle exhibit a bias relative to the truth.

[29] Challenging Mini-Satellite Payload

2. If negative GO bending angles occur below 55 km, the observational error is set to $50\,\mu\mathrm{rad}/\sqrt{5}$. Negative GO bending angles are removed and the top of the profile is cut off and the QF[30] is set to a non-zero value (QF = 2).

3. If negative GO bending angles occur below 50 km, the profile is discarded, the QF is set to a non-zero value (QF = 5).

This (conservative) approach, which proved to be useful for comparatively noisy CHAMP data, leads to stronger weighting of the bending angle background when performing statistical optimization.

High Altitude Initialization and Statistical Optimization

In the next "main" step of the retrieval, the calculation of microwave refractivity is performed by an Abel transformation, which involves an integral (cf. Subsection A.4.6). The upper bound of this integral is infinity. Since RO data are usually available only up to 80 km, the Abel integral needs an upper boundary initialization. A bad initialization of the bending angle at highest altitudes (in the lower thermosphere) results in errors in the refractivity profile. Furthermore, bending angles at high altitudes (upper stratosphere and beyond) are characterized by high noise, which also results in non-negligible errors in the refractivity profile.

The retrieved GO bending angle profile is optimized in a statistically optimal way [Rod00] yielding a "statistically optimized bending angle", which is used for further calculations. The OPS retrieval uses co-located ECMWF[31] short-range forecast profiles for statistical optimization since these data are believed to be the best-possible data set available. However, therefore RO data retrieved at WEGC are not fully independent from ECMWF at high altitudes, since as noise of RO data becomes high ECMWF data receive relatively more weight. Practically up to about 35 km to 40 km altitude RO information generally dominates the retrieval.

The optimization is performed between 30 km and 120 km impact height. The method used is an inverse covariance weighting technique, where unbiased (Gaussian) errors and a linear problem are assumed [GK04].

Merge of GO and WO bending angles

GO and WO bending angles are merged applying a half Gaussian transition between 7 km (or the bottom GO/WO impact height) and 13 km with a Gaussian half width of 1.5 km.

No merge is performed if (i) the GO bending angle reaches further down than the WO bending angle, (ii) the WO bending angle does not reach below 7 km, or (iii) the GO

---

[30] Quality Flag

[31] European Centre for Medium-Range Weather Forecasts

bending angle does not reach below 13 km. If one of these conditions applies, the OPSv5.6 final bending angle output only contains the GO bending angle.

A.4.6 Atmospheric Refractivity

Bending of a ray is caused by radial variations of the refractive index n. The inversion of an Abel integral equation (the corresponding derivation is shown e.g., by Steiner [Ste98]) yields

$$n(r_1) = \exp\left[-\frac{1}{\pi}\int\limits_{a_1}^{\infty}\frac{\alpha(a)}{\sqrt{a^2 - a_1^2}}\mathrm{d}a\right], \tag{A.3}$$

where a_1 is the impact parameter for a particular ray and $r_1 = r_\mathrm{t}$ is the radius of the corresponding tangent point, $a_1 = n(r_1)r_1$.

Since the refractive index is close to unity in the free atmosphere and refractive index variations are very small, the atmospheric community prefers using atmospheric refractivity N rather than the refractive index n. It is defined by

$$N(h) = (n(h) - 1) \cdot 10^6, \tag{A.4}$$

with

$$h = r - r_\mathrm{c} = \frac{a}{n(a)} - r_\mathrm{c}, \tag{A.5}$$

where h is the height above Earth's ellipsoid and r_c is the radius of curvature of the ellipsoidal Earth at the location of the occultation event.

After calculation of atmospheric refractivity as a function of height, the profile is smoothed by a Blackman-window filter (<1 km filter width) to eliminate numerical noise without degrading the resolution (∼1 km).

Figure A.4 depicts an RO refractivity profile (derived from a CHAMP setting event, which has been recorded end of September 2007 at high southern latitudes) and the corresponding co-located ECMWF refractivity profile (extracted from an ECMWF analysis field) in linear space (left panel) and in logarithmic space (middle panel) as a function of MSL altitude. The right panel shows the systematic difference between CHAMP and ECMWF refractivity, given in percent. The wavelike variability structures seen in this difference contain geophysical information (atmospheric wave variability such as from internal gravity waves). Such smaller-scale structures are captured by RO data due to their higher vertical resolution compared to ECMWF data (the latter have gravity waves filtered out for the sake of numerical stability of the weather prediction and analysis fields).

A.4.7 Retrieval of Dry Atmospheric Parameters

Atmospheric refractivity at microwave wavelengths as derived from GPS signals depends on conditions of the dry atmosphere, the moist atmosphere, the ionosphere, and on atmospheric

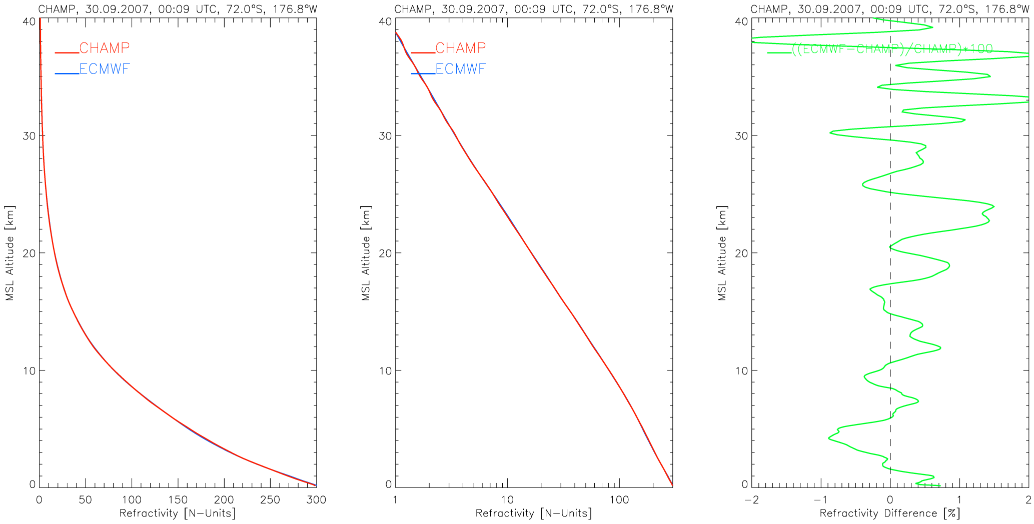

Figure A.4: RO and ECMWF refractivity profiles (left: in linear scale, middle: in logarithmic scale) as a function of MSL altitude. Their systematic difference, given in percent, is depicted in the right panel.

scattering from liquid water or ice crystals. To first order this relationship is given by [Kur+97; SW53]

$$N = c_1 \frac{p}{T} + c_2 \frac{e}{T^2} + c_3 \frac{n_e}{f^2} + c_4 W, \tag{A.6}$$

where p is the atmospheric pressure (in hPa), T atmospheric temperature (in K), e partial pressure of water vapor (in hPa), n_e is the electron density (in electrons m^{-3}), f the transmitter frequency (in Hz), and W is the mass density of condensed water in the atmosphere (in $\mathrm{g\,m^{-3}}$). The constants are $c_1 = 77.6\,\mathrm{K\,hPa^{-1}}$, $c_2 = 3.73 \times 10^5\ \mathrm{K^2\,hPa^{-1}}$, $c_3 = -4.03 \times 10^7\ \mathrm{Hz^2\,m^3}$, and $c_4 = 1.4\,\mathrm{m^3\,g^{-1}}$.

The first and the second term of Eq. (A.6) remain important in further considerations. The neglect of moisture yields dry atmospheric parameters, e.g., “dry temperature”. Physical atmospheric parameters and humidity profiles can only be simultaneously derived using auxiliary information obtained from independent data sets.

Derivation of Dry Density

In atmospheric regions where moisture is negligible, which holds true for altitudes above 8 km (polar winter) and 14 km (tropics) [Foe+08; SP+11b], refractivity at microwave wavelengths

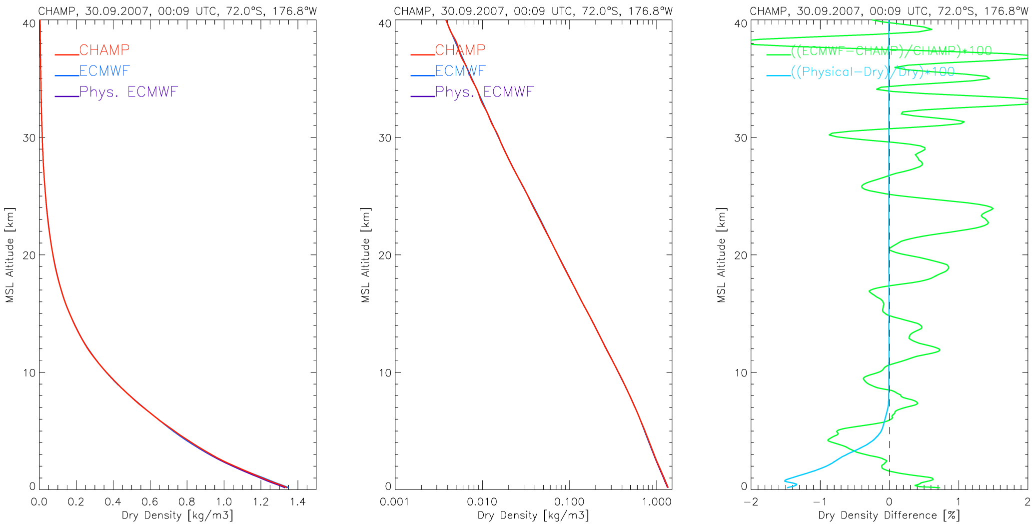

Figure A.5: RO and ECMWF dry density and ECMWF physical density profiles (left: in linear space, middle: in logarithmic space) as a function of MSL altitude. The systematic difference between RO and ECMWF dry density as well as between ECMWF physical and dry density, both given in percent, are depicted in the right panel.

mainly depends on the density of dry air:

$$N_{\text{dry}} = c_1 \frac{p_{\text{dry}}}{T_{\text{dry}}} = c_1 \rho_{\text{dry}} \frac{R}{\overline{M}}, \tag{A.7}$$

where $R = 8.3145\,\mathrm{J/(K\,mol)}$ is the universal gas constant [MTN08] and $\overline{M} = 28.964\,\mathrm{kg\,kmol^{-1}}$ is the mean molar mass of dry air [KLH07].

The profile of air density as a function of height can therefore be directly derived from the refractivity profile by

$$\rho_{\text{dry}}(h) = N_{\text{dry}}(h) \frac{\overline{M}}{c_1 R}. \tag{A.8}$$

The CHAMP dry density profile as a function of MSL altitude is shown in Figure A.5 in linear space (left panel) and in logarithmic space (middle panel). The logarithmic behavior of refractivity is propagated also in the dry density profile. Since refractivity is directly proportional to dry density (see Eq. (A.8)), the dry density relative difference profile between CHAMP and ECMWF (right panel of Figure A.5) is the same as the refractivity relative difference profile (Figure A.4).

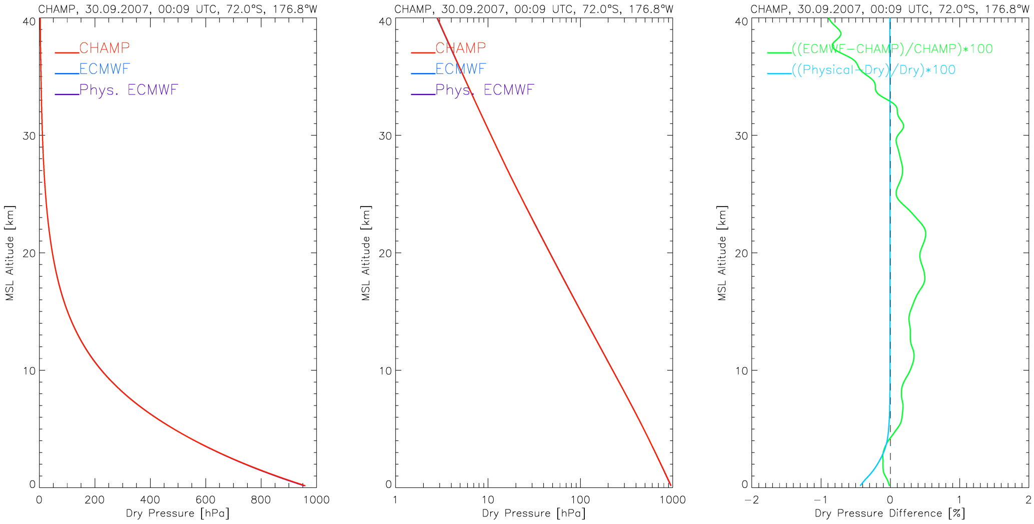

Figure A.6: RO and ECMWF dry pressure and ECMWF physical pressure profiles (left: in linear space, middle: in logarithmic space) as a function of MSL altitude. The systematic difference between RO and ECMWF dry pressure as well as between ECMWF physical and dry pressure, both given in percent, are depicted in the right panel.

Derivation of Dry Pressure

Under the assumption of hydrostatic equilibrium, the atmospheric pressure equals the weight of the overlying air column per area. This relationship is specified by the hydrostatic integral, which is the integral of acceleration of gravity as a function of geographic latitude and height $g(\phi, h)$ times density $\rho_{\text{dry}}(h)$ yielding atmospheric pressure:

$$p_{\text{dry}}(h) = \int_{h}^{\infty} g(\phi, h')\rho_{\text{dry}}(h')\mathrm{d}h' \tag{A.9}$$

The upper bound of the integral, which is theoretically infinity, is set to 120 km.

Figure A.6 shows the RO and ECMWF dry pressure profiles as well as the ECMWF physical pressure profile as a function of MSL altitude (again in linear and in logarithmic space, left and middle panel).

The systematic difference between RO and ECMWF dry pressure (green line in the right panel of Figure A.6) increases from the surface to approximately 22 km, where it yields its maximum value of approximately 0.6 %. It becomes smaller above about 22 km, above about 33 km it even becomes negative. This southern high latitude profile reveals the difference between physical and dry pressure (shown in light blue) being negligible above about 6 km

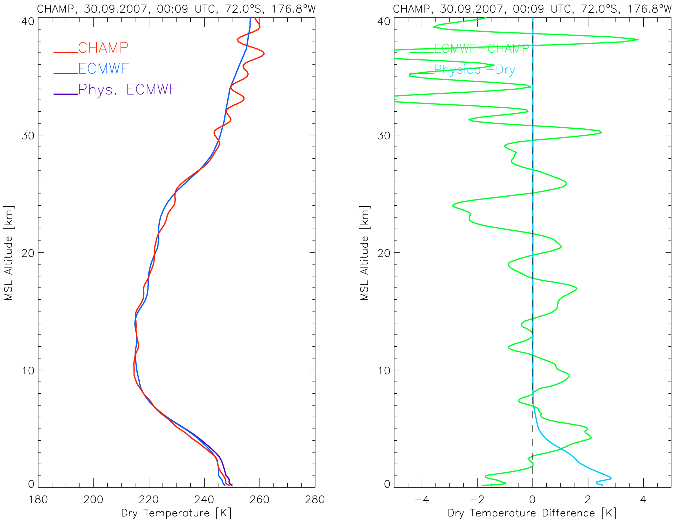

Figure A.7: RO and ECMWF dry temperature and ECMWF physical temperature profiles as a function of MSL altitude (left). The systematic difference between RO and ECMWF dry temperature as well as between ECMWF physical and dry temperature are depicted in the right panel.

altitude where the water vapor content is small. Below 6 km altitude, however, water vapor partial pressure yields physical pressure being smaller than dry pressure. Therefore, the difference (physical minus dry pressure) is negative.

Derivation of Dry Temperature

Dry temperature is obtained by utilizing the ideal gas law:

$$T_{\mathrm{dry}}(h) = \frac{\overline{M}}{R}\frac{p_{\mathrm{dry}}(h)}{\rho_{\mathrm{dry}}(h)}. \tag{A.10}$$

The temperature profile is finally smoothed by a Blackman-window filter (<1 km filter width) to eliminate numerical noise without degrading the resolution (∼1 km).

Vertical profiles of RO and ECMWF dry temperature and ECMWF physical temperature are depicted in Figure A.7. Temperature does not decrease exponentially with height. It decreases from the Earth's surface to the tropopause (here at approximately 9 km), where minimal temperatures are recorded. In the stratosphere, however, the availability of ozone assures an increase of atmospheric temperature. The (small) systematic difference between the RO and the co-located ECMWF dry temperature profile is predominantly positive in the upper troposphere and lower stratosphere up to about 21 km and predominantly negative above. The difference between physical and dry temperature remains smaller than 3 K under these cold and dry high-latitude conditions. However, in the tropical lower troposphere such differences can exceed 30 K.

Derivation of Geopotential Height on Dry Pressure Levels

The geopotential height can be calculated at all altitude levels from

$$Z(h) = \frac{1}{g_{45}} \int_{0}^{h} g(\phi, h')\mathrm{d}h', \tag{A.11}$$

where $g_{45} = 9.806\,65\,\mathrm{m\,s^{-2}}$ is the mean acceleration of gravity at sea level at $\phi = 45°$ [NIS01].

Geopotential height can then be interpolated to standard dry pressure altitude levels (termed "(dry) pressure altitude"), defined by

$$\text{dry pressure altitude} = -H_0 \ln\left(\frac{p_{\mathrm{dry}}}{p_0}\right), \tag{A.12}$$

where $H_0 = 7\,\mathrm{km}$ is the mean atmospheric scale height, p_{dry} is atmospheric dry pressure (in hPa), and $p_0 = 1013.25\,\mathrm{hPa}$ is the standard surface pressure. This interpolation can be done based on first converting the dry pressure values at the altitude levels to dry pressure altitude values and then interpolating the geopotential height profile from this dry pressure altitude grid to a standardized dry pressure altitude grid (e.g., with equidistant 100 m vertical spacing).

Geopotential height as a function of pressure altitude and the systematic difference between the RO and ECMWF profile is shown in Figure A.8. There is a nearly linear relationship between geopotential height and pressure altitude. The systematic difference between the RO and the ECMWF profile shows that ECMWF geopotential height is somewhat higher than RO geopotential height up to approximately 35 km and somewhat lower above.

A.4.8 Retrieval of Moist Atmospheric Parameters

Atmospheric profiles of physical temperature, physical pressure, and humidity (moist atmospheric quantities) can be retrieved applying a 1D-Var[32] retrieval. As a general principle, it utilizes the measured refractivity or bending angle profile y_{obs}, the a priori knowledge of the state of the atmosphere (i.e., a background profile) x_{bg}, and their associated errors (i.e., observation and background covariance matrices, **O** and **B**, respectively). The 1D-Var minimizes a quadratic cost function J [GRA09]

$$J(x) = \frac{1}{2}\left(x - x_{\mathrm{bg}}\right)^{\mathrm{T}} \mathbf{B}^{-1} \left(x - x_{\mathrm{bg}}\right) + \frac{1}{2}\left(y_{\mathrm{obs}} - \mathbf{H}[x]\right)^{\mathrm{T}} \mathbf{O}^{-1} \left(y_{\mathrm{obs}} - \mathbf{H}[x]\right) \tag{A.13}$$

---

[32] 1-Dimensional Variational Data Assimilation

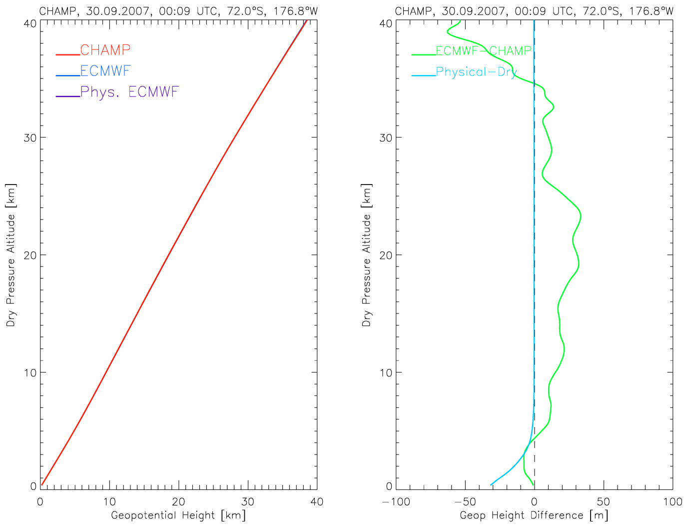

Figure A.8: RO and ECMWF geopotential height profiles as a function of dry pressure altitude (left) and their systematic difference (right), which reflects the relative pressure differences as seen in the right panel of Figure A.6.

to retrieve the physical atmospheric state x. $\mathbf{H}[x]$ is the forward modeled observation.

We use co-located ECMWF short-term forecast profiles as background data (24 h or 30 h forecast fields). This keeps independence from the ECMWF analysis, which on its own contains as of December 2006 RO information from data assimilation.

The implementation in the OPSv5.6 system is a carefully simplified version of 1D-Var which is summarized below. The moist air retrieval is an algorithm to retrieve temperature T and/or specific humidity q, as well as water vapor volume mixing ratio V_w, water vapor pressure e, pressure p, and density ρ, from dry pressure p_dry, dry temperature T_dry, and pre-scribed background temperature T_bg and/or background specific humidity q_bg. Also error estimation for the retrieved temperature and humidity is included, based on the input errors of the retrieved dry temperature profile T_dry, the background temperature profile T_bg, and the background humidity profile q_bg (the dominating error sources in the retrieval). We provide an overview description here; a detailed description is found in [Kir+13].

Moist Air Retrieval Algorithm Description

The fundamental dry air refractivity relation

$$N = c_1 R_\mathrm{d} \rho_\mathrm{dry} = c_1 \cdot \frac{p_\mathrm{dry}}{T_\mathrm{dry}}, \tag{A.14}$$

embodies the dry air equation of state $p_{\text{dry}}/\rho_{\text{dry}} = R_{\text{d}} T_{\text{dry}}$, with $R_{\text{d}} = R/\overline{M}$ being the specific gas constant of dry air. Eq. (A.14) allows to formulate the ratio of dry pressure p_{dry} and dry temperature T_{dry} in terms of generic refractivity,

$$c_1 \frac{p_{\text{dry}}}{T_{\text{dry}}} = N\left(T, V_{\text{w}}, p\right). \tag{A.15}$$

The water vapor volume mixing ratio V_{w} relates to water vapor pressure e, pressure p, and specific humidity q as,

$$V_{\text{w}} = \frac{q}{a_{\text{w}} + b_{\text{w}} q}, \tag{A.16}$$

$$q = \frac{a_{\text{w}} V_{\text{w}}}{1 + b_{\text{w}} V_{\text{w}}}, \tag{A.17}$$

where $a_{\text{w}} = \overline{M}_{\text{w}}/\overline{M} = 0.6220$ and $b_{\text{w}} = 1 - \overline{M}_{\text{w}}/\overline{M} = 0.3780$ are constants with $\overline{M}_{\text{w}}$ being the molar mass of water $M_{\text{w}} = 18.0153\,\text{kg}\,\text{kmol}^{-1}$. The R.H.S. of Eq. (A.15) denotes in principle any existing type of refractivity relation (from Smith-Weintraub-type [SW53] to Thayer-type [Tha74]; see also [Foe99; Hea09]).

Applying the Smith-Weintraub formula,

$$N = c_1 \frac{p}{T} + c_2 \frac{e}{T^2}, \tag{A.18}$$

the R.H.S. of Eq. (A.15), N, can be written as

$$N\left(T, V_{\text{w}}, p\right) = N = c_1 \frac{p}{T} \left(1 + \frac{c_{\text{T}}}{T} V_{\text{w}}\right), \tag{A.19}$$

where $c_{\text{T}} = c_2/c_1$. We get the three mutually equivalent forms

$$T = T_{\text{dry}} \frac{p}{p_{\text{dry}}} \left(1 + \frac{c_{\text{T}}}{T} V_{\text{w}}\right), \tag{A.20}$$

$$V_{\text{w}} = \frac{\frac{p_{\text{dry}}}{p} T - T_{\text{dry}}}{\frac{c_{\text{T}}}{T} T_{\text{dry}}}, \tag{A.21}$$

$$p = p_{\text{dry}} \frac{T}{T_{\text{dry}} \left(1 + \frac{c_{\text{T}}}{T} V_{\text{w}}\right)}. \tag{A.22}$$

Invoking as complementary fundamental relations the dry air and moist air hydrostatic equations in differential form for dry pressure p_{dry} and pressure p, respectively, and rationing them to express the moist pressure vertical increment $\mathrm{d}\ln p$ in terms of the dry pressure increment, yields

$$\frac{\mathrm{d}\ln p}{\mathrm{d}\ln p_{\text{dry}}} = \frac{R_{\text{d}} T_{\text{dry}}}{R_{\text{d}} T (1 + c_{\text{w}} q)} \tag{A.23}$$

and

$$\mathrm{d}\ln p = \mathrm{d}\ln p_{\mathrm{dry}} \frac{T_{\mathrm{dry}}}{T(1 + c_{\mathrm{w}} q)}.$$

Using Eq. (A.16) to convert q to V_{w},

$$1 + c_{\mathrm{w}} q = 1 + \frac{b_{\mathrm{w}} V_{\mathrm{w}}}{1 + b_{\mathrm{w}} V_{\mathrm{w}}} = \frac{1 + 2b_{\mathrm{w}} V_{\mathrm{w}}}{1 + b_{\mathrm{w}} V_{\mathrm{w}}} \tag{A.24}$$

we get

$$\mathrm{d}\ln p = \frac{T_{\mathrm{dry}}\,(1 + b_{\mathrm{w}} V_{\mathrm{w}})}{T\,(1 + 2b_{\mathrm{w}} V_{\mathrm{w}})} \mathrm{d}\ln p_{\mathrm{dry}}. \tag{A.25}$$

Based on these general expressions we can now either solve for T and p if q (and thus via Eq. (A.16) V_{w}) is prescribed or for V_{w} (and via Eq. (A.17) q) and p if T is prescribed. This works by a simple iteration at any arbitrary altitude level where a suitably adjacent level has been solved for p before,

1. if q and therefore also V_{w} is prescribed, we iterate the pair of Eqs. (A.20) and (A.25) until T has converged to within a tolerance (also p is automatically consistent with this converged T),

2. if T is prescribed, we iterate the pair of equations (A.21) and (A.25) until V_{w} has converged to within a tolerance (again p will be consistent with the converged V_{w}).

For the initial values for T, p, and V_{w} at start of iterations we use $T_0 = T_{\mathrm{dry}}$, $V_{\mathrm{w0}} = q_{\mathrm{minE}}/a_{\mathrm{w}}$ ($q_{\mathrm{minE}} = 1.5\dot{1}0^{-6}\ \mathrm{g\,kg^{-1}}$), and $p_0 = p_{\mathrm{dry}}$ for the initial level, and $T_{i,0} = T_{i-1}$, $V_{wi,0} = V_{wi-1}$, and $p_{i,0} = p_{i-1} \cdot (1 + |z_i - z_{i-1}|/H_0)$ for successive MSL altitude levels z_i from top downwards.

The retrieval of T, V_{w}, p, and q at all altitude levels as described provides the core algorithmic basis of the new moist air retrieval. Based on combining the results from V_{w} prescribed and T prescribed in an optimal estimation sense (inverse-variance weighting of retrieved and background profiles), optimally estimated T and q profiles are finally obtained, based on which also consistent values of V_{w} (via Eq. (A.16)) and p (via Eq. (A.22)) are computed.

The profiles e and ρ are then derived from V_{w}, p, T, and q. The water vapor partial pressure profile e is computed as

$$e = V_{\mathrm{w}} p, \tag{A.26}$$

and the density profile ρ via the equation of state in moist air as

$$\rho = \frac{p}{R_{\mathrm{d}} T (1 + c_{\mathrm{w}} q)}. \tag{A.27}$$

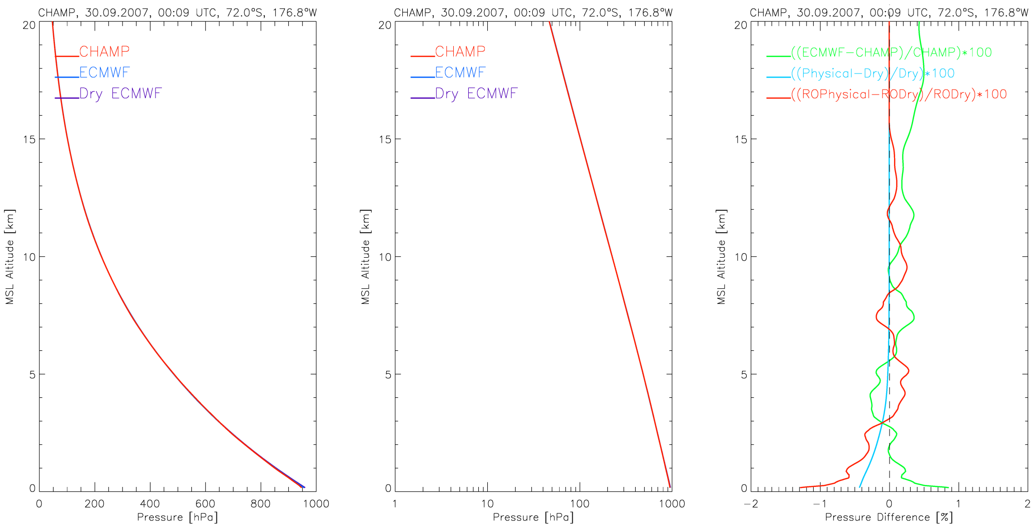

Figure A.9: RO and ECMWF physical pressure and ECMWF dry pressure profiles (left: in linear space, middle: in logarithmic space) as a function of MSL altitude. The systematic difference between RO and ECMWF physical pressure as well as between ECMWF physical and dry pressure and between RO physical and dry pressure, all given in percent, are depicted in the right panel.

Geopotential height Z can be interpolated to standard pressure altitude levels (“pressure altitude”), analogous to Eq. (A.12) in Subsection A.4.7.

Figure A.9, Figure A.10, and Figure A.11 show vertical profiles of physical pressure, temperature, and specific humidity of CHAMP and ECMWF as well as their differences.

A.4.9 Quality Control

Quality checks are performed on a regular basis during the retrieval chain. Quality checks, which comprise technical aspects and data consistency, are called “internal” quality checks. Most of them are performed in the bending angle retrieval.

“External” quality checks are applied to the retrieval results (refractivity, dry temperature, and physical temperature profiles) where retrieved profiles are compared to co-located profiles extracted from ECMWF analysis fields. RO refractivity profiles are compared to co-located ECMWF refractivity profiles between 5 km and 35 km. RO profiles, which differ from co-located ECMWF profiles by more than 10 % (maximum allowed refractivity deviation) are assigned to a “bad” QF. Dry temperature and physical temperature profiles are checked between 8 km and 25 km. RO temperature profiles, which differ from co-located ECMWF temperature profiles by more than 20 K (maximum allowed dry temperature de-

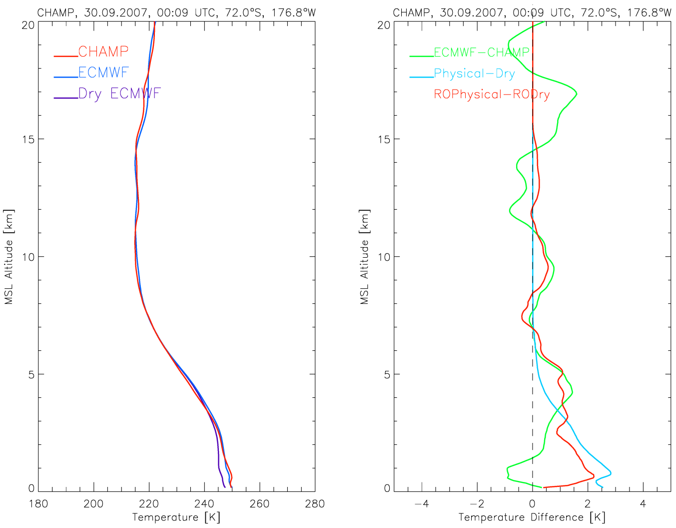

Figure A.10: RO and ECMWF physical temperature and ECMWF dry temperature profiles as a function of MSL altitude (left). The systematic difference between RO and ECMWF physical temperature as well as between ECMWF physical and dry temperature and between RO physical and dry temperature are depicted in the right panel.

viation) are also assigned to a “bad” QF.

Schwarz [Sch13] investigated potential systematic errors in RO climatologies due to irregular distributions of profiles flagged “bad”. He found a larger number of flagged profiles during hemispheric winter at high latitudes and during nighttime. These systematic rejections cause the sampling error of RO climatologies to increase up to four times in some cases and regions.

A.4.10 Reference to the Earth’s Geoid

All dry atmospheric profiles are derived as a function of ellipsoidal height. However, atmospheric parameters derived by the OPS retrieval are finally referenced to the Earth’s geoid (i.e., MSL altitude, as used in the example plots above) where

$$\text{MSL altitude} = \text{height} - \text{geoid undulation}. \tag{A.28}$$

The geoid undulation is extracted from a 0.25° × 0.25° latitude-longitude grid and interpolated to the mean RO event location. The underlying geoid model is the EGM-96 geoid (`http://cddis.nasa.gov/926/egm96/`) that was used in a version smoothed to about 2° × 2° latitude-longitude resolution, about matching the RO horizontal resolution.

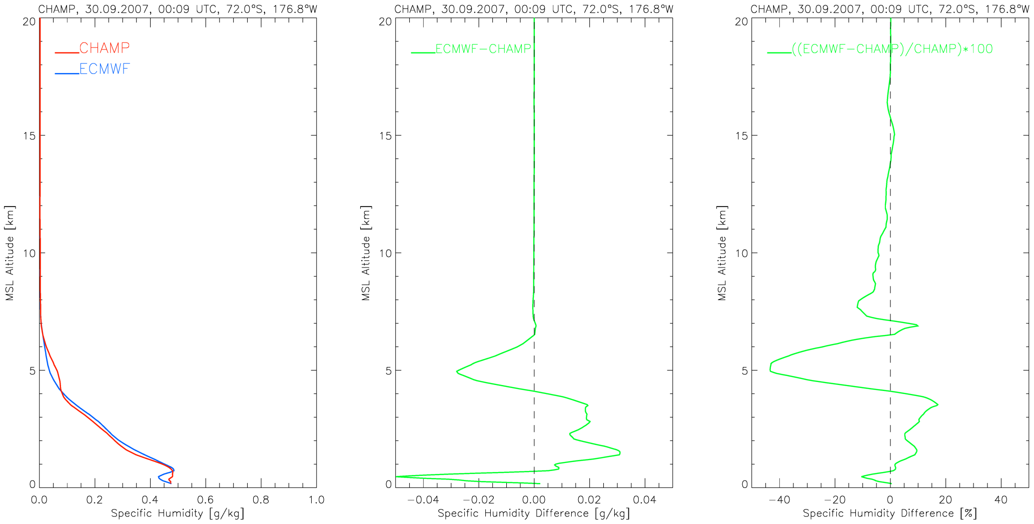

Figure A.11: RO and ECMWF specific humidity profiles as a function of MSL altitude (left). Absolute and relative systematic differences between RO and ECMWF specific humidity are depicted in the middle and right panel, respectively.

A.4.11 Summary of OPSv5.6 Retrieval

The main retrieval steps of OPSv5.6 are summarized in a flowchart shown in Figure A.12 below.

A.5 Beyond OPSv5.6

A.5.1 Rationale for the rOPS

Monitoring the atmosphere to gain accurate and long-term stable records of ECVs[33] such as temperature is the backbone of contemporary atmospheric and climate science. Observation from space is the key to obtain such data globally in the Earth's atmosphere. Currently, however, not any existing satellite-based atmospheric ECV record can serve as authoritative reference over months to decades so that climate variability and change in the atmosphere are not yet reliably monitored.

GNSS RO provides a unique opportunity to solve this problem in the free atmosphere for core ECVs: the thermodynamic variables temperature and pressure, and to some degree water vapor, which are key parameters both for governing atmospheric chemistry and for tracking climate change. RO accurately measures time delays from refraction of GNSS

---

[33] Essential Climate Variables

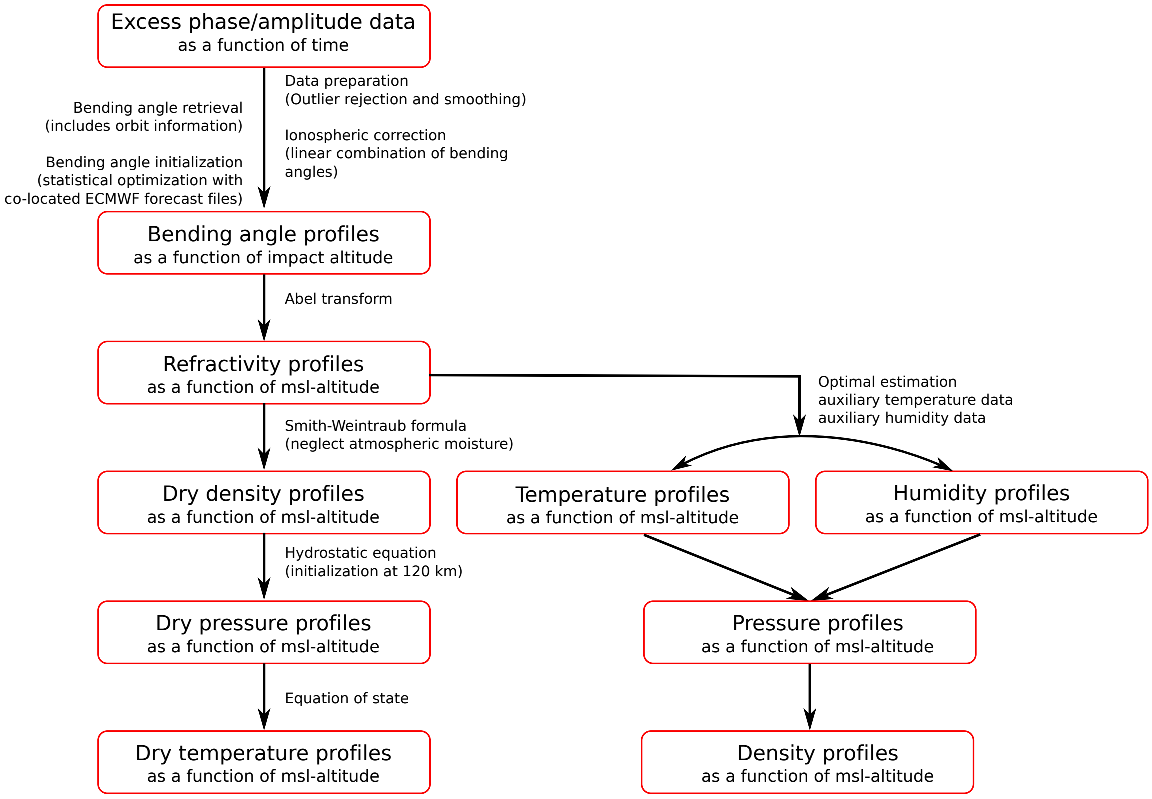

Figure A.12: Summary of the RO retrieval algorithm of the OPSv5.6 retrieval.

signals. This enables to tie RO-derived ECVs and their uncertainty to fundamental time standards, effectively the SI[34] second. These standards feature unique long-term stability and narrow uncertainty. However, despite impressive advances since the pioneering RO mission GPS/MET in the mid-1990ties, no rigorous trace from fundamental time to the ECVs (duly accounting also for relevant side influences) exists so far.

Establishing such a trace first-time in form of the rOPS[35], providing reference RO data for calibration/validation and climate monitoring, research and services, is therefore a current cornerstone endeavor at the WEGC over 2013 to 2016, supported also by colleagues from EUMETSAT Darmstadt, ROM[36]-SAF[37] Copenhagen-Reading, IAP[38] Moscow,

---

[34] Systeme International
[35] Reference Occultation Processing System
[36] Radio Occultation Meteorology
[37] Satellite Application Facility
[38] Institute of Atmospheric Physics

AIUB[39] Bern, DLR[40] Oberpfaffenhofen, UCAR Boulder, JPL[41] Pasadena, IGG[42] Wuhan, and RMIT[43] Melbourne. The rOPS approach demands to process the full chain from the SI-tied raw data to the ECVs with integrated uncertainty propagation. This includes a first step to so-called excess phase level (Level 1a), a second one to atmospheric bending angle level (Level 1b), a third one to refractivity/dry-air level (Level 2a), and a forth one to final thermodynamic ECV profiles (Level 2b).

A.5.2 rOPS Development Projects

The development of the new rOPS was started by the ESA[44] project OPSGRAS[45] (fall 2011 to spring 2014), which led to the development of the basic Level 1b and Level 2a/ 2b processing system components. The FFG[46]-ALR[47] projects OPSCLIMPROP[48], OPSCLIMTRACE[49], OPSCLIMVALUE[50], following the OPSGRAS project over 2013 to 2016 and will complete most components of the new system.

This will enable to trace and propagate the fundamental-time uncertainty and relevant side influences from RO raw tracking data and high-accuracy GPS orbit data to atmospheric variables. In parallel the MMValRO[51]-Extension Project funded by ESA/ESRIN[52] helps to complete the uncertainty propagation chain with Level 2 uncertainty propagation down to the atmospheric ECVs over 2016.

Based on this new rOPS, the WEGC is scheduled to serve as of 2017 as the primary global distribution center for benchmark-quality RO data from multiple future satellite missions such as COSMIC-2[53] and FY-3C[54]/GNOS[55].

---

[39] Astronomical Institute at the University of Bern

[40] Deutsches Zentrum für Luft und Raumfahrt

[41] Jet Propulsion Laboratory

[42] Institute of Geodesy and Geophysics. Chinese Academy of Sciences

[43] Royal Melbourne Institute of Technology

[44] European Space Agency

[45] Reference Occultation Processing System for GRAS on MetOp and other Past and Future RO Missions

[46] Austrian Research Promotion Agency (Österreichische Forschungsförderungsgesellschaft)

[47] Aeronautics and Space Agency

[48] Occultation Processing System for Cal/Val and Climate: Level 1 Processing with Integrated Uncertainty Propagation

[49] Occultation Processing System for Cal/Val and Climate: Algorithm Advancements and SI-traceable Processing

[50] Value-added Products and Validation of Occultation Processing System Re-processing Data for Climate Monitoring

[51] Multi-Mission Validation by Satellite Radio Occultation

[52] European Space Research Institute

[53] Constellation Observing System for Meteorology, Ionosphere, and Climate-2

[54] Feng Yun series-3 satellite C

[55] GNSS radio-occultation sounder

We will also (re-)process data from other RO missions, like the European MetOp/GRAS[56] and the F3C mission, with the aim to broadly provide a new reference standard for thermodynamic ECVs for atmosphere and climate research and applications.

---

[56] Global Navigation Satellite Systems Receiver for Atmospheric Sounding

List of Figures

1.1 Daily number of high quality RO profiles from 2001 to 2016. 17
1.2 Bending angle bias as a function of latitude. 19
1.3 Bending angle noise as a function of latitude. 20
1.4 Bending angle bias as a function of latitude for MetOp-A only. 21
1.5 Dry pressure validation results. 24
1.6 Dry temperature validation results. 25
1.7 Physical temperature validation results. 26
1.8 Specific humidity validation results. 28
1.9 Bending angle bias, noise, and zRAER50 values as a function of time. 33
1.10 Latitudinal and longitudinal event statistics of different satellites in July 2008. 34
1.11 Differences between dry temperature single-satellite climatologies relative to the satellite mean climatology in July 2008. 35
1.12 Sampling error corrected differences between dry temperature single-satellite climatologies relative to the satellite mean climatology in July 2008. 36
1.13 Temporal evolution of dry temperature single-satellite climatologies relative to the satellite mean. 37

2.1 Overview on the number of events of MIPAS and RO data, as well as on the collocated profiles from 2002 to 2012. 39
2.2 Collocation distribution for MIPAS, months July 2003 and 2008. 40
2.3 Global MIPAS versus RO temperature validation results and the number of collocated profile pairs as a function of time from 2002 to 2012. 48
2.4 Global MIPAS versus RO temperature validation results for the UTLS core region (200 hPa to 20 hPa) and the number of collocated profile pairs as a function of time. Top panel: detailed statistical measures for MIPAS[57]v7.03; mean differences: blue; median: red; standard deviation: light-gray bars; 10 % and 90 % Percentiles: green; 90 % RO uncertainty range: dark gray. Bottom panel: Comparison of MIPASv7.03 vs. OPSv5.6 (blue) and MIPASv6.0 (green) vs. OPSv5.6 from 2002 to 2012; mean differences: dashed; median differences: solid. 49

---

[57] Michelson Interferometer for Passive Atmospheric Sounding

2.5 Global MIPAS versus RO temperature validation results from 1000 hPa to 10 hPa and the number of collocated profiles for December 2003. Top panel: detailed statistical measures for MIPASv7.03; mean differences: blue; median: red; standard deviation: light-gray bars; 10 % and 90 % Percentiles: green; 90 % RO uncertainty range: dark gray. Bottom panel: Comparison of MIPASv7.03 vs. OPSv5.6 (blue) and MIPASv6.0 (green) vs. OPSv5.6; mean differences: dashed; median differences: solid. 50

2.6 Global MIPAS versus RO temperature validation results from 1000 hPa to 10 hPa and the number of collocated profiles for February 2008. Top panel: detailed statistical measures for MIPASv7.03; mean differences: blue; median: red; standard deviation: light-gray bars; 10 % and 90 % Percentiles: green; 90 % RO uncertainty range: dark gray. Bottom panel: Comparison of MIPASv7.03 vs. OPSv5.6 (blue) and MIPASv6.0 (green) vs. OPSv5.6; mean differences: dashed; median differences: solid. 51

2.7 Global MIPAS versus RO alititude validation results and the number of collocated profiles as a function of time from 2002 to 2012. 52

2.8 Global MIPAS versus RO altitude validation results for the UTLS core region (200 hPa to 20 hPa) and the number of collocated profile pairs as a function of time. Top panel: detailed statistical measures for MIPASv7.03; mean differences: blue; median: red; standard deviation: light-gray bars; 10 % and 90 % Percentiles: green;. Bottom panel: Comparison of MIPASv7.03 vs. OPSv5.6 (blue) and MIPASv6.0 (green) vs. OPSv5.6 from 2002 to 2012; mean differences: dashed; median differences: solid. 53

2.9 Global MIPAS versus RO altitude validation results from 1000 hPa to 10 hPa and the number of collocated profiles for December 2003. Top panel: detailed statistical measures for MIPASv7.03; mean differences: blue; median: red; standard deviation: light-gray bars; 10 % and 90 % Percentiles: green;. Bottom panel: Comparison of MIPASv7.03 vs. OPSv5.6 (blue) and MIPASv6.0 (green) vs. OPSv5.6; mean differences: dashed; median differences: solid. . . 54

2.10 Global MIPAS versus RO altitude validation results from 1000 hPa to 10 hPa and the number of collocated profiles for February 2008. Top panel: detailed statistical measures for MIPASv7.03; mean differences: blue; median: red; standard deviation: light-gray bars; 10 % and 90 % Percentiles: green;. Bottom panel: Comparison of MIPASv7.03 vs. OPSv5.6 (blue) and MIPASv6.0 (green) vs. OPSv5.6; mean differences: dashed; median differences: solid. . . 55

2.11 Global MIPAS versus RO altitude validation results from 1000 hPa to 10 hPa and the number of collocated profiles for January 2010. Top panel: detailed statistical measures for MIPASv7.03; mean differences: blue; median: red; standard deviation: light-gray bars; 10 % and 90 % Percentiles: green;. Bottom panel: Comparison of MIPASv7.03 vs. OPSv5.6 (blue) and MIPASv6.0 (green) vs. OPSv5.6; mean differences: dashed; median differences: solid. . . 56

2.12 Overview on the number of events of GOMOS and RO data, as well as on the collocated profiles, over 2002 to 2012. 58

2.13 Collocation distribution for GOMOS, months July 2005 and 2008. 59

2.14 Global GOMOS versus RO temperature validation results and the number of collocated profiles as a function of time from 2002 to 2012. 60

2.15 Global GOMOS versus RO temperature validation from 20 km to 25 km (top panel) and 15 km to 20 km (bottom panel) and the number of collocated profiles as a function of time on a monthly scale. Mean systematic differences: blue; median differences: red; standard deviation: light-gray bars; 10 % and 90 % Percentiles: green; 90 % RO uncertainty range: dark gray. 61

2.16 Global GOMOS versus OPSv5.6 temperature validation results from 0 km to 35 km; actual data down to about 18 km/13 km) and the number of collocated profiles for September 2005. Mean systematic differences: blue; median differences: red; standard deviation: light-gray bars; 10 % and 90 % Percentiles: green; 90 % RO uncertainty range: dark gray. 63

2.17 Global GOMOS versus OPSv5.6 temperature validation results from 0 km to 35 km; actual data down to about 18 km/13 km) and the number of collocated profiles for June 2008. Mean systematic differences: blue; median differences: red; standard deviation: light-gray bars; 10 % and 90 % Percentiles: green; 90 % RO uncertainty range: dark gray. 64

2.18 Global GOMOS versus RO density validation results and the number of collocated profiles as a function of time from 2002 to 2012. 66

2.19 Global GOMOS versus RO density validation from 20 km to 25 km (top panel) and 15 km to 20 km (bottom panel) and the number of collocated profiles as a function of time on a monthly scale. Mean systematic differences: blue; median differences: red; standard deviation: light-gray bars; 10 % and 90 % Percentiles: green; 90 % RO uncertainty range: dark gray. 68

2.20 Global GOMOS versus OPSv5.6 density validation results from 0 km to 35 km; actual data down to about 18 km/13 km) and the number of collocated profiles for September 2005. Mean systematic differences: blue; median differences: red; standard deviation: light-gray bars; 10 % and 90 % Percentiles: green; 90 % RO uncertainty range: dark gray. 69

2.21 Global GOMOS versus OPSv5.6 density validation results from 0 km to 35 km; actual data down to about 18 km/13 km) and the number of collocated profiles for June 2008. Mean systematic differences: blue; median differences: red; standard deviation: light-gray bars; 10 % and 90 % Percentiles: green; 90 % RO uncertainty range: dark gray. 70

2.22 Overview on the number of events of RAOB and RO data, as well as on the collocated profiles, from 2002 to 2016. 72

2.23 Collocation distribution for RAOB, months July 2005 and 2008. 73

2.24 Global RAOB versus RO temperature validation results from 1000 hPa to 10 hPa and the number of collocated profiles as a function of time from 2002 to 2012. 74

2.25 Global RAOB versus RO temperature validation results of the UTLS core region (200 hPa to 20 hPa) and the number of collocated profiles as a function of time from 2002 to 2012. Mean systematic differences: blue; median differences: red; standard deviation: light-gray bars; 10 % and 90 % Percentiles: green; 90 % RO uncertainty range: dark gray. 75

2.26 Number of high quality RAOB[58] measurements separated into different radiosonde types (Vaisala RS80, RS90, RS92, RS41)on a daily basis from 2001 to 2016. 76

2.27 Global OPSv5.6 versus RAOB temperature validation results from 1000 hPa to 10 hPa and the number of collocated profiles for May 2003. Mean systematic differences: blue; median differences: red; standard deviation: light-gray bars; 10 % and 90 % Percentiles: green; 90 % RO uncertainty range: dark gray. 77

2.28 Global OPSv5.6 versus RAOB temperature validation results from 1000 hPa to 10 hPa and the number of collocated profiles for July 2007. Mean systematic differences: blue; median differences: red; standard deviation: light-gray bars; 10 % and 90 % Percentiles: green; 90 % RO uncertainty range: dark gray. 78

2.29 Global RO versus RAOB humidity validation results of the troposphere (1000 hPa to 100 hPa) and the number of collocated profiles as a function of time from 2002 to 2016. 80

2.30 Global RO versus RAOB humidity validation results for the troposphere (800 hPa to 500 hPa and 500 hPa to 200 hPa) and the number of collocated profiles as a function of time from 2002 to 2016. Mean systematic differences: blue; median differences: red; standard deviation: light-gray bars; 10 % and 90 % Percentiles: green. 81

---

[58] Radiosonde Observation (Rawinsonde Observation)

2.31 Global RO versus RAOB humidity validation results from 1000 hPa to 100 hPa and the number of collocated profiles for May 2003. Mean systematic differences: blue; median differences: red; standard deviation: light-gray bars; 10 % and 90 % Percentiles: green. 82
2.32 Global RO versus RAOB humidity validation results from 1000 hPa to 100 hPa and the number of collocated profiles for July 2007. Mean systematic differences: blue; median differences: red; standard deviation: light-gray bars; 10 % and 90 % Percentiles: green. 83
2.33 Map of GRUAN stations which were active in the study time period 2009 to 2016. 84
2.34 Comparison of temperature between RO and GRUAN for the time period 2009 to 2016 for all profile pairs between 30°N to 60°N. 85
2.35 Comparison of specific humidity between RO and GRUAN for the time period 2009 to 2016 for all profile pairs between 30°N to 60°N. 86
2.36 Comparison of specific humidity between RO and GRUAN for the time period 2009 to 2016 for all profile pairs between 30°S to 30°N. 87

3.1 MMValRO PPS structure: information flows, processes and input and output data. 91
3.2 OPS structure: information flows, processes and input and output data. . . . 92
3.3 Job chains implemented via the job scheduler. 98
3.4 Data smoothing example for an arbitrarily chosen collocated profile pair of GOMOS and RO data from August 8, 2005. 104

A.1 Occultation geometry of a setting RO event. 127
A.2 Summary of dry temperature errors as a function of altitude. 129
A.3 Minimal impact height of OPSv5.4 and OPSv5.6 bending angle profiles. . . . 132
A.4 RO and ECMWF refractivity profiles and their systematic difference. 137
A.5 RO and ECMWF dry density and ECMWF physical density profiles as well as their systematic differences. 138
A.6 RO and ECMWF dry pressure and ECMWF physical pressure profiles as well as their systematic differences. 139
A.7 RO and ECMWF dry temperature and ECMWF physical temperature profiles as well as their systematic differences. 140
A.8 RO and ECMWF geopotential height profiles as a function of dry pressure altitude and their systematic difference. 142
A.9 RO and ECMWF physical pressure and ECMWF dry pressure profiles as well as their systematic differences. 145
A.10 RO and ECMWF physical temperature and ECMWF dry temperature profiles as well as their systematic differences. 146

A.11 RO and ECMWF specific humidity as well as their systematic difference. . . 147
A.12 Summary of the RO retrieval algorithm. 148

List of Tables

2.1 Temperature bias and standard deviation of MIPAS versus OPS for the whole envisat period. . . . 43
2.2 Altitude bias and standard deviation of MIPAS versus OPS for the whole envisat period. . . . 46
2.3 Mean temperature bias and standard deviation of GOMOS versus OPSv5.6 for the whole ENVISAT period. . . . 63
2.4 Mean density bias and standard deviation of GOMOS versus OPS for the whole envisat period. . . . 67

3.1 Overview on MIPAS data stream. . . . 94
3.2 Overview over GOMOS data stream. . . . 95
3.3 Overview over RAOB data stream. . . . 96
3.4 Overview over RO data stream. . . . 97
3.5 Time lines and dependencies. . . . 100

Reference Documents

The following documents are applicable to and/or referenced by the present document.

[Ant11] R. A. Anthes. “Exploring Earth’s atmosphere with radio occultation: contributions to weather, climate, and space weather”. In: *Atmos. Meas. Tech.* 4 (2011), pp. 1077–1103. DOI: 10.5194/amt-4-1077-2011 (cit. on pp. 126, 128).

[ASW03] C. O. Ao, W. S. Schreiner, and J. Wickert. *First report on the CHAMP radio occultation intercomparison study.* JPL publication 03-016. JPL, 2003 (cit. on p. 16).

[BKF07] M. Borsche, G. Kirchengast, and U. Foelsche. “Tropical tropopause climatology as observed with radio occultation measurements from CHAMP compared to ECMWF and NCEP analyses”. In: *Geophys. Res. Lett.* 34, L03702 (2007). DOI: 10.1029/2006GL027918 (cit. on p. 32).

[DSPF13] J. Danzer, B. Scherllin-Pirscher, and U. Foelsche. “Systematic residual ionospheric errors in radio occultation data and a potential way to minimize them”. In: *Atmos. Meas. Tech.* 6 (2013), pp. 2169–2179. DOI: 10.5194/amt-6-2169-2013 (cit. on p. 18).

[Eng06] A. von Engeln. “A first test of climate monitoring with radio occultation instruments: Comparing two processing centers”. In: *Geophys. Res. Lett.* 33, L22705 (2006). DOI: 10.1029/2006GL027767 (cit. on p. 16).

[Esh73] V. R. Eshleman. “The radio occultation method for the study of planetary atmospheres”. In: *Planet. Space Sci.* 21.9 (1973), pp. 1521–1531. DOI: 10.1016/0032-0633(73)90059-7 (cit. on p. 126).

[FE68] G. Fjeldbo and V. R. Eshleman. “The atmosphere of Mars analyzed by integral inversion of the Mariner IV occultation data”. In: *Planet. Space Sci.* 16.8 (1968), pp. 1035–1059. DOI: 10.1016/0032-0633(68)90020-2 (cit. on p. 126).

[FH99] D. D. Feng and B. M. Herman. “Remotely sensing the Earth’s atmosphere using the Global Positioning System (GPS)—The GPS/MET data analysis”. In: *J. Atmos. Oceanic Technol.* 16.8 (1999), pp. 989–1002. DOI: 10.1175/1520-0426(1999)016<0989:RSTESA>2.0.CO;2 (cit. on p. 132).

[Foe99] U. Foelsche. “Tropospheric water vapor imaging by combination of ground-based and spaceborne GNSS sounding data”. PhD Thesis. University of Graz, Austria: IGAM, 1999 (cit. on p. 143).

[Foe+08] U. Foelsche et al. “Observing upper troposphere-lower stratosphere climate with radio occultation data from the CHAMP satellite”. In: *Climate Dyn.* 31 (2008), pp. 49–65. DOI: `10.1007/s00382-007-0337-7` (cit. on pp. 32, 137).

[Foe+09a] U. Foelsche et al. “Assessing the climate monitoring utility of radio occultation data: From CHAMP to FORMOSAT-3/COSMIC”. In: *Terr. Atmos. Ocean. Sci.* 20.1 (2009), pp. 155–170. DOI: `10.3319/TAO.2008.01.14.01(F3C)` (cit. on p. 30).

[Foe+09b] U. Foelsche et al. “Climatologies based on radio occultation data from CHAMP and Formosat-3/COSMIC”. In: *New Horizons in Occultation Research: Studies in Atmosphere and Climate*. Ed. by A. K. Steiner et al. Berlin Heidelberg: Springer, 2009, pp. 181–194. DOI: `10.1007/978-3-642-00321-9\_15` (cit. on p. 30).

[Foe+11] U. Foelsche et al. “Refractivity and temperature climate records from multiple radio occultation satellites consistent within 0.05 %”. In: *Atmos. Meas. Tech.* 4 (2011), pp. 2007–2018. DOI: `10.5194/amt-4-2007-2011` (cit. on pp. 31, 126, 128).

[GK04] A. Gobiet and G. Kirchengast. “Advancements of Global Navigation Satellite System radio occultation retrieval in the upper stratosphere for optimal climate monitoring utility”. In: *J. Geophys. Res.* 109, D24110 (2004). DOI: `10.1029/2004JD005117` (cit. on p. 135).

[Gob05] A. Gobiet. *Radio occultation data analysis for climate change monitoring and first climatologies from CHAMP (Ph.D. Thesis)*. Austria: Wegener Center Verlag Graz, 2005. ISBN: 3-9502126-3-9 (cit. on p. 134).

[Gob+05] A. Gobiet et al. “Climatological validation of stratospheric temperatures in ECMWF operational analyses with CHAMP radio occultation data”. In: *Geophys. Res. Lett.* 32, L12806 (2005). DOI: `10.1029/2005GL022617` (cit. on p. 32).

[Gor02] M. E. Gorbunov. “Canonical transform method for processing radio occultation data in the lower troposphere”. In: *Radio Sci.* 37.5 (2002). DOI: `10.1029/2000RS002592` (cit. on p. 133).

[Gor+04] M. E. Gorbunov et al. “Comparative analysis of radio occultation processing approaches based on Fourier integral operators”. In: *Radio Sci.* 39, RS6004 (2004). DOI: `10.1029/2003RS002916` (cit. on pp. 130, 133).

[Haj+04] G. A. Hajj et al. “CHAMP and SAC-C atmospheric occultation results and intercomparisons”. In: *J. Geophys. Res.* 109, D06109 (2004). DOI: `10.1029/2003JD003909` (cit. on p. 30).

[Hea09] S. Healy. *Refractivity coefficients used in the assimilation of GPS radio occultation measurements.* GRAS SAF Report 9. GRAS SAF, 2009, p. 18 (cit. on p. 143).

[Hed91] A. E. Hedin. “Extension of the MSIS thermosphere model into the middle and lower atmosphere”. In: *J. Geophys. Res.* 96.A2 (1991), pp. 1159–1172. DOI: `10.1029/90JA02125` (cit. on p. 134).

[HIT03] K. Hocke, K. Igarashi, and T. Tsuda. “High-resolution profiling of layered structures in the lower stratosphere by GPS occultation”. In: *Geophys. Res. Lett.* 30.8 (2003). DOI: `10.1029/2002GL016566` (cit. on p. 134).

[Ho+12] S.-P. Ho et al. “Reproducibility of GPS radio occultation data for climate monitoring: Profile-to-profile inter-comparison of CHAMP climate records 2002 to 2008 from six data centers”. In: *J. Geophys. Res.* 117, D18111 (2012). DOI: `10.1029/2012JD017665` (cit. on p. 16).

[HWLW08] B. Hofmann-Wellenhof, H. Lichtenegger, and E. Wasle. *GNSS—Global Navigation Satellite Systems.* Wien New York: Springer, 2008, p. 516 (cit. on p. 128).

[Jak+02] N. Jakowski et al. “GPS/GLONASS-based TEC measurements as a contributor for space weather forecast”. In: *J. Atmos. Solar-Terr. Phys.* 64 (2002), pp. 729–735 (cit. on p. 126).

[Kir+13] G. Kirchengast et al. *Reference OPS Detailed Algorithm Descriptions Document.* Technical Report. Version 1. University of Graz, Austria: WEGC and IGAM, 2013 (cit. on p. 142).

[KLH07] N. Khélifa, M. Lecollinet, and M. Himbert. “Molar mass of dry air in mass metrology”. In: *Measurement* 40.7–8 (2007), pp. 779–784. DOI: `10.1016/j.measurement.2006.05.009` (cit. on p. 138).

[KS10] G. Kirchengast and M. Schwärz. *MMValRO Project Management Plan.* ESRIN/Contract No. 21651/08/I-EC 2̌013 MMValRO. ESA/ESRIN, 2010, p. 22 (cit. on p. 88).

[Kuo+00] Y.-H. Kuo et al. “Assimilation of GPS radio occultation data for numerical weather prediction”. In: *Terr. Atmos. Ocean. Sci.* 11.1 (2000), pp. 157–186 (cit. on p. 126).

[Kur+97] E. R. Kursinski et al. “Observing Earth’s atmosphere with radio occultation measurements using the Global Positioning System”. In: *J. Geophys. Res.* 102.D19 (1997), pp. 23429–23465. DOI: `10.1029/97JD01569` (cit. on pp. 126, 129, 130, 137).

[Lac10] B. C. Lackner. *Exploring trend indicators of climate change from radio occultation and optimal trend detection (Ph.D. thesis)*. Sci. Rep. 38-2010. Austria: Wegener Center Verlag Graz, 2010. ISBN: 978-3-9502940-5-7 (cit. on p. 21).

[Lac+11] B. C. Lackner et al. “Atmospheric Climate Change Detection by Radio Occultation Data Using a Fingerprinting Method”. In: *J. Climate* 24 (2011), pp. 5275–5291. DOI: `10.1175/2011JCLI3966.1` (cit. on p. 16).

[Lad+11] F. Ladstädter et al. “An assessment of differences in lower stratospheric temperature records from (A)MSU, radiosondes, and GPS radio occultation”. In: *Atmos. Meas. Tech.* 4 (2011), pp. 1965–1977. DOI: `10.5194/amt-4-1965-2011` (cit. on p. 16).

[Lad+15] F. Ladstädter et al. “Climate intercomparison of GPS radio occultation, RS90/92 radiosondes and GRUAN from 2002 to 2013”. In: *Atmos. Meas. Tech.* 8 (2015), pp. 1819–1834. DOI: `10.5194/amt-8-1819-2015` (cit. on pp. 79, 84).

[LLS09] A. Löscher, K. B. Lauritsen, and M. Sørensen. “The GRAS SAF radio occultation processing intercomparison project ROPIC”. In: *New Horizons in Occultation Research: Studies in Atmosphere and Climate*. Ed. by A. K. Steiner et al. Berlin, Heidelberg: Springer-Verlag, 2009, pp. 49–62. DOI: `10.1007/978-3-642-00321-9_5` (cit. on p. 16).

[MTN08] P. J. Mohr, B. N. Taylor, and D. B. Newell. “CODATA recommended values of the fundamental physical constants: 2006”. In: *Rev. Mod. Phys.* 80 (2008), pp. 663–730. DOI: `10.1103/RevModPhys.80.633` (cit. on p. 138).

[Pir10] B. Pirscher. *Multi-satellite climatologies of fundamental atmospheric variables from radio occultation and their validation (Ph.D. thesis)*. Sci. Rep. 33-2010. Austria: Wegener Center Verlag Graz, 2010. ISBN: 978-3-9502940-3-3 (cit. on p. 31).

[Rie+16] T. Rieckh et al. *Tropospheric dry Layers in the Tropical Western Pacific: A comparison of Multiple Data Sets*. OPAC-IROWG 2016, 5–11 September 2013: Seggau, Austria. 2016. URL: `https://wegcwww.uni-graz.at/opacirowg2016/data/public/files/opacirowg2016_Therese_Rieckh_presentation_214.pdf` (cit. on p. 82).

[Rod00] C. D. Rodgers. *Inverse Methods for Atmospheric Sounding: Theory and Practice*. Vol. 2. Series on Atmospheric Oceanic and Planetary Physics. Singapore: World Scientific Publishing Company, 2000 (cit. on p. 135).

[Sch13] J. Schwarz. *Potential Systematic Errors in Radio Occultation Climatologies due to Irregular Distributions of Apparent Outliers in the Retrieval Process.* Sci. Rep. 54-2013. Austria: Wegener Center Verlag Graz, 2013. ISBN: 978-3-9503608-1-3 (cit. on p. 146).

[Sch+07] W. Schreiner et al. “Estimates of the precision of GPS radio occultations from the COSMIC/FORMOSAT-3 mission”. In: *Geophys. Res. Lett.* 34, L04808 (2007). DOI: `10.1029/2006GL027557` (cit. on p. 30).

[Sch+10] M. Schwaerz et al. *MMValRO Annual Report No. 2, covering the period Aug 2009 to Aug 2010.* Technical report. University of Graz, Austria: WEGC and IGAM, 2010 (cit. on p. 89).

[Sch+13] M. Schwärz et al. *Multi-Mission Validation by Satellite Radio Occultation.* Final report for ESA/ESRIN No. 01/2013. University of Graz, Austria: WEGC, 2013, p. 187 (cit. on pp. 21, 89, 120).

[Sch+99] W. S. Schreiner et al. “Analysis and validation of GPS/MET radio occultation data in the ionosphere”. In: *Radio Sci.* 34.4 (1999), pp. 949–966 (cit. on p. 126).

[SD10] V. Sofieva and F. Dalaudier. *Recommendations for validation of high-resolution temperature profiles.* Technical note. FMI Helsinki, Finnland, 2010 (cit. on p. 103).

[SK04] A. K. Steiner and G. Kirchengast. “Ensemble-based analysis of errors in atmospheric profiles retrieved from GNSS occultation data”. In: *Occultations for Probing Atmosphere and Climate.* Ed. by G. Kirchengast, U. Foelsche, and A. K. Steiner. Berlin, Heidelberg: Springer-Verlag, 2004, pp. 149–160 (cit. on p. 102).

[SK05] A. K. Steiner and G. Kirchengast. “Error analysis of GNSS radio occultation data based on ensembles of profiles from end-to-end simulations”. In: *J. Geophys. Res.* 110, D15307 (2005). DOI: `10.1029/2004JD005251` (cit. on p. 22).

[SLK06] A. K. Steiner, A. Löscher, and G. Kirchengast. “Error characteristics of refractivity profiles retrieved from CHAMP radio occultation data”. In: *Atmosphere and Climate: Studies by Occultation Methods.* Ed. by U. Foelsche, G. Kirchengast, and A. K. Steiner. Berlin, Heidelberg: Springer-Verlag, 2006, pp. 27–36 (cit. on p. 22).

[Sof+08] V. F. Sofieva et al. “On the variability of temperature profiles in the stratosphere: Implications for validation”. In: *Geophys. Res. Lett.* 35, L23808 (2008). DOI: `10.1029/2008GL035539` (cit. on pp. 38, 99).

[SP+11a] B. Scherllin-Pirscher et al. "Empirical analysis and modeling of errors of atmospheric profiles from GPS radio occultation". In: *Atmos. Meas. Tech.* 4 (2011), pp. 1875–1890. DOI: `10.5194/amt-4-1875-2011` (cit. on pp. 22, 41, 65).

[SP+11b] B. Scherllin-Pirscher et al. "Quantifying uncertainty in climatological fields from GPS radio occultation: an empirical-analytical error model". In: *Atmos. Meas. Tech.* 4 (2011), pp. 2019–2034. DOI: `10.5194/amt-4-2019-2011` (cit. on pp. 41, 44, 65, 137).

[SP+12] B. Scherllin-Pirscher et al. "The vertical and spatial structure of ENSO in the upper troposphere and lower stratosphere from GPS radio occultation measurements". In: *Geophys. Res. Lett.* 39, L20801 (2012). DOI: `10.1029/2012GL053071` (cit. on p. 16).

[Ste98] A. K. Steiner. "High resolution sounding of key climate variables using the radio occultation technique". PhD thesis. University of Graz, Austria: IGAM, 1998 (cit. on p. 136).

[Ste+01] A. K. Steiner et al. "GNSS occultation sounding for climate monitoring". In: *Phys. Chem. Earth A* 26.3, D09102 (2001), pp. 113–124. DOI: `10.1016/S1464-1895(01)00034-5` (cit. on p. 126).

[Ste+09] A. K. Steiner et al. "Atmospheric temperature change detection with GPS radio occultation 1995 to 2008". In: *Geophys. Res. Lett.* 36, L18702 (2009). DOI: `10.1029/2009GL039777` (cit. on p. 16).

[Ste+11] A. K. Steiner et al. "GPS radio occultation for climate monitoring and change detection". In: *Radio Sci.* 46, RS0D24 (2011). DOI: `10.1029/2010RS004614` (cit. on pp. 16, 126, 128).

[Ste+13] A. K. Steiner et al. "Quantification of structural uncertainty in climate data records from GPS radio occultation". In: *Atmos. Chem. Phys.* 13 (2013), pp. 1469–1484. DOI: `10.5194/acp-13-1469-2013` (cit. on pp. 16, 41, 44, 65).

[SW53] E. Smith and S. Weintraub. "The constants in the equation for atmospheric refractive index at radio frequencies". In: *Proc. IRE* 41 (1953), pp. 1035–1037 (cit. on pp. 137, 143).

[Syn98] S. Syndergaard. "Modeling the impact of the Earth's oblateness on the retrieval of temperature and pressure profiles from limb sounding". In: *J. Atmos. Solar-Terr. Phys.* 60.2 (1998), pp. 171–180. DOI: `10.1016/S1364-6826(97)00056-4` (cit. on p. 133).

[Syn99] S. Syndergaard. *Retrieval analysis and methodologies in atmospheric limb sounding using the GNSS radio occultation technique.* DMI Sci Rep 99-6. Danish Meteorological Institute, Copenhagen, Denmark. 1999, p. 131 (cit. on pp. 127, 132).

[Tha74] G. D. Thayer. “An improved equation for the radio refractive index of air”. In: *Radio Sci.* 9.10 (1974), pp. 803–807. DOI: `10.1029/RS009i010p00803` (cit. on p. 143).

[Wan+04] D.-Y. Wang et al. “Cross-validation of MIPAS/ENVISAT and GPS-RO/CHAMP temperature profiles”. In: *J. Geophys. Res.* 109, D19311 (2004). DOI: `10.1029/2004JD004963` (cit. on p. 105).

[War+96] R. Ware et al. “GPS sounding of the atmosphere from low Earth orbit: Preliminary results”. In: *Bull. Amer. Meteor. Soc.* 77.1 (1996), pp. 19–40. DOI: `10.1175/1520-0477(1996)077<0019:GSOTAF>2.0.CO;2` (cit. on p. 126).

[ECM16] ECMWF. *Changes in ECMWF model.* 2016. URL: `http://www.ecmwf.int/en/forecasts/documentation-and-support/changes-ecmwf-model` (cit. on p. 121).

[GRA09] GRAS SAF. *The radio occultation processing package (ROPP) user guide, part II: Forward model and 1DVar modules.* User Guide. DMI ECMWF IEEC MetO. 2009, p. 79 (cit. on p. 141).

[NIS01] NIST. *The International System of Units (SI).* NIST Special Publication 330. National Institute of Standards and Technology, 2001. URL: `http://physics.nist.gov/Document/sp330.pdf` (cit. on p. 141).